AMERICAN UNIVERSITY OF BEIRUT

DFT STUDIES ON TERMINAL VERSUS BRIDGED N_2 BINDING IN TRANSITION METAL CHEMISTRY AND REACTIONS OF METAL-NITRIDE COMPLEXES

by
LYNN SAMIRA YAMOUT

A thesis
submitted in partial fulfillment of the requirements
for the degree of Master of Science
to the Department of Chemistry
of the Faculty of Arts and Sciences
at the American University of Beirut

Beirut, Lebanon
August 2021

AMERICAN UNIVERSITY OF BEIRUT

DFT STUDIES ON TERMINAL VERSUS BRIDGED N_2 BINDING IN TRANSITION METAL CHEMISTRY AND REACTIONS OF METAL-NITRIDE COMPLEXES

by
LYNN SAMIRA YAMOUT

Approved by:

Dr. Faraj Hasanayn, Professor — Advisor
Chemistry

Dr. Tarek Ghaddar, Professor — Member of Committee
Chemistry

Dr. Mohamad Hmadeh, Associate Professor — Member of Committee
Chemistry

Date of thesis defense: August 24, 2021

AMERICAN UNIVERSITY OF BEIRUT

THESIS, DISSERTATION, PROJECT RELEASE FORM

Student Name: Yamout Lynn Samira Mohamad

Last First Middle

☑ Master's Thesis ◯ Master's Project ◯ Doctoral Dissertation

☑ I authorize the American University of Beirut to: (a) reproduce hard or electronic copies of my thesis, dissertation, or project; (b) include such copies in the archives and digital repositories of the University; and (c) make freely available such copies to third parties for research or educational purposes.

☐ I authorize the American University of Beirut, to: (a) reproduce hard or electronic copies of it; (b) include such copies in the archives and digital repositories of the University; and (c) make freely available such copies to third parties for research or educational purposes after: **One ___ year from the date of submission of my thesis, dissertation or project.**
Two ___ years from the date of submission of my thesis , dissertation or project.
Three ___ years from the date of submission of my thesis , dissertation or project.

15/09/2021

Signature Date

This form is signed when submitting the thesis, dissertation, or project to the University Libraries

Acknowledgements

The work summarized in this thesis was completed during an extremely difficult time internationally and locally. Starting with the October 19, 2019 revolution, to a global pandemic, to a devastating economic collapse, the past two years have been challenging for AUB. So, it would be foolish to assume that this work has been an individual effort. This work was a result of the support and investment of numerous people, of whom I would like to thank a few. First off, I would like to thank God for His faithfulness and endless grace and mercies shown to me in the past two years. To my father, Mohammad Said Yamout, thank you for constantly challenging me to push myself further, to never take things for granted, and to work hard to achieve my goals. To my mother, Grace Hanan Moussa, thank you for your relentless support, for teaching me how to put others first, and for being my first teacher. It is due to my parents that I have a work ethic and a constant desire to grow. To my siblings Laya, Selina, Peter and Sara, thank you for standing by me and always being ready to listen. I would like to thank my church family (Pastor Abo Issa, Mohamad, Grace, Mohamad Ataya, Christina, Mirvet, Majdi, Jeremy, Laya, Selina, Peter and Sara) for constantly pouring into me and supporting me in the toughest of my personal life. To Vicken and Talar, thank you for your mentorship and prayer throughout the past few years. To my advisor, Professor Faraj Hasanayn, thank you for your academic guidance in the past two years. Thank you for always being available for feedback and ready to teach me something new. Thank you for teaching me how to teach and how to share my knowledge well with anyone no matter what their academic background is. Thank you for your patience and kindness towards me during my time in your lab. It is has been a joy an honor to be a student of yours. Professor Pierre Karam, it is in your undergraduate CHEM 201L class that I first realized how fascinating science really is. You showed me that not only is science all around me, but that I could be a part of it too. Thank you! Thank you for also supporting my loved ones and I in some of the most difficult times. Professor Najat Saliba, thank you for being an exemplary role model as a Lebanese woman in science. Thank you for showing me that everything I do, every project I take on, must have purpose and that I can make a difference. The time I spent in your lab was a formative time for me. Professor Kamal Bouhadir, thank you for teaching me that I don't truly understand something if I can not explain it to the guy at a falafel stand. You made what some may consider the most difficult branch of chemistry, organic chemistry, a pleasure to learn. To Professor Lara Halaoui, thank you for introducing me to the world batteries and energy. Thank you for being kind, approachable and an amazing example of a strong female scientist in the Middle East. Thank you for guiding me in how to instruct a lab well by being an amazing instuctor yourself. To my committee member Mohamad Hmadeh, it is in your courses that I discovered my potential as a scientist. Whether it is through designing my own MOF, or writing my first proposal, or attempting to write a review paper, it is under your mentorship that I realized that I have what it takes to go further in science. Thank you for that. To my committee member Tarek Ghaddar, thank you for taking a chance on me in my final year at AUB and agreeing to be a member on my committee. Thank you for showing me what true dedication and commitment to science and raising young scientists is. You have had a great share of sickness and challenges this past year, but remained an outstanding instructor! To Miss Lara Abramian, Saydeh and Nayri, thank you for everything you do to make the department labs run smoothly. Thank you for all the times you stayed later to make sure an experiment works. Thank you for all the sacrifice that you do that goes unaccredited. Thank you to my friends and colleagues Mohamad Ataya, Elissa Shehayeb, Nayri Jaboutian, Josephina Mallah, Meghrie Jilakian, Mariam Barakat and many more who have been an amazing support group during my time at AUB. Many more people have contributed to this work who may have gone unmentioned. I am forever grateful to every person who has shown me support, encouraged me to grow, and challenged me to break new ground. Thank you all! I love you!

An Abstract of the Thesis of

Lynn Samira Yamout for Master of Science
Major: Chemistry

Title: DFT Studies on Terminal versus Bridged N_2 Binding in Transition Metal Chemistry and Reactions of Metal-Nitride Complexes

Structure determines function. Although this statement is simple in principle, understanding how structure can affect the function of a molecule, enzyme or catalyst can be a very complex process. Whether it is the coordination geometry, the arrangement of molecular orbitals, or the way intramolecular forces can cause a molecule to fold around itself, it is hard to determine exactly what causes a molecule or catalyst to react in a certain way. Fortunately, the development and advancement of quantum mechanical methods such as Density Functional Theory (DFT) has allowed chemists to take a deeper look at the structural properties of chemical systems. Herein, we utilize such computational methods to understand the behavior of molecular catalysts in the synthesis of ammonia from dinitrogen. The following work is divided into three main parts. After the introduction, the second chapter focuses on the equilibrium between terminal N_2 metal complexes and bridging N_2 complexes. The coordination of N_2 to a metal catalyst is the first step in the ammonia synthesis process. While some molecular catalysts spontaneously form terminal N_2 complexes in solution upon exposure to a flow of N_2, others form bridged N_2 complexes. In Chapter 2, we consider several organometallic complexes, all with previous experimental data, of different metal centers, coordination spheres and π-electron counts. We split the equilibrium of interest into simpler fundamental steps and calculate the energies of each step. Based on the analysis of the computed data, we propose a π-Bond order (π-BO) model which explains why complexes prefer either mode of N_2 coordination based on the number of π-electrons in the system. In the third chapter, we consider the thermodynamics and kinetics of the formation and cleavage of bridged N_2 complexes. We study the effect of the nature of the metal and the coordination sphere by considering two different organometallic systems with several metal centers. We utilize the proposed π-BO model and MO-theory in attempt to determine the factors affecting the formation and cleavage of bridging N_2 complexes. In Chapter

3, we also reproduce the the kinetics of the experimentally observed cleavage of Schneider's bridging N_2 complex and see how changing the metal center affects these kinetic observations. The last chapter of this work considers reactions of metal nitride complexes, the products of the previously considered cleavage reactions. This has direct applications in molecular catalysis of NH_3 synthesis from N_2. We consider five different transfer reactions to the metal nitride: a proton transfer, an electron transfer, a hydrogen atom transfer, a nitrogen atom transfer, and an oxygen atom transfer. We study the effect of the metal and coordination sphere on such reactions by considering two systems and alter the nature of the metal center. We hope that the studies included in this work contribute to the design and synthesis of more efficient catalysts for ammonia synthesis.

Contents

List of Figures

List of Tables

Chapter 1

Introduction

1.1 The Haber-Bosch Process

Ammonia is commonly used as starting material for agricultural fertilizers. The industrial revolution in the 1800s followed by the rapid increase in the world population led to a spike in the global demand of ammonia. Inspired by the biological nitrogenase enzyme scientists raced to supply this demand by synthesizing ammonia from its elements N_2 and H_2. In 1909, Fritz Haber, a German scientist, succeeded at producing ammonia using an iron catalyst under high pressure and temperature. Carl Bosch later built upon this proof of principle to industrialize the ammonia production process, now called the Haber-Bosch process. Both Haber and Bosch were awarded Nobel Prizes in Chemistry for their accomplishments, in 1918 and 1931, respectively [1]. More recently, Gerhard Ertl was awarded the Nobel Prize in Chemistry for his contributions to the field of surface chemistry. In his work he highlighted the major substrate-catalyst interactions that allow the synthesis of ammonia to proceed [2].

$$N_{2(g)} + 3H_{2(g)} \xrightarrow[\substack{400\text{-}600^{o}C \\ 200\text{-}300\ \text{atm}}]{\text{Iron Catalyst}} 2NH_{3(g)}$$

Figure 1.1: The Haber-Bosch Process

The Haber-Bosch process became the main source of the world's ammonia supply, reaching a production rate of over 150 million metric tons per year with an expected 2.3% annual increase [3]. This process is energy and resource hungry, not to mention its severe environmental impacts with high CO_2 emissions. As a result, a search began to find alternate methods of ammonia synthesis which are less energy demanding and more environment-friendly. One of these approaches involves the use of molecular catalysts for the electrocatalytic reduction of N_2 to NH_3.

1.2 Alternative Methods of Ammonia Synthesis

1.2.1 A Molecular Approach

Transition metal dinitrogen complexes have been the subject of intense research, since their discovery in the mid-60s, due to their potential utility as homogeneous catalysts for N_2 functionalization. Above all, there is interest at present to develop molecular catalysts for N_2 reduction into ammonia that may provide a greener and more sustainable alternative to the century old Haber-Bosch process.

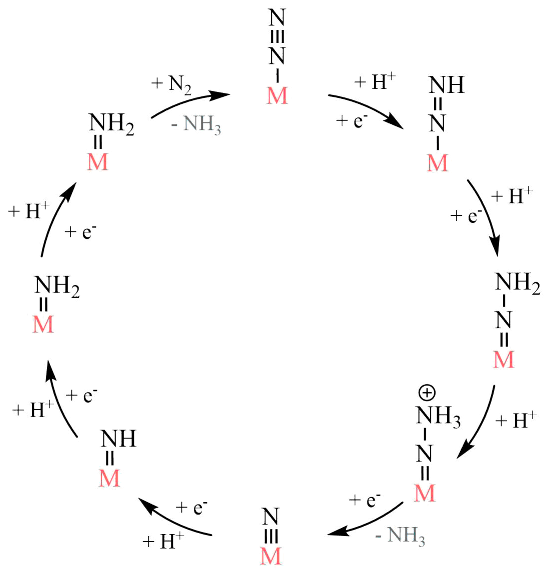

Figure 1.2: The Chatt Cycle

In 1975, Chatt identified a mechanism of N_2 fixation and reduction on a molecular metal center [4]. This mechanism is known as the "Chatt Cycle". Upon coordination to the metal center, the N_2 molecule undergoes and sequence of protonation and reduction reactions at the distal nitrogen. This distal path may be inhibited by formation of a bridging end-on N_2 complex, but an MNNM complex can instead undergo cleavage directly into two metal nitrides prior to any reduction.

1.2.2 Cummins & Laplaza 1995

In 1995, Cummins and Laplaza identified the formation of a bridging complex during the formation of metal nitrides from a three coordinate Mo (III) complex [5]. At subzero temperatures and a flow of 1atm N_2, a red-orange hydrocarbon solution of $Mo(NRAr)_3$ ($R=C(CD_3)_2CH_3$ and $Ar=3,5\text{-}C_6H_3Me_2$) turned purple. Warming the solution led to a change in its color from purple to gold. Using different spectroscopic and isotopic techniques, the group identified the purple

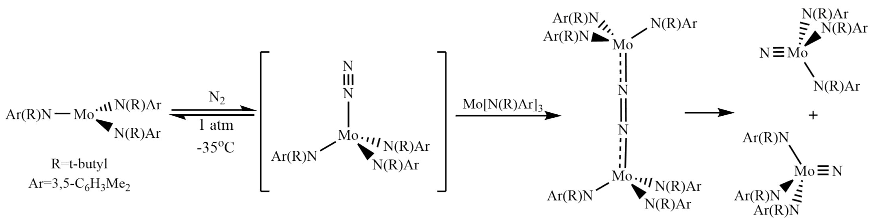

Figure 1.3: The reductive cleavage of N_2 using a Mo(III) complex

solution as the bimetallic bridging complex solution and the gold soltuion as the molybdenum nitride solution. The resultant metal-nitride complex did not go any further hydrogenation reactions due to the stability of the resulting M≡N bond.

1.3 Background & Present Study

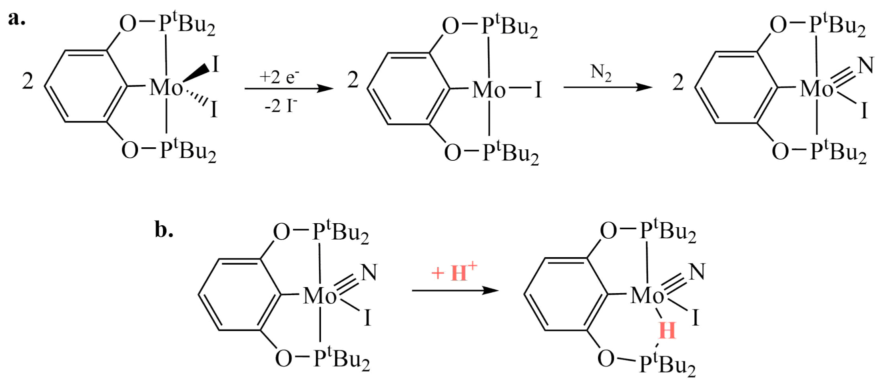

Figure 1.4: a. The reductive cleavage of N_2 using a ^{tBu}POCOP)MoI$_2$ complex, b. The protonation of (^{tBu}POCOP)MoIN

After successfully reducing N_2 to ammonia in 2003 using a molybdenum complex, Schrock and his colleagues attempted to couple this Mo center with a pincer ligand in hopes of achieving similar reduction reactions [6]. The formed complex cleaved N_2 forming a metal nitride, (^{tBu}POCOP)MoIN, which did not go any further reduction. Upon protonation, the proton was not added to the nitride but it is inserted between the Mo center and the phosphine of the pincer ligand. Nevertheless, Schrock was able to propose a novel pathway for N_2 reduction and cleavage which involves the formation of a bimetallic bridged complex.

Functionalization will almost always involve binding of N_2 to a transition metal center as a key step. Dinitrogen complexes are known for most of the transition metals, and they exhibit a variety of binding modes, among which terminal end-on (η^1-N_2) and bridging end-on (μ-N_2) coordination are prevalent.

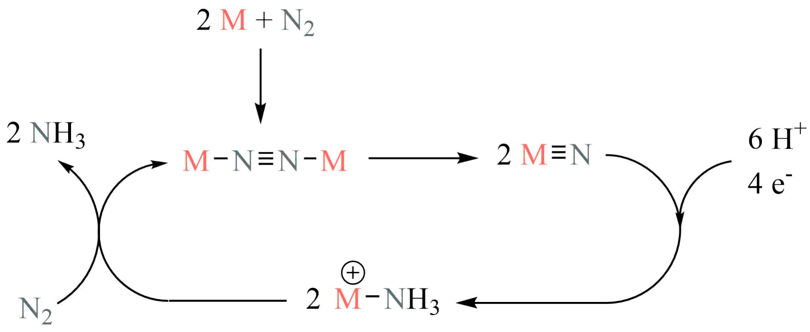

Figure 1.5: Alternative pathway for N_2 reduction to NH_3

Different binding modes can offer drastically different chemistries. For example, the terminal N_2 ligand is known to undergo electrophilic attack reactions that will be inhibited by bridging.

The direction and magnitude of the equilibrium between the terminal and bridging modes can thus control which mechanistic pathways are available in a particular system. However, the factors which determine whether a metal complex would prefer to form a terminal or a bridging N_2 complex are not addressed in the literature. Can the thermodynamics of terminal versus bridging binding modes be predicted?

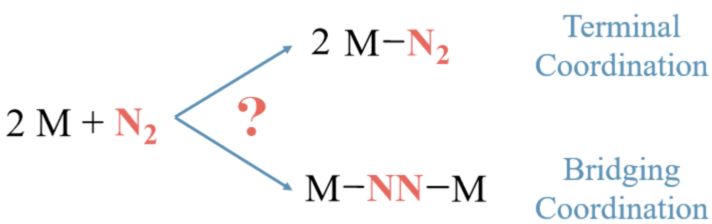

To address this gap in the literature, we will resort to quantum chemical methods and computational tools. In the next half of this chapter, we will briefly discuss the development of such quantum methods, specifically Density Functional Theory (DFT).

1.4 Introduction to Computational Chemistry

The origins of computational chemistry, a relatively novel field in science, can be traced back to the 1920s. Its history is woven into that of quantum mechanics, a body of laws that describe nature on the scale of the atom and subatomic particles. The articulation of Heisenberg's uncertainty principle, the solution of Schrödinger's equation for the hydrogen atom, and the postulation of the pi electron theory by Hückel opened many new research opportunities for the scientific community present at the time. By understanding the subatomic electronic and nuclear structure of chemical systems, scientists were able to explain and predict experimental observations such as spectra and reactivity. However, the extension of quantum chemical treatments to systems larger than the hydrogen molecule or helium atom frequently resulted in complex equations that were too tedious for scientists to solve manually. Not only were they time and energy demanding, but any mistake in the calculations could put off the calculation for days. Human error was simply too expensive. Fortunately, the invention of digital computers during the Second World War introduced new computational resources to science. This led to the emergence of the computational sciences, specifically computational chemistry. A calculation that would've once taken several researchers months to solve could now be done in a fraction of the time and effort.

$$\hat{H}|\Psi\rangle = E|\Psi\rangle$$

Time-independent Schrödinger Equation

$$i\hbar\frac{d}{dt}|\Psi(t)\rangle = \hat{H}|\Psi(t)\rangle$$

Time-dependent Schrödinger Equation

$$E\psi = -\frac{\hbar^2}{2\mu}\nabla^2\psi - \frac{q^2}{4\pi\varepsilon_o r}\psi$$

Schrödinger Equation for the Hydrogen Atom

Figure 1.6: Different Forms of the Schrödinger Equation

As mentioned earlier, many scientific advances were necessary to allow computational chemistry to grow as an independent field of science. The formulation of the Schrödinger equation in 1925 by Erwin Schrödinger is a key accomplishment of quantum mechanics and is the cornerstone of any computational treatment. This equation is to quantum mechanics what Newton's second law is to classical mechanics. It is a linear partial differential equation from which the wave function of a quantum mechanical system can be determined. This wave function allows us to describe the wave behavior of a particle and its quantum mechanical state. Although this equation could only be solved accurately for the hydrogen atom, approximate solutions can aid in describing larger molecular systems. The Self-Consistent Field (SCF) method, or the Hartree-Fock (HF) method, allows us to obtain these approximations. This method was first developed by Douglas Rayner Hartree in 1927 and was enhanced later by Vladimir Aleksandrovich Fock. The HF method involves selecting an approximate Hamiltonian, solving the Schrödinger equation to obtain a new set of molecular orbitals, then solving the Schrödinger equation again using these orbitals. This process is repeated until the results converge and the lowest possible energy for the system is obtained. Several iterations may be required before reaching the lowest energy for a given system. According to the variational principle, the approximate wave function obtained by the HF method will always be higher in energy than the experimental ground state of the system.

In 1966, a Nobel prize in chemistry was awarded to Robert Mulliken for the development of Molecular Orbital (MO) theory [7]. This theory uses quantum mechanics to describe the electronic structure of molecules. According to this theory, electrons are distributed into different molecular orbitals of distinct energies that are distributed over the whole molecule. Unlike the previously used valence bond theory, MO theory describes these molecular orbitals as linear combinations of atomic orbitals (LCAOs). Atomic orbitals can come together and form molecular orbitals if they satisfy the following conditions: they have suitable symmetry that allows their interaction, they physically overlap in space, and they have similar energies. The number of total orbitals is conserved during the transformation from atomic orbitals (AOs) to MOs. For example, to form the hydrogen molecule we start with two individual hydrogen atoms, each with a single atomic orbital (AO) and an electron. After the hydrogen atoms approach each other and satisfy the conditions mentioned previously, two molecular orbitals are formed with two electrons. The MO wave function ψ_j is represented numerically by the equation below. It is the weighted sum of n atomic orbitals, χ_i. The coefficients, c_{ij}, represent the relative contribution of each AO to the MO and can be determined by plugging ψ_j into the Schrödinger equation and applying the variational principle. The Hartree-Fock method was initially used to determine the wave function of MOs.

$$\psi_j = \sum_{i=1}^{n} c_{ij}\chi_i$$

Figure 1.7: The Wave function of a Molecular Orbital

A few decades later, Walter Kohn and John Pople split a Nobel prize for the "development of density functional theory (DFT)" and the "development of computational methods in quantum chemistry", respectively [8]. DFT is a modelling method used to obtain approximate solutions of the Schrödinger equation for many-body systems. It utilizes functionals (functions of other functions) and approximations to determine the electronic structure of atoms, molecules, and solid materials. The Schrödinger equation for a many-body system is given below, where $\hat{\mathrm{T}}$ is the kinetic energy, $\hat{\mathrm{V}}$ is the potential energy potential energy from the external field due to positively charged nuclei, and $\hat{\mathrm{U}}$ is the electron–electron interaction energy. The simplest approach to solving such a complex equation would be to divide it into simpler single-body equations. However, since the $\hat{\mathrm{U}}$ term is inseparable, the solution of this equation remains complex and requires several approximations. One of the these approximations is the Born-Oppenheimer Ap-

$$\hat{H}\Psi = [\hat{T} + \hat{V} + \hat{U}]\Psi = \left[\sum_{i=1}^{N}\left(-\frac{\hbar^2}{2m_i}\nabla_i^2\right) + \sum_{i=1}^{N} V(r_i) + \sum_{i<j}^{N} U(r_i, r_j)\right]\Psi = E\Psi$$

Figure 1.8: The Schrödinger Equation for a Many-Body System

proximation, which separates the treatment of the electron wave functions from the nuclei wave functions. It assumes that the nuclei are fixed point masses with electrons moving around them. Another important approximation that DFT uses is treating the many electrons in the system as a single electron density. Simply put, this turns the many-body problem to a single-body one. The electron density of a state is the number of electrons per unit volume in that state. The nuclei in this case are considered as maxima in the electron density. These approximations simplify the solution of the Schrödinger equation reducing the time and effort required to solve it. The development of DFT is considered to be a milestone in the emergence of computational chemistry as an independent field of science.

Soon after its formulation, density functional theory found applications in solid-state physics in the 1970s. However, it was not considered accurate enough to perform quantum chemical calculations until the 1990s. Since then, DFT

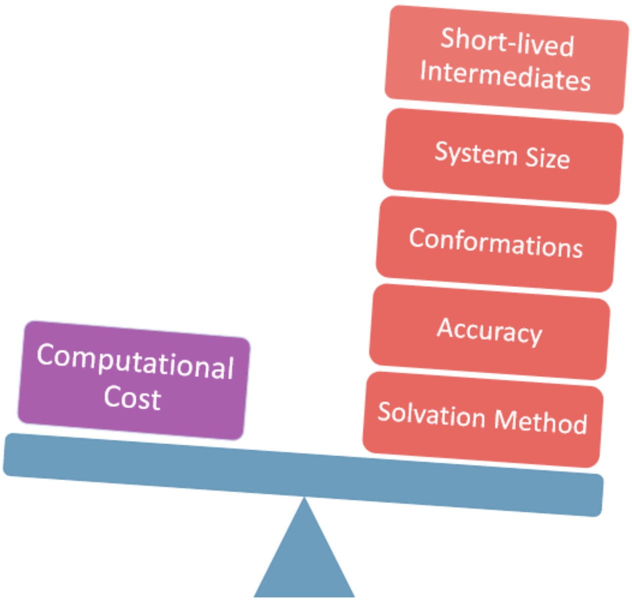

Figure 1.9: Challenges in Mechanism Elucidation of Homogeneous Catalytic Reactions

and other methods have provided evidence for electronic structure, and in some cases in predictions. It has had wide applications in drug discovery, along with computer-aided molecular design (CAMD) and molecular mechanics (MM). DFT has also been used to gather supplementary material for experimental observations. For example, DFT has aided the understanding of reaction mechanisms. Before the development of DFT, chemists faced many challenges in determining the correct mechanism of a reaction of interest. Some of these challenges are the presence of multiple elementary steps, competing reactions with similar energies as the reaction of interest, unknown reactive species in the reaction mixture, and highly reactive intermediates that can not be detected experimentally. Using DFT, chemists could explore the unseen and undetectable. It allowed chemists to plot potential energy surfaces, locate possible transition states, and determine lowest energy pathways for reactions. Researchers could now compare different geometries and conformations of the reactants and products and determine the most stable species present in their system. However, using DFT to elucidate reaction mechanisms does not come without its challenges and shortcomings. An important challenge computational chemists face is the constant struggle to balance accuracy and cost. Over the years, numerous methods have been developed to achieve higher levels of accuracy and consistency with experimental observations. Coupling these accurate methods with larger basis sets would be ideal if not for the high computing cost that would result as the size of the system under study increased. To avoid this high cost, chemists employ efficient approximations in the treatment of larger many-body systems. For example, CCSD (couple-cluster single-double) is a computational method that was developed by Fritz Coester and Hermann Kümmel in the 1950s. This method extends the HF molecular orbital method to construct multi-electron wave functions using special operators to account for electron correlation. Due to the high levels of accuracy this method was able to achieve at low computational efforts, it has been considered by many to be the "gold standard" of quantum chemistry [9]. However, as the system size increases, the accuracy of CCSD starts to diminish and approximations such as the domain-based local pair natural orbital (DLPNO) approximation are necessary to maintain high level of accuracy in larger systems.

Another challenge in mechanism elucidation using DFT is simulating experimental conditions as close to experiment as possible. Optimizing reaction conditions in homogeneous catalysis is an exhaustive process where many factors should be considered such as temperature, pressure, pH, and solvent choice. In many cases the solvent plays a crucial role in the progress of the reaction where it may be directly or indirectly involved in the reaction. In other cases, reactants or catalysts may change conformations depending on the solvent used which affects the accessibility of the active sites and therefore the progress of a reaction. It is very important that these experimental details are represented well in a computational simulation. For this reason, many solvation methods have been developed. While some are implicit solvation methods, which involve the introduction of individual solvent molecules into the system, other solvation methods such as SMD (Solvation Model based on Density) explicitly represent the solvent as a continuum into which the reactants are placed.

As the field of computational chemistry continues to grow in parallel with the rapid advances in technology, many methods and software are being developed to facilitate and speed up catalyst development. For instance, Morokuma and his colleagues recently reported the development of a computational approach which allows the exploration of a PES while avoiding user bias [10]. Human bias is an important factor that affects the quality of computational results and their accuracy. No matter how advanced a computational method is, it still relies on the data given to it by the user to generate results. Morokuma was able to avoid bias by developing the artificial induced reaction method (AFIR) to explore the full catalytic cycle of a hydroformylation process using a cobalt molecular catalyst. This method relies on a fully automated approach to locate and connect reaction minima with transition states along the PES. Other approaches relying on machine learning and artificial intelligence which aim at designing novel catalysts based on the libraries of available data are in the making. These algorithms can rapidly screen through the literature and detect patterns in synthetic procedures without human supervision. Chemists can then utilize these patterns to accelerate the synthetic process instead of entering a long process of trial and error. While experimentalists can perform high-throughput experiments to rapidly screen through reaction conditions, theoreticians will soon be able to perform high-throughput computations to design catalysts of different functions and properties [11].

1.5 Methods of Analysis and Inquiry

This study is based on theoretical studies but it is linked to available experimental data. All computations are carried out on the IBM high performance computer (HPC) at AUB and that in Rutgers University. The quantum chemical software Gaussian 16 is used [12]. Geometry optimization and frequency calculations are done using the popular density functional theory (DFT) level M06L in gas phase. If needed other levels of theory may be used such as M06, wB97XD, and b3LYP. The thermal and entropy terms to the Gibbs free energy are computed at 298.15 K and 1 M concentrations of the metal complexes and a pressure of 1 atm for N2.The basis set used for main group elements and first row transition metal is 6-311G(d,p). The remaining transition metals carry SDD relativistic effective core potentials (ECP) with an addition of an f-function from the LANL08(f) basis set. Final energies are obtained from single point calculations in a polarizable continuum (SMD) representing toluene as solvent using the gas phase geometries and the def2-tzvp basis set implemented in Gaussian on the non-metals and the def2-qzvp with ECPs on the heavier metals as provided on the Basis Set Exchange website [13]. Natural bonding analysis is carried out on the NBO 3.1 program included in the Gaussian 16 package [14]. We utilize the Gaussview 5 visualization software to visualize optimized geometries, vibration frequencies and intrinsic reaction coordinates (IRCs) [15]. Molecular orbitals will be visualized from formcheck files generated by Gaussian using the graphical program Chemcraft [16].

Chapter 2

DFT Studies on Terminal versus Bridged N_2 Binding in Transition Metal Chemistry

2.1 Computational Approach

In this chapter, we focus on the equilibrium between the two binding modes, presented in the following equation.

$$2\,MN_2 \xrightleftharpoons{2\,\Delta G^{o}_{eq}} MNNM + N_2 \ (1)$$

We use DFT to elucidate the factors that govern the direction of this equilibrium. The complexes of interest are pincer-ligated complexes with previous experimental data. We calculate the free energy (ΔG^{o}_{eq}) of the equilibrium in eq1 for each complex and its analogues. The ΔG^{o}_{eq} values are normalized to one M-N bond for comparison's sake. From the computed data and detailed molecular orbital (MO) analysis, we are able to set up a model which enables us to predict the binding mode of the metal centers to N_2 using only the π bond order (π-BO).

Several factors may affect the sign and magnitude of ΔG^{o}_{eq}. These factors may be simply divided to outer-sphere electrostatic interactions between the ligands, which may be attractive or repulsive, and the electronic interactions between the metal centers and the N_2 molecule. Theoretically, we can separate these factors by constructing two thermodynamic cycles, one for the η^1-N_2 binding and the other for the μ-N_2 binding of N_2 to the metal centers. These cycles are outlined in Figure 2.3. Both cycles start with a metal fragment with a free coordination cite.

In **Cycle 1**, the electronic energy of N_2 coordination is split into two terms: i. A distortion energy ($\Delta E'_{dist1}$) required for the ligands surrounding the metal to rearrange themselves to M'; and ii. a "vertical" (adiabatic) energy corresponding to the binding step of N_2 to M' without any further geometry changes. **Cycle**

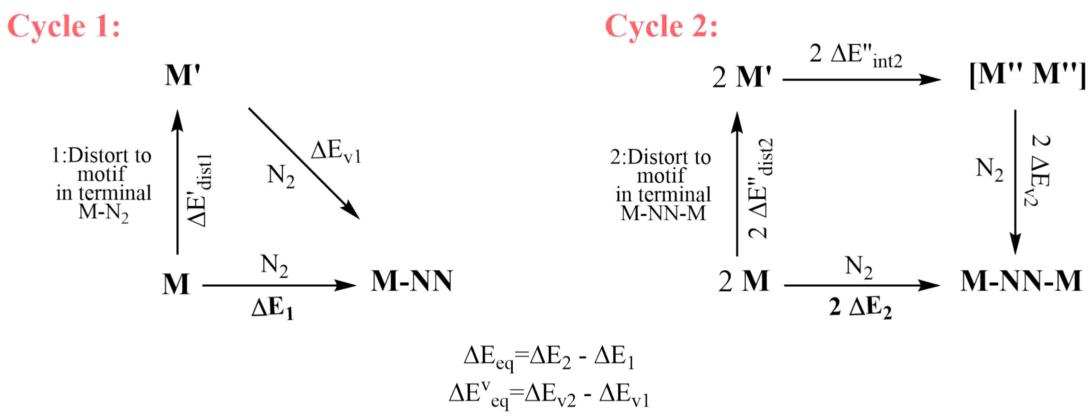

Figure 2.1: Thermodynamic cycles for N_2 coordination to a metal fragment

2 splits the electronic energy into three terms: i.ΔE'$_{dist2}$, the energy needed to distort two metal fragments, M, to M"; ii. ΔE"$_{int2}$, the energy needed to combine two distorted metal fragments into a bimetallic [M"M"] adduct to match their position and spin states in the bridged complex; and iii.ΔE"$_{v2}$, the energy of the N−2 insertion into the [M"M"] adduct. To understand the free energy of the equilibrium, we consider the difference ΔE^v_{eq}=ΔE_{v2}-ΔE_{v1}. This difference accounts for the electronic properties that may drive the equilibrium towards terminal coordination or bridging coordination. Comparisons between ΔE^v_{eq} and ΔG^o_{eq} may reveal whether outer-sphere effects and entropy drive the mode of coordination or electronic effects determine it.

2.2 Results and Discussion

We focus our calculations and discussion on pincer-ligated complexes having previous experimental data in the literature. We then vary the metal and in some cases the ligands to study the effect of different structural and electronic properties on the equilibrium energy.

2.2.1 Octahedral d^5 & d^6 Pincer Complexes

We first consider the the molybdenum(0) (bis)dinitrogen fragment trans (^{tBu}PNP)Mo(N_2)$_2$, $\mathbf{t}^1$-Mo. Nishibayashi and colleagues discovered $\mathbf{t}^1$-Mo which exhibited catalytic properties for N_2 reduction to NH_3 [17]. They identified the catalytic precursor to be the dinitrogen bimetallic bridged complex. This bridging complex was experimentally found to be stable when dissolved in THF under 1 atm N_2. Its stability was confirmed using Raman and ^{15}N NMR spectroscopy. We setup the equilibrium and cycles for $\mathbf{t}^1$-Mo and presented the data in Table 2.1. ΔG^o_{eq} was determined to be -2.9 kcal/mol, favoring bridging coordination

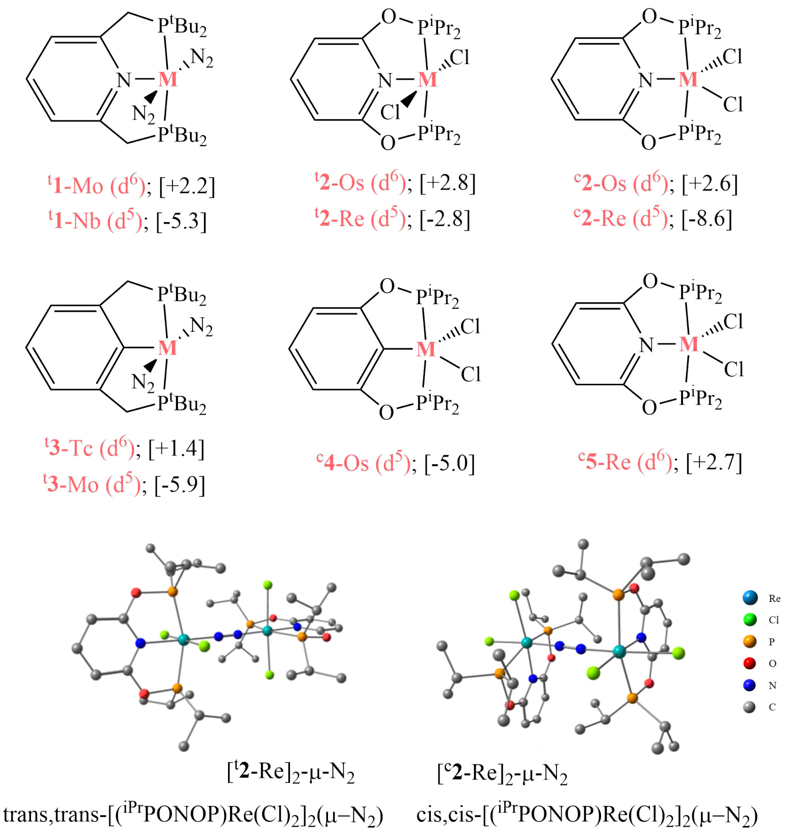

(a) Numbers in brackets are the E^{v}_{eq} values defined Figure 2.6 in kcal/mol.
The molecular displays illustrate isomers of bridging complexes.

Figure 2.2: Investigated Octahedral Transition Metal Fragments with d^5 and d^6 metal centers

and agreeing with the experimental observations. However, ΔE^{v}_{eq} is positive, +2.2 kcal/mol, indicating that electronic factors favor the μ-N_2 coordination over η^1-N_2 coordination and the M-N_2 bond is stronger in the former mode of coordination. There was a minimal difference between the distortion energies $\Delta E'_{dist1}$ and $\Delta E''_{dist2}$, 0.9 kcal/mol and 1.4 kcal/mol, so their effects calcel out. The slightly favored ΔG^{o}_{eq} was attributed to the outer-sphere interaction energy between the two distorted fragments, $\Delta E''_{int2}$ (-5.4 kcal/mol), due to the dispersion forces between the distorted metal fragments. The M06-L level of theory was designed to treat non-covalent interactions between atoms [18, 19]. To verify that the favored $\Delta E''_{int2}$ was in fact due to the weak dispersion forces between the distorted metal fragments we calculate this interaction energy, $\Delta E''_{int2}$, using a functional which does not account for such interactions. The B3LYP level of theory gives $\Delta E''_{int2}$= +1.8 kcal/mol and ΔG^{o}_{eq}= +5.6 kcal/mol. When dispersion terms [20, 21] were later added using B3LYP, the negative $\Delta E''_{int2}$ (-7.4

Table 2.1: Terminal versus bridging N_2 binding in octahedral d^5 and d^6 complexes.$^{(a)}$

	Cycle 1		Cycle 2				Eq 1			
	ΔE_{dist1}	ΔE_{v1}	ΔE_{dist}	ΔE_{int2}	ΔE_{v2}	d^n-d^n	ΔE^{v}_{eq}	ΔE_{eq}	ΔG^{o}_{eq}	ΔBO^{π}_{eq}
^{t}**1**-Nb d^5	1.9	-30.9	3.3	-5.6	-36.2	$(2\pi_\mu)^4(\delta_\mu)^4(3\pi^*_\mu)^2$	-5.3	-9.5	-9.3	1
^{t}**1**-Mo d^6	0.9 ^{b}	-37.7	1.4	-5.4	-35.4	$(2\pi_\mu)^4(\delta_\mu)^4(3\pi^*_\mu)^4$	+2.2	-2.6	-2.9	0
^{Me}**1**-Mo	1.2	-35.7	1.0	-1.0	-33.0	$(2\pi_\mu)^4(\delta_\mu)^4(3\pi^*_\mu)^4$	+2.8	+1.5	+1.3	0
^{t}**2**-Re d^5	7.8	-33.2	7.8	-4.3	-35.9	$(2\pi_\mu)^4(\delta_\mu)^4(3\pi^*_\mu)^2$	-2.8	-7.0	-5.0	1
^{t}**2**-Os d^6	7.8	-42.9	7.7	-5.4	-38.4	$(2\pi_\mu)^4(\delta_\mu)^4(3\pi^*_\mu)^4$	+4.5	-1.0	+0.8	0
^{c}**2**-Re d^5	10.6	-37.2	10.6	-7.2	-42.9	$(2\pi_\mu)^4(\delta_\mu)^4(3\pi^*_\mu)^2$	-5.7	-12.9	-8.0	1
^{c}**2**-Os d^6	10.9	-43.4	12.3	-8.5	-40.8	$(2\pi_\mu)^4(\delta_\mu)^4(3\pi^*_\mu)^4$	+2.6	-4.6	-0.7	0
^{t}**3**-Mo d^5	1.0	-22.4	2.1	-5.1	-28.3	$(2\pi_\mu)^4(\delta_\mu)^4(3\pi^*_\mu)^2$	-5.9	-9.9	-10.2	1
^{t}**3**-Tc d^6	1.2	-27.9	1.4	-5.1	-26.5	$(2\pi_\mu)^4(\delta_\mu)^4(3\pi^*_\mu)^4$	+1.4	-3.5	-1.3	0
^{c}**4**-Os d^5	19.1	-31.6	23.3	-7.7	-36.6	$(2\pi_\mu)^4(\delta_\mu)^4(3\pi^*_\mu)^2$	-5.0	-8.5	-5.3	1
^{c}**5**-Re d^6	10.8	-44.9	11.4	-7.0	-42.2	$(2\pi_\mu)^4(\delta_\mu)^4(3\pi^*_\mu)^4$	+2.7	-3.7	-1.6	0

$^{(a)}$ M06-L results in kcal/mol. The ΔE terms are defined in Figure 2.6. "d^n-d^n" is the occupancy of the valence MOs in the bridging complex as defined in Figure 2.8. ΔBO^{π}_{eq} is defined in Figure 2.9. $^{(b)}$ Distortion energies are given relative to the *trans*-$(N_2)_2$ fragment which is 10 kcal higher than the *cis*-$(N_2)_2$-isomer.

kcal/mol) and ΔG^{o}_{eq} (-3.5 kcal/mol) were restored.

We further investigate the effect of outer-sphere interactions on the direction of the equilibrium by substituting the bulky *tert*-butyl groups of ^{t}**1**-Mo with smaller methyl groups. The results of this substitution are presented in entry ^{Me}**1**-Mo in Figure 2.8. The substitution has little effect on ΔE^{v}_{eq} (2.2 vs 2.8 kcal/mol) does not affect the interaction of dinitrogen with the metal center. The Mo-N_2 bond remains stronger than each bridging bond. However, $\Delta E''_{int2}$ is reduced from -5.4 to -1.0 kcal/mol, so the slightly positive ΔG^{o}_{eq} (+1.3 kcal/mol) is due to the positive ΔE^{v}_{eq}. It is interesting that substituting the groups on the phosphines with less bulky groups led to less favored bridging, contrary to expectations. Bulkier groups have traditionally been used to prevent dimerization through the formation of M-M bonds or single-atom bridges, but in this case, they enhance the bridging of the two metals via N_2.

We consider a second octahedral system consisting of a d^5 rhenium(II) fragment, **2**-Re. Bruch et al were the first to synthesize a rhenium based catalyst able to reduce N_2 to NH_3 [22]. The *trans,trans* isomer of the dinitrogen bimetallic bridged complex $[(^{iPr}PONOP)ReCl_2]_2(\mu\text{-}N_2)$shown in Figure 2.7 was initially isolated. This complex isomerizes upon heating to the *cis,cis* isomer also shown in the molecular models. No terminal η-N_2 complex was detected experimentally under an N_2 atmosphere, so we expect the equilibrium to lie to right.

Starting with the *trans* isomer of the **2**-Re fragment, the ΔG^{o}_{eq} of the equilibrium going from the doublet spin state terminal N_2 adduct to the triplet state bridging complex is -5.0 kcal/mol (^{t}**2**-Re in Table 2.1). As seen experimentally, ΔG^o_{eq} was computed to be even more negative, -8.0 kcal/mol, for the *cis*-isomer. ΔE^v_{eq} for the d^5 ^{t}**2**-Re and ^{c}**2**-Re complexes is negative, -2.8 and -5.7, respectively. This indicates that the M-N bonds in the bridging complexes are intrinsically stronger than the M-N bond found in the terminal ones. These findings should also apply to the isoelectronic octahedral d^5-Re system with a different pincer ligand that was recently reported by Schneider to split N_2 via an N_2-bridged intermediate [23].

For a deeper understanding of the factors that may influence the direction and magnitude of ΔG^o_{eq} of the equilibrium under study, we consider several derivatives of **1**-Mo and **2**-Re. These deserves are designed to preserve overall charge neutrality and general structure. Table 2.1 presents the data for complexes isostructural to **1**-Mo supported by neutral pyridyl ^{tBu}PNP and its anionic analogue with a phenyl backbone ^{tBu}PCP. We also consider those isostructural to **2**-Re supported by ^{iPr}PONOP and the anionic ^{iPr}POCOP. Although the metals in the considered derivatives have oxidation states ranging from 0 to III, their d-electron count remains either 5 or 6 electrons.

The first ^{t}**1**-Mo variant is the ^{t}**1**-Nb complex with a Nb(0), a group V metal, center. The second variant of the same complex is the ^{t}**3**-Mo complex with a Mo(I) metal center and the ^{tBu}PCP ligand. Similar to the previous d^5 metal complexes considered, ^{t}**1**-Nb and ^{t}**3**-Mo both afford ΔE^v_{eq} less than zero, -5.3 and -5.9 respectively. On the other hand, ^{t}**3**-Tc, a d^6 analogue of ^{t}**3**-Mo has a positive ΔE^v_{eq}: +1.4 kcal/mol. We continue our investigation to include the variants of the **2**-Re isomers. Replacing the d^5-Re(II) metal center with d^6-Os(II) in ^{t}**2**-Re and ^{c}**2**-Re yielded positive ΔE^v_{eq} in ^{t}**2**-Os and ^{c}**2**-Os: +4.5 and +2.6 kcal/mol, respectively. The d^5-Os(III) ^{iPr}POCOP analogue of ^{c}**2**-Os, ^{c}**4**-Os, has a ΔE^v_{eq}= -5.0 kcal/mol and the d^6 ^{c}**5**-Re with a ^{iPr}PONOP pincer ligand, a chloride, and an N_2 ligand has ΔE^v_{eq}= +2.7 kcal/mol.

The components of Cycle 1 and Cycle 2 shown in Figure 2.8 display noticeable variations as changes are imposed on the metals and ligands, all the while preserving the overall neutrality of the complexes. However some trends appear in the ΔG^o_{eq} and ΔE^v_{eq} values. ΔG^o_{eq} is within 3 kcal/mol of ergoneutral in all d^6 systems, while they are significantly more exergonic for the d^5 systems. The ΔE^v_{eq} show an even sharper division where ΔE^v_{eq} is systematically positive for d^6 complexes and negative for d^5 complexes, with averages of +2.2 and -5.5 kcal/mol, respectively. These resulst are independent of DFT level of theory, basis set, solvation, and the absence or presence of dispersion effect factors.

2.2.2 A π-Bond Order Model

The trends seen in the ΔE^v_{eq} values of Table 2.1 indicate the presence of electronic effects that favor bridging N_2 coordination in d^5 complexes and not in d^6 ones. To elucidate the origin of this effect, we consider the π-MOs in the octahderal terminal and bridging dinitrogen complexes of the symmetrical d^6 fragment [$HRe(NH_3)_4$]. We choose the ammonia and hydride ligands since they do not permit π-MO delocatization beyond the M-N_2 entity and therefore afford clear MO representations. Such delocalization is seen in the complexes of Table 2.1 and are known to hinder MO analysis of similar complexes [24, 25].

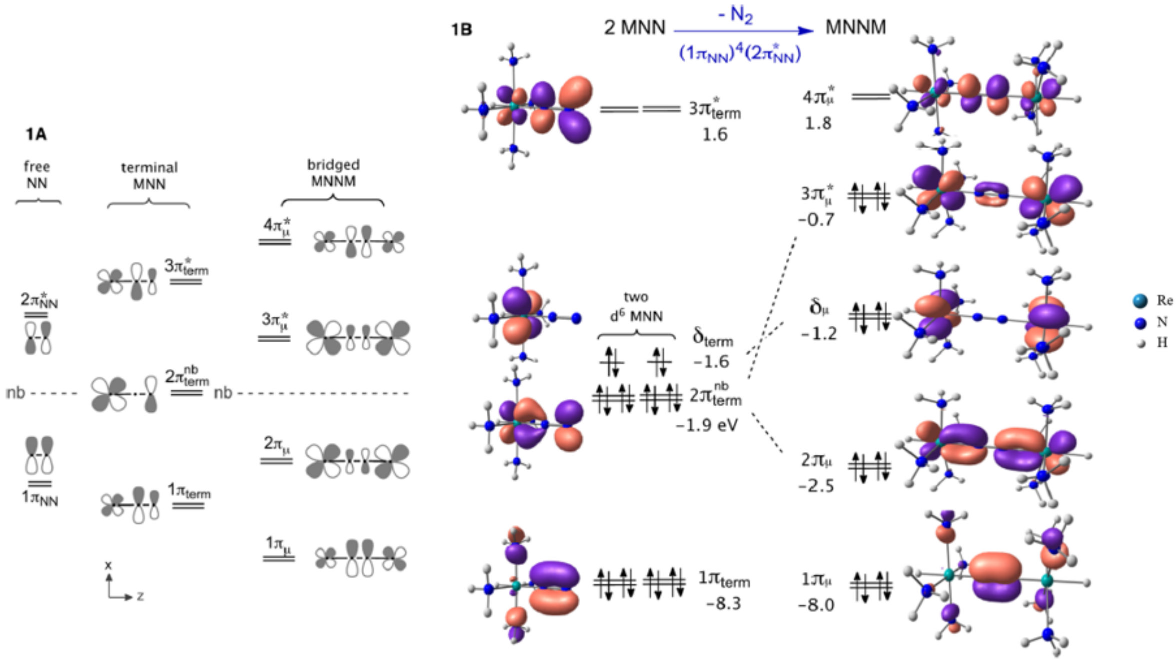

Figure 2.3: Schematic π-MOs in NN, MNN and MNNM, and Kohn-Sham MOs of the terminal and bridging N_2 complexes of the fragment d^6-[$HRe(NH_3)_4$]; MO energies in eV.

Part 1A of Figure 2.8 first shows the π-MOs of a free N_2 molecule: a pair of bonding π-MOs, $1\pi_{NN}$, and a pair of antibonding π-MOs, $2\pi^*_{NN}$. The four electrons present in the system occupy $1\pi_{NN}$ yielding a π-bond order (BO^π) of 2. In the terminal end-on M-NN complex, two d-orbitals are introduced from the metal center. These orbitals have suitable symmetry to interact with the free N_2 π-MOs, yielding a total of three pairs of π-symmetry orbitals. Similar to the simpler allyl group where the individual atomic orbitals (AOs) are similar in energy, these three pairs of MOs have the following characters: $1\pi_{term}$ is in the all in-phase bonding MO, $2\pi^{nb}_{term}$ is the non-bonding MO with a single node on the central atom, and $3\pi^*_{term}$ is the out-of-phase antibonding with two nodal planes.

Figure 1B shown on the right hand side shows the Kohn-Sham π-MOs for the ReNN moeity of [$HRe(NH_3)_4(N_2)$], along with the metal based d_{xy} orbital of δ symmetry with respect to the Re-N_2 bond (δ_{term}). The π-MOs have uneven atomic contributions due to the difference in electronegativities of the nitrogen

Table 2.2: M-N and N-N bond lengths (in Å) and N-N stretching vibration frequencies (in cm^{-1}) for selected octahedral complexes from Table 2.1$^{(a)}$

		Terminal $M\text{-}N_2$			Bridging $M\text{-}N_2$			Eq 1	
Fragment	$d\pi$/M	r_{MN}	r_{NN}	ν_{NN}	r_{MN}	r_{NN}	ν_{NN}	Δr_{MN}	Δr_{NN}
^{t}**1**-Nb d^5	3	2.113	1.135	2026	1.973	1.189	1678	-0.140	0.054
^{t}**1**-Mo d^6	4	2.018	1.134	2070	2.012	1.153	1976	-0.006	0.019
^{t}**2**-Re d^5	3	1.975	1.128	2129	1.923	1.155	1940	-0.055	0.027
^{t}**2**-Os d^6	4	1.935	1.124	2184	1.944	1.134	2173	0.032	0.010
^{c}**2**-Re d^5	3	1.973	1.131	2093	1.909	1.175	1843	-0.064	0.044
^{c}**2**-Os d^6	4	1.912	1.130	2142	1.950	1.144	2101	0.015	0.014
^{t}**3**-Mo d^5	3	2.119	1.127	2094	1.993	1.169	1831	-0.126	0.042
^{t}**3**-Tc d^6	4	2.041	1.126	2137	2.053	1.140	2067	0.012	0.014

$^{(a)}$ Complexes described in Figure 2.7. $d\pi$/M is the number of d electrons provided by each metal to the π-moiety.

and rhenium atoms. Starting from the bottom of the diagram, the $1\pi_{term}$ is mainly localized on the two nitrogen atoms of Re-NN. The second MO consists mostly of the metal d-orbital and the distal nitrogen p-orbital, with minor contributions from the proximal nitrogen. This orbital is similar to the non-bonding π orbital found in the allyl group, so by analogy we name the MO in ReNN also as "non-bonding" ($2\pi^{nb}_{term}$). This orbital is followed by the δ metal d-orbital, which in turn is followed by an all-antibonding $3\pi^{*}_{term}$ having large contributions from the nitrogen atoms and smaller contributions from the metal. Dubois and Hoffmann were the first to notice the analogy between the well known allyl group and the valence π-MO in $M\text{-}N_2$ [26].

According the allyl analogy of π-bonding in $M\text{-}N_2$, the population of the $2\pi^{nb}_{term}$ in d^5 and d^6 terminal N_2 complexes, $(2\pi^{nb}_{term})^3$ and $(2\pi^{nb}_{term})^4$ respectively, should not affect the M-N (r_{MN}) and N-N (r_{NN}) bond distances. This is contrary to the traditional backbonding model that is dominated by in-phase mixing between filled metal d-AOs and π^{*}_{NN}. The later model expects that upon N_2 complexation with the metal center, the M-N bond would be shorter than the N-N bond which would elongate in d^6. However, this is not supported by the computed data as shown in Table 2.2.

In the four pairs of terminal congeners shown in Table 2.2, the M-N bond distances, r_{MN}, are significantly shorter (by 0.07 Å in average) for the d^6 complexes than they are for their d^5 congeners. On the other hand, the r_{NN} values are not dependent on the occupancy of the $2\pi^{nb}_{term}$ where all four d^6 complexes have *shorter* r_{NN} (seen in Δr_{NN}) and slightly *higher* NN stretching vibrational frequency ν_{NN} (by 43 to 55 cm^{-1}) than their d^5 counterpart. The M-N and N-N bond distances cannot be explained from the π-MO model alone. Interestingly, the allyl-like analogy allows us to prescribe a formal BO^{π}=2 due to the filled

MOs in $1\pi_{term}$. This is independent of the occupancy of $2\pi_{term}^{nb}$. Since $1\pi_{term}$ is mostly concentrated on the NN group, the following Lewis is representative of the BO^{π}: M-N≡N. This structure describes the relatively short r_{NN} distances computed for the terminal complexes.

We know consider the bridging N_2 complexes, which are treated differently. Focusing on the MNNM core, each metal or nitrogen atom contributes 2 π-AOs to the system yielding a total of four double degenerate π_{μ}-MOs: two with bonding ($1\pi_{\mu}$ and $2\pi_{\mu}$) and two with antibonding character ($3\pi_{\mu}^{*}$ and $4\pi_{\mu}^{*}$) as displayed in part 1A of Figure 2.8. The Kohn-Sham MOs of the model system $[HRe(NH_3)_4]_2(\mu\text{-}N_2)$ show $1\pi_{\mu}$ to be concentrated on the two central nitrogen atoms, similar to $1\pi_{term}$ in M-N_2. Unlike the $2\pi_{term}^{nb}$ in the η-N_2 complex, the $2\pi_{\mu}$ MO has significant in-phase interaction between the metal AO and the AO of the nitrogen adjacent to it. Consistent with the bonding character shown in the orbital structure, the energy of $2\pi_{\mu}$ is 1.3 eV below the δ_{μ} orbital formed from two formally non-degenrate combinations of the d_{xy} AOs of the metals. The $3\pi_{\mu}^{*}$ MOs are mostly localized only the metal with minor contributions from the nitrogen AOs. The energy of these $3\pi_{\mu}^{*}$ MOs also confirms their antibonding character by being 0.5 eV higher than that of the δ_{μ}. This is also shown by the presence of additional π-nodes between the metals and the nitrogens. The last π-MO to be considered is $4\pi_{\mu}^{*}$ with all π-antibonding interactions and higher atomic coefficients from the nitrogens than the metals. Since there are no non-bonding π-MOs, the BO^{π} in the μ-N_2 bridging complexes is dependent on the total electrons in the π-symmetry supplied by the metals ($d\pi$/M in Table 2.2). In the d^6-d^6, the N_2 provides 4 electrons and each metal contributes 4 electrons to the total π-electron configuration: $(1\pi_{\mu})^4(2\pi_{\mu})^4(3\pi_{\mu}^{*})^4(4\pi_{\mu}^{*})^0$. The BO^{π} in this case is 2 due to the filled $1\pi_{\mu}$. Since the $3\pi_{\mu}^{*}$ orbitals are filled, the filled $2\pi_{\mu}$ orbitals do not contribute to the BO^{π} and their effects cancel out. A suitable Lewis-structure for the d^6-d^6 complexes would be: M-N≡N-M. In the d^5-d^5, each metal donates three electrons to the total π-system leading to the following π-electron configuration: $(1\pi_{\mu})^4(2\pi_{\mu})^4(3\pi_{\mu}^{*})^2(4\pi_{\mu}^{*})^0$. The partial depletion of the $3\pi_{\mu}^{*}$ MOs while $2\pi_{\mu}$ remains full increases the BO^{π} to 3. When determining a suitable Lewis-structure, the position of the nodes in $3\pi_{\mu}^{*}$ between the metal centers and the adjacent nitrogen atoms play a significant role. Since the $3\pi_{\mu}^{*}$ is not full, the M-N bonds become relatively shorter compared to those in the d^6-d^6 systems and an adequate Lewis structure is: M=N=N=M. This is displayed in the of Table 2.2 where the r_{MN} values are 0.02 to 0.06 Å *shorter* in the d^5-d^5 systems than the d^6-d^6 ones.

We can now assign a new term, ΔBO_{eq}^{π}, to express the change the in π-bond order when going from the left side of the equilibrium to the right i.e. from the terminal to the bridging complexes. As mentioned earlier, the filled non-bonding $2\pi_{term}^{nb}$ ensures that all terminal complexes, whether with d^6 or d^5 centers, will have a fixed BO^{π} of 2. Going from the terminal N_2 complex to the bridging N_2 complex, the $2\pi_{term}^{nb}$ term splits into bonding and antibonding π-MOs. The BO^{π}

may now change depending on the occupancy of the $2\pi_\mu$ and the $3\pi^*_\mu$ MOs as shown in Figure 2.9.

Figure 2.4: Relating the π-electron configuration of MNNM to ΔBO^{π}_{eq} and ΔE^{v}_{eq} of eq1.$^{(a)}$

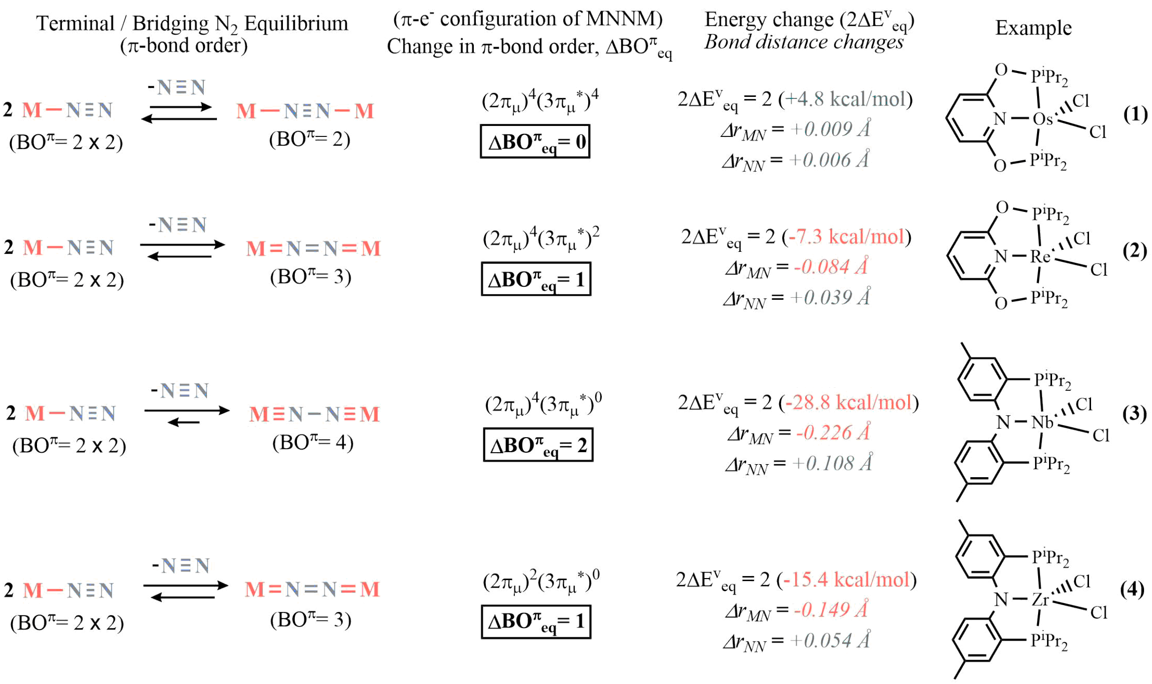

(a) Δr_{MN} and Δr_{NN} are the differences in the MN and NN bond distances in the bridging and terminal N_2 complexes. Energy and bond distance values are the averages of the octahedral complexes in Table 2.2-2.4 .

For the d^6 systems, the BO^{π} does not change when going from terminal η-N_2 complexes to bridging μ-N_2 complexes. In this case, the BO^{π} remains 2, so the ΔBO^{π}=0 (eq1 in Figure 2.11). On the other hand, in d^5 systems, one extra π-bond is created upon conversion from MNN to MNNM and ΔBO^{π}=1 (eq2 in Figure 2.9).

We can see the structural implications of the ΔBO^{π} in both d^5 and d^6 systems in Table 2.2. For the d^6 systems, the MN and NN bonds experience a minor *stretch* in bond distances going from MNN to MNNM: Δr_{MN}= 0.013 Å and Δr_{NN}= 0.014 Å, on average. In contrast, bridging in the d^5 systems causes noticeable *contraction* in r_{MN} and lengthening in r_{NN} compared to the terminal complexes: Δr_{MN}= -0.097 Å and Δr_{NN}= 0.042 Å, on average.

This π-BO approach for rationalizing the direction of eq 1 taken for octahedral d^5 and d^6 complexes should be applicable to any metal N_2 complex. In the following sections we explore other d^n configurations and coordination numbers.

2.2.3 Octahedral d^4-d^1 Complexes

The above MO analysis predicts that the MNNM moiety can have a maximum BO$^\pi$ of 4 if the bonding $2\pi_\mu$ MOs were full and the antibonding $3\pi_\mu^*$ were empty. A suitable Lewis structure to describe this situation would be that similar to butadiyne: M≡N-N≡M. This case is presented in eq3 of Figure 2.9 where ΔBO$^\pi$ = 2 and the equilibrium is expected to be strongly shifted to the right. This scenario can theoretically be achieved in octahedral d^4, d^3 and d^2 metal systems, depending on the occupancy of the non-bonding δ_μ MOs. We considered the fragments present in Figure 2.10 and present their data in Tables 2.3 and 2.4.

Figure 2.5: Fragments investigated for terminal versus bridging N_2 binding in octahedral d^4 – d^1 complexes in Table 2.3

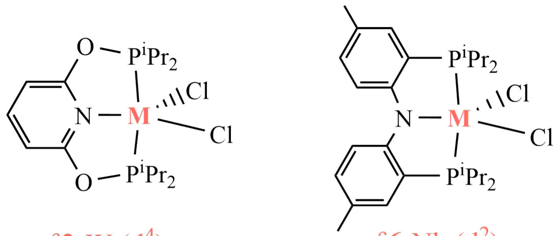

^{c}**2**-W (d^4); ^{c}**2**-Ta (d^3)

^{c}**6**-Nb (d^2); ^{c}**6**-Zr (d^1)

Table 2.3: Terminal versus bridging N_2 binding in octahedral d^4 – d^1 complexes.$^{(a)}$

	Cycle 1		Cycle 2				Eq 1			
	ΔE_{dist1}	ΔE_{v1}	ΔE_{dist2}	ΔE_{int2}	ΔE_{v2}	d^n-d^n	ΔE^{v}_{eq}	ΔE_{eq}	ΔG^{o}_{eq}	ΔBO^{π}_{eq}
^{c}**2**-W d^4	14.5	-38.3	27.1	-5.9	-64.2	$(2\pi_\mu)^4(\delta_\mu)^4(3\pi^*_\mu)^0$	-25.9	-19.2	-14.6	2
^{c}**2**-Ta d^3	10.8	-31.1	19.0	-12.1	-56.6	$(2\pi_\mu)^4(\delta_\mu)^2(3\pi^*_\mu)^0$	-25.5	-29.4	-24.0	2
^{c}**6**-Nb d^2	15.2	-20.0	33.6	-7.3	-55.0	$(2\pi_\mu)^4(\delta_\mu)^0(3\pi^*_\mu)^0$	-35.0	-23.9	-17.8	2
^{c}**6**-Zr d^1	5.0	-17.0	9.0	-2.1	-32.5	$(2\pi_\mu)^2(\delta_\mu)^0(3\pi^*_\mu)^0$	-15.5	-13.6	-6.5	1

$^{(a)}$ M06-L results in kcal/mol. The ΔE terms are defined in Figure 2.6. "d^n-d^n" is the occupancy of the valence MOs in the bridging complex as defined in Figure 2.8. ΔBO^{π}_{eq} is defined in Figure 2.9.

The first entry, ^{c}**2**-W, in the table of Figure 2.12 is a d^4 analogue of the d^5 ^{c}**2**-Re and d^6 ^{c}**2**-Os metal fragments. The [(^{iPr}PONOP)WCl$_2$] fragment has a triplet state ground state with a distorted trigonal bipyramidal geometry in which the Cl-W-Cl angle is 145^o. Similarly, the terminal N_2 tungsten complex has a triplet ground state, with the lowest closed shell singlet state 11.2 kcal/mol higher than the ground state. However, upon conversion from the terminal η-N_2 complex to the [^{c}2-W]$_2$(μ-N_2) bridged complex, the ground state changes spin state from a triplet to a singlet state corresponding to the following electron figuration:

Table 2.4: M-N and N-N bond lengths (in Å) and N-N stretching vibration frequencies (in cm^{-1}) for octahedral d^4 – d^1 complexes in Table 2.3.[(a)]

		Terminal M-N_2			Bridging M-N_2			Eq 1	
Fragment	dπ/M	r_{MN}	r_{NN}	ν_{NN}	r_{MN}	r_{NN}	ν_{NN}	Δr_{MN}	Δr_{NN}
^{c}**2**-W d^4	**2**	1.996	1.141	2017	1.831	1.239	1512	-0.165	0.098
^{c}**2**-Ta d^3	**2**	2.086	1.141	1966	1.871	1.255	1457	-0.215	0.114
^{c}**6**-Nb d^2	**2**	2.178	1.124	2120	1.879	1.237	1457	-0.299	0.113
^{c}**6**-Zr d^1	**1**	2.322	1.122	2142	2.173	1.177	1786	-0.149	0.055

[(a)] Complexes described in Figure 2.10. dπ/M is the number of d electrons provided by each metal to the π-moiety.

$(2\pi_\mu)^4(\delta_\mu)^4(3\pi^*_\mu)^0$. This electron configuration is 8.5 kcal/mol lower than the quintet state of electron configuration: $(2\pi_\mu)^4(\delta_\mu)^2(3\pi^*_\mu)^2$, observed in other similar systems [27]. We expect that the bridged complex have the Lewis structure: M≡N-N≡M, which was supported by the optimized geometry's M-N and N-N bond lengths. The M-N bond lengths undergo significant shortening (Δr_{MN}=-0.165 Å) while the N-N bond length undergoes lengthening (Δr_{NN}=0.098 Å). While the formation of the terminal η-N_2 complex does not require a change in spin state, it does require major distortion of the free metal fragment with ΔE_{dist1}= 14.5 kcal/mol (Table 2.3). The formation of the μ-N_2 bridging complex not only involves major changes in geometry but also a change in spin state ($^3T \rightarrow ^1S$), affording a high ΔE_{dist2}= 27.1 kcal/mol). Considering only electronic factors present in the system, ΔE^v_{eq} = -25.9 kcal/mol, fully consistent the the formation of two new π-bonds and indicating very favorable electronic interactions. The effect of the considerable difference between the distortion energies can still be see in ΔG^o_{eq} (-14.6 kcal/mol) which is much less than ΔE^v_{eq}. ΔG^o_{eq} in the d^4 ^{c}**2**-W system is still more exergonic than those of the d^5 systems shown earlier in the Table 2.1.

The next entry in Table 2.3 is the d^3 ^{c}**2**-Ta analogue of ^{c}**2**-W. Both the free metal fragment and the [^{c}**2**-Ta]-N_2 complex have quartet spin ground states lying slightly below a double spin state. The $[^c\mathbf{2}\text{-Ta}]_2(\mu\text{-}N_2)$, on the other hand, has a triplet ground state according to the $(2\pi_\mu)^4(\delta_\mu)^2(3\pi^*_\mu)^0$ d^3-d^3 configuration corresponding to the M≡N-N≡N Lewis structure. As in ^{c}**2**-W, ΔE^v_{eq} and ΔG^o_{eq} are highly negative, -25.5 and -24.0 kcal/mol, respectively. We notice that the ^{c}**2**-W and the ^{c}**2**-Ta ΔE^v_{eq} are nearly equal due to the difference in the occupancy of δ_μ between the systems which does not affect the BO^π_{eq}.

The third case in which maximal ΔBO^π_{eq} is achieved is the d^2 fragments yielding μ-N_2 complexes with the electron configuration: $(2\pi_\mu)^4(\delta_\mu)^0(3\pi^*_\mu)^0$. Complexes of this configuration are experimentally known [28, 29]. In this study, we consider a Nb(III) complex derived from the ^{c}**6**-Nb fragment with a diarylamidodiphosphine pincer ligand previously studied by the Mindiola group [30]. Similar to other systems with ΔBO^{π}_{eq}= 2, the bridging mode of N_2 coordination is computed to be greatly favored over the terminal end-on binding mode. This is shown by very negative ΔE^{v}_{eq}= -35.0 kcal/mol and ΔG^{o}_{eq}= -17.8 kcal/mol.

To further demonstrate how the occupancy of the $2\pi_{\mu}$ and the $3\pi^{*}_{\mu}$ MOs drives the equilibrium in eq1 left or right, we consider a final system of the configuration: $(2\pi_{\mu})^2(\delta_{\mu})^0(3\pi^{*}_{\mu})^0$. The partial depletion of the $2\pi_{\mu}$ orbital in ^{c}**6**-Zr, the d^1-Zr^{III} analogue of ^{c}**6**-Nb, leads to ΔBO^{π}_{eq}= 1. Although bridging is still expected to favored over terminal N_2 coordination, the degree to which it is favored is diminished. This can be seen in the ΔE^{v}_{eq}= -15.5 kcal/mol and ΔG^{o}_{eq}= -6.5 kcal/mol values which are significantly more positive than those of ^{c}**6**-Nb.

The structural parameters displayed in Table 2.4 provide further evidence of the effect of different $2\pi_{\mu}$ and $3\pi^{*}_{\mu}$ populations. The NN bond distance remains almost the same with r_{NN}= 1.122 vs 1.124 Å in the terminal [^{c}**6**-Zr]-N_2 and [^{c}**6**-Nb]-N_2, respectively, despite the different $2\pi_{\mu}$ occupancies. This is due to the absence of NN antibonding character in $2\pi_{\mu}$, leading to little to no effect on the N-N bond. In contrast, the N-N bond is significantly longer in the μ-N_2 ^{c}**6**-Zr complex than in the terminal complex. It is also 0.060 Å longer in the μ-N_2 ^{c}**6**-Nb complex than the ^{c}**6**-Zr analogue (1.177 vs 1.237 Å. In addition, conversion from η-N_2 complexes to μ-N_2 complexes is accompanied with the contraction of the M-N bond by 0.144 Å in ^{c}**6**-Zr and by almost twice as much, 0.294 Å, in the ^{c}**6**-Nb system. This highlights the greater M-N bonding character seen in $2\pi_{\mu}$ than in $2\pi^{nb}_{term}$.

2.2.4 The π-BO Model Beyond the Octahedral Geometries

We now investigate whether the π-BO model extends to non-octahedral complexes. We consider a set of experimentally known four-, three- and two-coordinate fragments presented in Figure 2.11. The results are presented in Table 2.5.

The first non-octahedral system to be considered is the (^{tBu}PNP)ReCl fragment with a d^5-Re^{II} metal center. The d^5-d^5 bridging [(^{tBu}PNP)ReCl]$_2$(μ-N_2) complex was initially synthesized by Schneider's research group and is known to undergo MNNM cleavage at room temperature [31, 32]. No terminal N_2 complex was detected for **7**-Re. The d^5-d^5 electron configuration of the bridging complex is $(2\pi_{\mu})^4(\delta_{\mu})^4(3\pi^{*}_{\mu})^2$, so ΔBO^{π}_{eq} of eq1 becomes 1. In accordance with this configuration, ΔE^{v}_{eq} and ΔG^{o}_{eq} are negative at -10.8 and -6.9 kcal/mol, respectively. On the other hand, terminal bonding was found to be more experimentally favorable in the d^6-Os^{II} analogue of **7**-Re [33]. Our calculations show that the terminal end-on mode of N_2 binding is slightly favored over the bridging one, which can be rationalized by ΔBO^{π}_{eq}=0 due to full $3\pi^{*}_{\mu}$, the antibonding MO, in the μ-N_2 bridged complex (entry **7**-Os in Table 2.5).

The next system we consider is Cummin's complex **8**-Mo, the first complex

Figure 2.6: Fragments investigated for terminal versus bridging N_2 binding in non-octahedral complexes

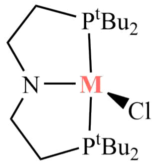

7-Re (d^5); **7**-Os (d^6)

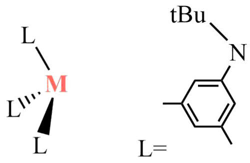

8-Mo (d^3); **8**-Tc (d^4)

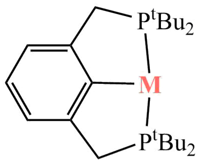

9-Ir (d^8)

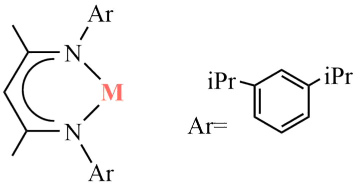

10-Fe (d^7)

ever reported to directly split N_2 into terminal metal nitride complexes [5]. Upon exposure to N_2 at low temperatures, solutions of the three coordinate d^3-Mo^{II} fragment gives the purple bridging N_2 complex which, upon warming the solution, cleaves into metal nitrides. Although it was initially considered as a intermediate, the terminal η-N_2 complex was not detected in solution, indicating the complex's preference for the bridging complex. The computational data for the **8**-Mo supports these experimental findings with ΔG^o_{eq}= -11.6 kcal/mol. The amido ligands in the bridging complex orient themselves such that their p-orbitals can interact with the d_{xy} AO of the metal, giving the Δ_μ MOs antibonding character. The π-electron configuration in this case is $(2\pi_\mu)^4(\delta_\mu)^0(3\pi^*_\mu)^2$ rather than $(2\pi_\mu)^4(\delta_\mu)^2(3\pi^*_\mu)^0$ as seen earlier for [^{c}**2**-Ta]$_2$($\mu$$-$$N_2$) in Table 2.3. Therefore, ΔE^v_{eq} is much *less negative* for **8**-Mo than for ^{c}**2**-Ta (-12.4 vs -25.5 kcal/mol). For cleavage to occur, the two unpaired electrons found in the $3\pi^*_\mu$, will have to be paired in a σ^* orbital for cleavage of the N-N bond to occur since $3\pi^*_\mu$ is bonding in NN [34]. We also consider the d^4-Tc^{III} analogue of **8**-Mo with the following π-electron configuration for the μ-N_2 complex: $(2\pi_\mu)^4(\delta_\mu)^0(3\pi^*_\mu)^4$. In this case both bonding $2\pi_\mu$ and antibonding $3\pi^*_\mu$ are filled, yielding a ΔBO^π= 0 and favoring the η-N_2 complex formation.

The N_2 complexes of the first two complexes considered, **8**-Mo and **8**-Tc, were of four coordinate distorted tetrahedral geometry. A second 4-coordinate geometry to be considered is the square planar N_2 complex of the T-shaped fragment **9**-Ir, the third entry of the Table 2.5. Under N_2 atmosphere (102 torr) the terminal N_2 complex of **9**-Ir equilibrates in a solution of 3% bridging N_2 complex. This indicates slightly endergonic ΔG^o_{eq} [35], which is confirmed computationally (ΔG^o_{eq}= +1.6 kcal/mol). With both $2\pi_\mu$ and $3\pi^*_\mu$ in the μ-

Table 2.5: Terminal versus bridging N_2 binding in five, four and three coordinate complexes.$^{(a)}$

	Cycle 1		Cycle 2				Eq 1			
	ΔE_{dist1}	ΔE_{v1}	ΔE_{dist}	ΔE_{int2}	ΔE_{v2}	d^n-d^n	ΔE^{v}_{eq}	ΔE_{eq}	ΔG^{o}_{eq}	ΔBO^{π}_{eq}
7-Re d^5	5.2	-25.5	9.1	-2.7	-36.2	$(2\pi_\mu)^4(\delta_\mu)^4(3\pi^*_\mu)^2$	-10.8	-9.5	-6.9	1
7-Os d^6	12.3	-33.2	14.2	-7.3	-26.6	$(2\pi_\mu)^4(\delta_\mu)^4(3\pi^*_\mu)^4$	+6.5	+1.2	+3.6	0
8-Mo d^3	20.7 ^{b}	-28.2	20.8 ^{b}	-4.7	-40.6	$(2\pi_\mu)^4(\delta_\mu)^0(3\pi^*_\mu)^2$	-12.4	-17.0	-11.6	1
8-Tc d^4	7.7	-42.6	9.3	-1.3	-38.8	$(2\pi_\mu)^4(\delta_\mu)^0(3\pi^*_\mu)^4$	+3.8	+4.1	+9.1	0
9-Ir d^8	2.2	-31.8	3.1	-3.4	-29.4	$(2\pi_\mu)^4(\delta_\mu)^4(3\pi^*_\mu)^4$	+2.4	-0.1	+1.6	0
10-Fe d^7	--$^{(c)}$	--	--	--	--	$(2\pi_\mu)^4(\delta_\mu)^2(3\pi^*_\mu)^2$	--	-9.3	-10.3	1

$^{(a)}$ M06-L results in kcal/mol. The ΔE terms are defined in Figure 2.6. "d^n-d^n" is the occupancy of the valence MOs in the bridging complex as defined in Figure 2.8. ΔBO^{π}_{eq} is defined in Figure 2.9. $^{(b)}$ ΔE_{dist1} and ΔE_{dist2} account for a change in the spin state from quartet to doublet. $^{(c)}$ Geometries optimized at the B3LYP level. Calculations of the septet state of the [M" M"] adduct for **10**-Fe encountered convergence problems that precluded calculation of ΔE^{v}_{eq}.

N_2 complex filled, ΔE^v_{eq} is positive (+2.4 kcal/mol) and the formation of the terminal N_2 complex is favored over the bridging complex. ΔE_{int2} in this case is -3.4 kcal/mol and is not sufficient enough to offset ΔE^v_{eq} and shift the equilibrium towards the bridging complex as seen in the octahedral d^6 ^{t}**1**-Mo of Table 2.1.

The final system to consider is the high-spin μ-N_2 complex of the iron(I) β-diketiminate fragment **10**-Fe developed by Holland and his group [36, 37, 38]. We calculate the terminal and bridged complexes of **10**-Fe in the quartet and septet states, respectively. The septet state π-electron configuration is $2\pi_\mu)^4(\delta_\mu)^2(3\pi^*_\mu)^2$, so the expected ΔBO^{π}_{eq}= 1. In line with these predictions, ΔG^o_{eq} is exergonic: -10.5 kcal/mol. Single point calculations of the the [Fe"Fe"] adduct encountered convergence failures and precluded the calculation of ΔE^v_{eq}.

2.3 Conclusion and Limitations

The difference between the intrinsic strengths of the terminal and bridging M-N_2 bonds defined by ΔE^v_{eq} varies between +6.5 and -35.0 kcal/mol per M-N bond in a set of transition metal complexes (Table 2.1, 2.3 and 2.5). We attempt to explain this variation by introducing the π-bond order model, a qualitative model applicable to wide range of transition metal complexes with different geometries and electronic structures. In analogy with the allyl group, the BO^π of the terminal MNN moeity is considered constant with a value of 2 regardless of the number of π-electrons supplied by the metal. However, the BO^π in the MNNM unit may vary depending on the occupancy of bonding ($2\pi_\mu$) and antibonding ($3\pi^*_\mu$) π-MOs. Applying these two observation on the equilibrium in eq1 gives an additional variable ΔBO^{π}_{eq} which can be related to ΔE^v_{eq}. When $2\pi_\mu$ and $3\pi^*_\mu$ are both filled, as in the octahedral d^6-d^6 and square-planar d^8-d^8 μ-N_2 complexes, BO^π for the

MNNM core is 2 due to the filled $1\pi_\mu$ MO (which is bonding in NN). ΔBO^π_{eq} in this case is 0 and the equilibrium is expected to shift to the left with positive ΔG^o_{eq}. This is validated computationally where ΔE^v_{eq} for complexes in this category vary between +1.2 and +6.5 kcal/mol. On the other hand, d^5-d^5 and d^1-d^1 complexes have $BO^\pi = 3$ due to partially filled $3\pi^*_\mu$ or partially filled $2\pi_\mu$ and empty $3\pi^*_\mu$, respectively . This gives $\Delta BO^\pi_{eq} = 1$ and favors the formation of the bridging N_2 complex by 2.8 to 12.4 kcal/mol relative to the the terminal N_2 complexes. Lastly, ΔBO^π_{eq} can reach a maximum of two if $2\pi_\mu$ is filled completely and $3\pi^*_\mu$ is empty resulting in a very favored μ-N_2 coordination to the metal centers and very negative ΔE^v_{eq}: -25.5 to -35.0 kcal/mol.

A qualitative π-MO diagram similar to Figure 2.8 was first proposed by Chatt and Roberts to account for observed trends in NN stretching vibrational frequencies (ν_{NN}) when a terminal N_2 complex *trans*-Cl(PMe_2Ph)$_4$Re(N_2) is bridged to other transitional metal fragments with varied d-electron counts [39]. This diagram has been developed in several studies focused on N_2 activation in binding complexes [40, 41, 42]. Such MO diagrams can now explain several structural and electronic parameters such as ν_{NN}, bond lengths, and ΔE^v_{eq}. To our knowledge this is the first time that this concept has been used to understand terminal versus bridging end-on N_2 coordination. Experimentally, crystallographic data helped identify three different Lewis structure for μ-N_2 complexes: M-N≡N-M, M=N=N=M, and M≡N-N≡M. However, when compared, these structures do not represent resonance structures of the same number of bonds. Each structure has a different total number of π-bonds (2,3 and 4, respectively).

As any theoretical model, there are limitations to the proposed model. First, this model doesn't address the variations in the strength of individual bonds (σ and π) but rather focuses on the change in number of π-bonds in eq1. Although this has aided qualitative discussions, the variations in the quality of individual bonds are relevant for quantitative purposes. For example, although d^5 and d^6 MNN complexes both have the same total $BO^\pi = 2$, the vertical dissociation energy of N_2 (-ΔE_{v1}) is systematically greater for d^6 complexes. However, careful inspection of the vertical dissociation energies of N_2 in the μ-N_2 complexes (-ΔE_{v2}) shows no major difference between -ΔE_{v2} for d^5-d^5 and those of d^6-d^6 complexes, although both differ in BO^π. In addition, although the ΔBO^π_{eq} term readily separates the ΔE^v_{eq} values into three non-overlapping sets (slightly positive, modestly negative, and highly negative), the variations within each set are still substantial, reaching near 10 kcal/mol when $\Delta BO^\pi_{eq} = 1$ or 2. This is not out of the ordinary since the complexes differ in metal centers, each having different attributes (effective nuclear charge, electronegativity, oxidation state, and size), and the nature of the ligands. These factors all play important roles in affecting the σ- and the π- components of the coordination energies. Another limitation to the proposed model is that it factors out the spin states and dispersion interactions in ΔE_{dist1}, ΔE_{dist2}, and ΔE_{int2} terms of Figure 2.6. The size of the ligands, for example, can play a significant role in preventing bridging if they were big enough. Even with the mentioned limitations, we believe that this model can aid in first: predicting whether N_2 will bind in a terminal or bridging mode in prospective complexes, and second: choosing suitable metal-ligand pairs for optimal catalytic N_2 fixation and reduction.

The findings and theoretical model presented in this chapter have recently been published (June 28, 2021) in the Journal of The American Chemical Society in collaboration with Patrick L. Holland, Alexander J. M. Miller, and Alan S. Goldman [43].

Chapter 3

Effect of Transition Metal Centers on Bimetallic N_2 Complex Formation and Cleavage

3.1 Background for Present Study

As mentioned in Chapter 2, a plausible method for N_2 cleavage is through the formation of a bimetallic bridged N_2 complex followed by the cleavage of the N-N bond forming two metal nitride complexes. This was first observed by Cummins and Laplaza where a three coordinate Mo (III) complex exposed to 1atm N_2 formed a bridged complex that underwent cleavage into two molybdenum nitrides [5].

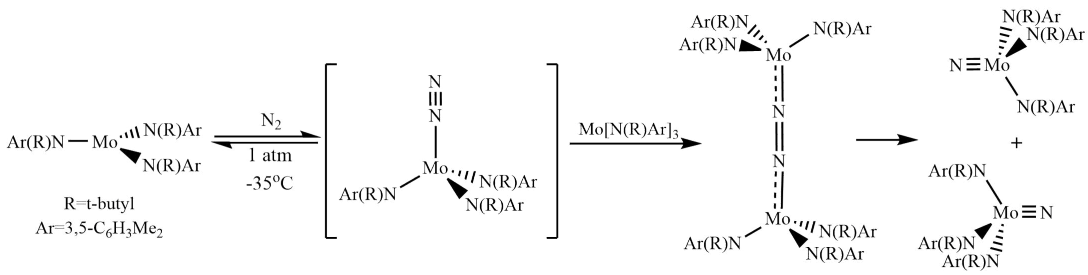

Figure 3.1: The reductive cleavage of N_2 using a Mo(III) complex

Further work conducted by Schrock and his team on pincer ligated metal complexes suggested an alternative mechanism for ammonia synthesis. In this chapter, we focus on the second step of this mechanism involving the cleavage of the bimetallic bridged complex into two metal nitrides. Specifically, we will study the effect of the metal on the formation and cleavage of the bridged N_2 metal complexes.

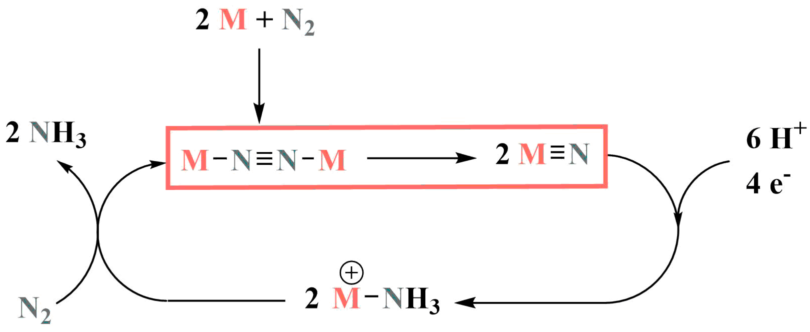

Figure 3.2: Alternative pathway for N_2 reduction to NH_3

We will consider two pincer-ligated systems: the five coordinate N_2 complex of Schneider's complex, $(^{tBu}$PNP)MCl, and the six coordinate N_2 complex of Miller's complex, $(^{iPr}$PONOP)MCl_2. To track the effect of the metal on the formation and cleavage of the bridged N_2 complexes, we examine the Group VII and Group VIII transition metal analogues of these systems.

3.2 Thermodynamics of Equilibrium between Terminal N_2 Complexes and Bridged N_2 Complexes

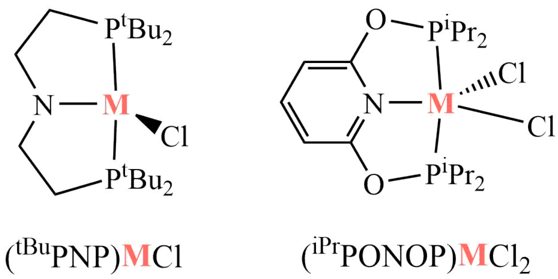

Figure 3.3: Schneider's Complex and Miller's Complex

We begin our investigation by studying the effect of Group VII and Group VIII metal centers on the thermodynamics of the equilibrium considered in eq 1. Calculating the different thermodynamic parameters of eq 1 for the $(^{iPr}$PONOP)MCl_2 complexes yields the results present in the table of Figure 3.3.

We first look at the d^5 Group VII metal complexes with Mn, Tc, and Re metal centers. Consistent with the π-BO model previously proposed, these complexes show negative ΔE^v_{eq} and ΔG^o_{eq} values favoring the formation of the bridging N_2 complex over the terminal N_2 complex. Starting with the left hand side of the

Table 3.1: Terminal versus bridging N_2 binding in Group VII and Group VIII transition metal PONOP complexes $^{(a)}$

	Cycle 1		Cycle 2				Eq 1			
	$\Delta E_{\mathrm{dist1}}$	ΔE_{v1}	$\Delta E_{\mathrm{dist2}}$	ΔE_{int2}	ΔE_{v2}	d^n-d^n	$\Delta E^{\mathrm{v}}_{\mathrm{eq}}$	ΔE_{eq}	$\Delta G^{\circ}_{\mathrm{eq}}$	$\Delta BO^{\pi}_{\mathrm{eq}}$
c2-Mn d^5	6.6	-24.6	10.8	-9.0	-29.5	$(2\pi_\mu)^4(\delta_\mu)^4(3\pi_\mu^*)^2$	-4.8	-9.6	-4.2	1
c2-Tc d^5	7.2	-30.3	9.6	-6.7	-37.2	$(2\pi_\mu)^4(\delta_\mu)^4(3\pi_\mu^*)^2$	-6.9	-11.3	-6.6	1
c2-Re d^5	10.6	-37.2	10.6	-7.2	-42.9	$(2\pi_\mu)^4(\delta_\mu)^4(3\pi_\mu^*)^2$	-5.7	-12.9	-8.0	1
c2-Fe d^6	6.8	-29.3	9.3	-6.3	-29.8	$(2\pi_\mu)^4(\delta_\mu)^4(3\pi_\mu^*)^4$	-0.5	-4.3	-0.3	0
c2-Ru d^6	6.9	-35.1	7.9	-7.0	-33.7	$(2\pi_\mu)^4(\delta_\mu)^4(3\pi_\mu^*)^4$	+1.4	-4.5	-1.1	0
c2-Os d^6	10.9	-43.4	12.3	-8.5	-40.8	$(2\pi_\mu)^4(\delta_\mu)^4(3\pi_\mu^*)^4$	+2.6	-4.6	-0.7	0

[a] M06-L results in kcal/mol. The ΔE terms are defined in Figure 2.6. "d^n-d^n" is the occupancy of the valence MOs in the bridging complex as defined in Figure 2.8. $\Delta BO^{\pi}_{\mathrm{eq}}$ is defined in Figure 2.9.

equilibrium represented by **Cycle 1**, we see no significant effect of the metal on the distortion energies of the metal fragments (ΔE_{dist1}= 6.6 kcal/mol for Mn, 7.2 kcal/mol for Tc, and 10.6 kcal/mol for Re). However, changing the metal has a significant effect on ΔE_{v1} where substituting Mn to Tc leads to a drop from -24.6 kcal/mol to -30.6 kcal/mol. Going further down the group from Tc to Re yields a further drop in ΔE_{v1} by 7 kcal/mol. This indicates much more favorable electronic interactions between complexes with an Re metal center and N_2 than between the later and those with Mn centers. Similarly, in **Cycle 2**, altering the nature of the metal shows almost no effect on the distortion energies (ΔE_{dist2}) and the outersphere interactions between the distorted fragments presented as ΔE_{int2} in Table 3.1. On the other hand, the vertical N_2 binding energy, ΔE_{v2}, is significantly affected by a change in the nature of the metal centers. As we substitute the metal from Mn to Tc to Re vertical binding of N_2 to the [M"M"] adduct becomes more favorable (ΔE_{v2}= -29.5 kcal/mol for Mn, -37.2 kcal/mol for Tc, and -42.9 kcal/mol for Re). The effect of the metal on the vertical binding energies cancels out when computing ΔE^v_{eq} where all ΔE^v_{eq} values for the three metals lie within a range of 2.1 kcal/mol. The ΔE_{v2} values of each metal are more negative than their corresponding ΔE_{v1} values. In addition, the three metals have favorable interaction energies while forming the [M"M"] adduct. These two factors drives the equilibrium towards the right with increasingly negative ΔG^o_{eq} values going down the group (ΔG^o_{eq}= -4.2 kcal/mol for Mn, -6.6 kcal/mol for Tc, and -8.0 kcal/mol for Re).

We extend our study of the effect of the metal center on the equilibrium between terminal N_2 complex formation and bridging N_2 complex formation to Group VIII transition metals. We now consider the Fe, Ru, and Os analogues

Table 3.2: M-N and N-N bond lengths (in Å) and N-N stretching vibration frequencies (in cm^{-1}) for selected octahedral complexes from Figure 3.3[(a)]

		Terminal M-N_2			Bridging M-N_2			Eq 1	
Fragment	dπ/M	r_{MN}	r_{NN}	ν_{NN}	r_{MN}	r_{NN}	ν_{NN}	Δr_{MN}	Δr_{NN}
c2-Mn d^5	**3**	1.892	1.122	2181	1.836	1.160	1909	-0.056	0.038
c2-Tc d^5	**3**	1.975	1.127	2133	1.919	1.164	1885	-0.056	0.037
c2-Re d^5	**3**	1.973	1.131	2093	1.909	1.175	1843	-0.064	0.044
c2-Fe d^6	**4**	1.796	1.123	2186	1.849	1.139	2105	0.053	0.016
c2-Ru d^6	**4**	1.915	1.124	2174	1.952	1.138	2115	0.037	0.014
c2-Os d^6	**4**	1.912	1.130	2142	1.950	1.144	2101	0.015	0.014

(a) Complexes described in Figure 3.3. dπ/M is the number of d electrons provided by each metal to the π-moiety.

of Miller's complex, (^{iPr}PONOP)MCl_2. These complexes have a d^6 π-electron configuration and are expected to favor terminal N_2 complex formation. This is confirmed by the ergoneutral ΔG^o_{eq} values (-0.3 kcal/mol for Fe, -1.1 kcal/mol for Ru, and -0.7 kcal/mol for Os). We notice that the effect of the metal on ΔG^o_{eq} diminishes when moving from Group VII to Group VIII transition metals (range of 0.8 vs 3.8 kcal/mol). To understand the factors affecting this change in trends, we take a closer look at **Cycle 1** and **Cycle 2**. In **Cycle 1**, substituting the metal center from Fe to Ru to Os gives similar trends in distortion energies and vertical N_2 binding energies as seen in Group VII metal complexes. This is consistent with the π-BO model since both have full $2\pi^{nb}_{term}$ MOs. In **Cycle 2**, the distortion energies exhibit no considerable effect of a change in the nature of the metal. On the other hand, we observe a switch in trends in interaction energy, ΔE_{int2}. While Group VII complexes showed less favorable ΔE_{int2} values going down the group, the interaction between the distorted metal fragments becomes more favorable going from Fe (ΔE_{int2}= -6.3 kcal/mol) to Os (ΔE_{int2}= -8.5 kcal/mol). The vertical adiabatic N_2 binding becomes more favorable going down the group, all the while remaining less favored than vertical N_2 binding in the terminal complexes. This yields neutral or positive ΔE^v_{eq} values (-0.5 kcal/mol for Fe, +1.4 kcal/mol for Ru, and +2.6 kcal/mol for Os) meaning that bridging N_2 complex formation is electronically unfavorable.

To study the structural implications of varying the metal centers on the N_2 complex formation we consider the M-N and N-N bond lengths present in Table 3.2. Complexes with Group VII metal centers show the contraction of the M-N bond (negative Δr_{MN} values) and significant elongation of the N-N bond (positive Δr_{NN} values) when going from the the terminal to the bridging N_2 complexes. Going down the group, we observe no considerable effect of varying the metal on the contraction and relaxation of the M-N and N-N bonds, respectively.

Substituting the metal center from Mn to Re leads to an increase contraction by less than 0.01Å in the M-N bond and N-N bond lengthening by an extra 0.006Å only. On the other hand, complexes with d^6 Group VIII metals experience greater structural implications upon changing the metal center. Going down the group from Fe to Ru to Os, we observe that the degree of elongation of the M-N bond is diminished considerably. Δr_{MN} drops from 0.053Å for Fe to 0.037Å for Ru to 0.015Å for Os. The N-N bond is not affected by variations in the metal center where Δr_{NN} remains between 0.016Å and 0.014Å.

Table 3.3: Terminal versus bridging N_2 binding in Group VII and Group VIII transition metal PNP complexes $^{(a)}$

	Cycle 1		**Cycle 2**				**Eq 1**			
	ΔE_{dist1}	ΔE_{v1}	ΔE_{dist2}	ΔE_{int2}	ΔE_{v2}	d^n-d^n	ΔE^v_{eq}	ΔE_{eq}	ΔG°_{eq}	ΔBO^{π}_{eq}
7-Mn d^5	9.9	-30.0	10.7	-9.0	-27.8	$(2\pi_\mu)^4(\delta_\mu)^4(3\pi_\mu^*)^2$	2.2	-6.0	-2.4	1
7-Tc d^5	4.9	-25.3	8.3	-7.9	-28.8	$(2\pi_\mu)^4(\delta_\mu)^4(3\pi_\mu^*)^2$	-3.5	-7.9	-4.6	1
7-Re d^5	5.1	-26.7	9.1	-2.7	-36.9	$(2\pi_\mu)^4(\delta_\mu)^4(3\pi_\mu^*)^2$	-10.2	-9.0	-5.3	1
7-Fe d^6	11.5	-31.0	14.6	-5.8	-28.5	$(2\pi_\mu)^4(\delta_\mu)^4(3\pi_\mu^*)^4$	2.5	-0.2	3.1	0
7-Ru d^6	10.3	-31.1	12.2	-6.4	-25.9	$(2\pi_\mu)^4(\delta_\mu)^4(3\pi_\mu^*)^4$	5.2	0.7	4.0	0
7-Os d^6	12.2	-32.8	14.2	-6.4	-26.9	$(2\pi_\mu)^4(\delta_\mu)^4(3\pi_\mu^*)^4$	6.0	1.6	4.7	0

$^{(a)}$ M06-L results in kcal/mol. The ΔE terms are defined in Figure 2.6. "d^n-d^n" is the occupancy of the valence MOs in the bridging complex as defined in Figure 2.8. ΔBO^{π}_{eq} is defined in Figure 2.9.

The second system we consider is the five coordinate N_2 complex of Schneider's complex, $(^{tBu}PNP)MCl$. Starting with the Group VII metal complexes, we predict the favorable formation of the bridging N_2 complex over the terminal N_2 complex. This is confirmed by the negative ΔG^o_{eq} values ranging from -2.4 kcal/mol for Mn to -5.3 kcal/mol for Re. While the ΔE^v_{eq} values for Tc and Re suggest that electronic factors favor the formation of bridging N_2 complexes with -3.5 and -10.2 kcal/mol, respectively, ΔE^v_{eq} for Mn is calculated to be positive (+2.2 kcal/mol). This is contradictory with the proposed π-BO model which suggests that d^5 systems with partially filled $3\pi^*_\mu$ MOs would electronically favor the formation of the bridging N_2 complexes over terminal complexes. The d^6 Fe analogue shows a similar ΔE^v_{eq} value of 2.5 kcal/mol with a positive ΔG^o_{eq} (+3.1 kcal/mol).

To gain further insight on the factors that may contribute to the unexpected ΔE^v_{eq} of the Mn complex, we compare the electronic structure of the d^5-d^5 Mn bridged N_2 complex presented in Figure 3.4 and 3.5 with that of the d^6-d^6 Fe analogue in Figure 3.6. In addition, the Re centered Schneider complex has a low-lying singlet state that is involved in further cleavage reactions [31]. Here

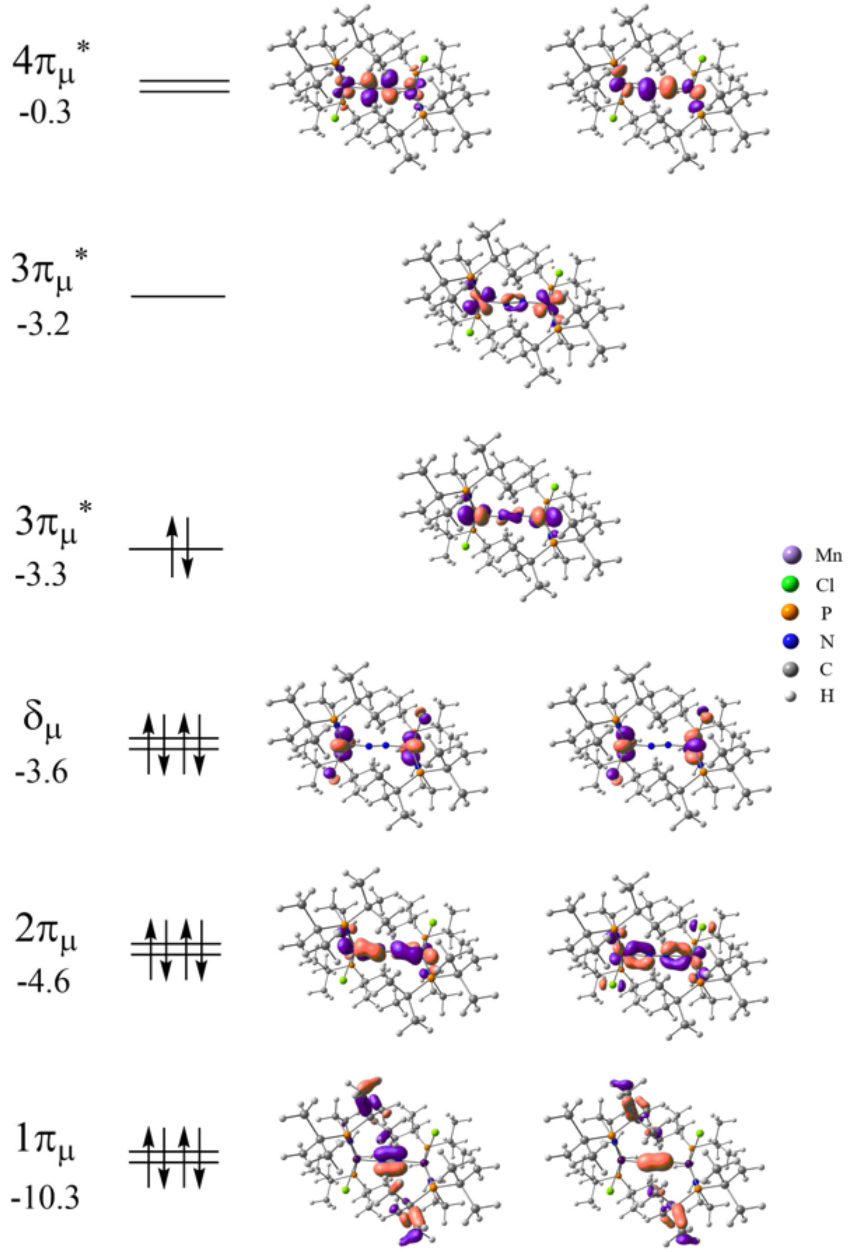

Figure 3.4: Kohn-Sham Molecular Orbitals for the Triplet Bridged N_2 Mn complexes. Orbital energies are given in eV.

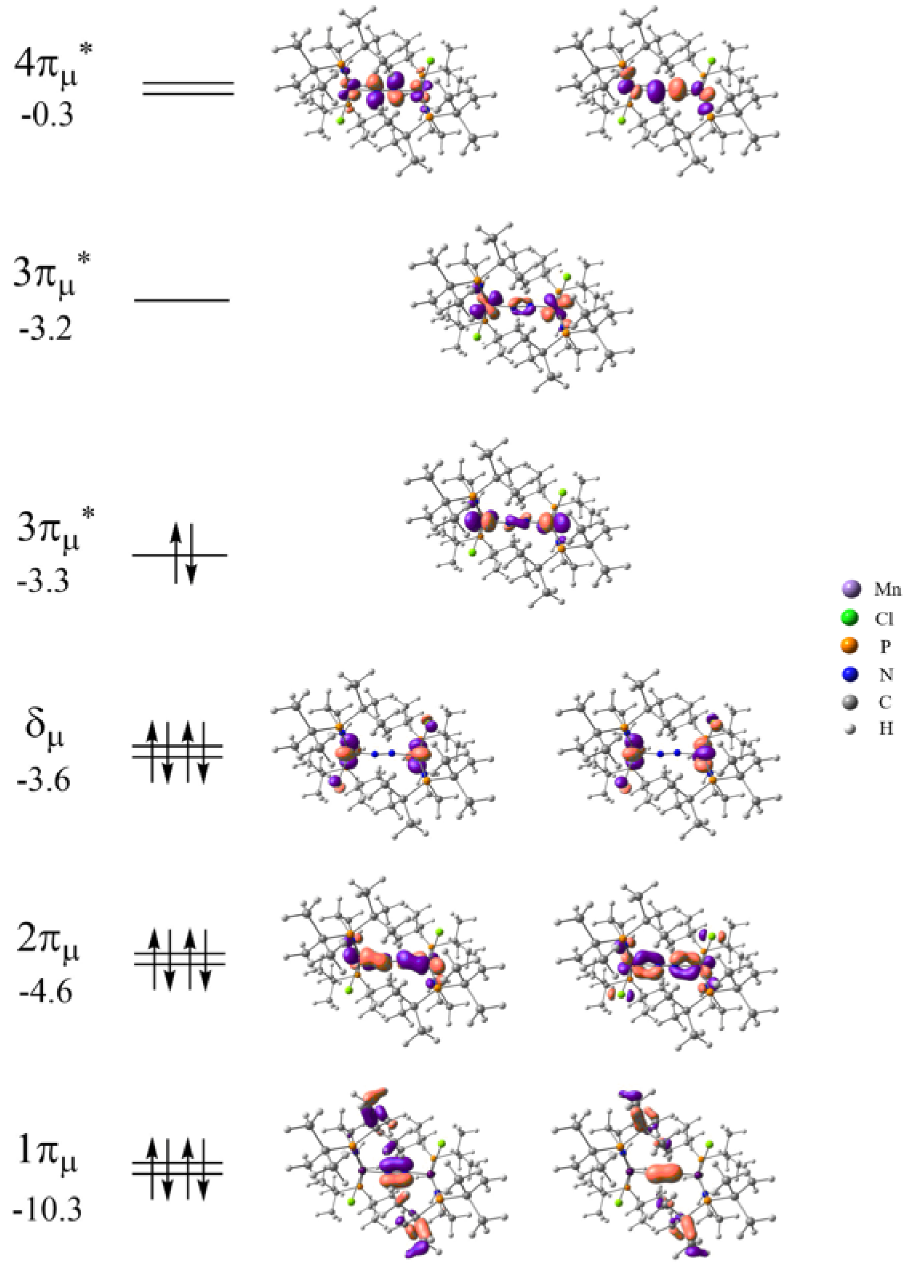

Figure 3.5: Kohn-Sham Molecular Orbitals for the Singlet Bridged N_2 Mn complexes. Orbital energies are given in eV.

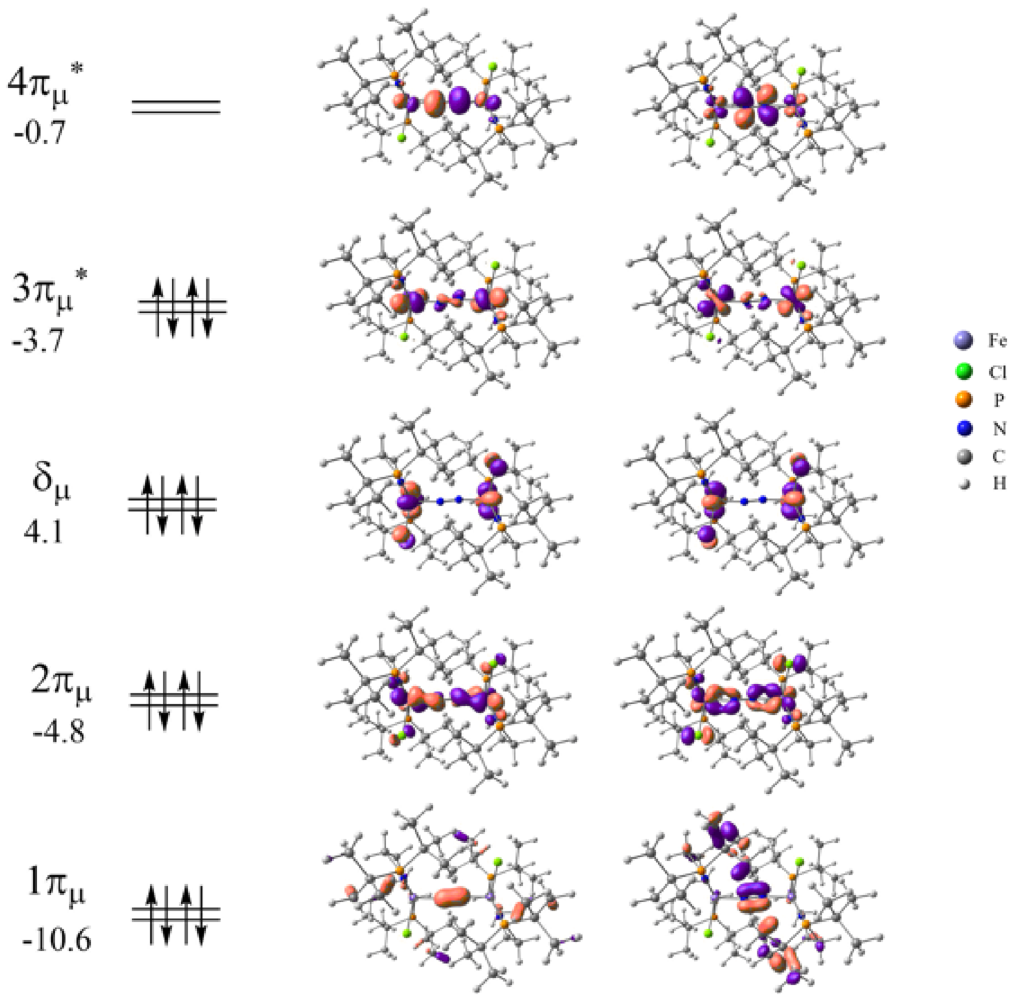

Figure 3.6: Kohn-Sham Molecular Orbitals for the Bridged N_2 Fe complexes. Orbital energies are given in eV.

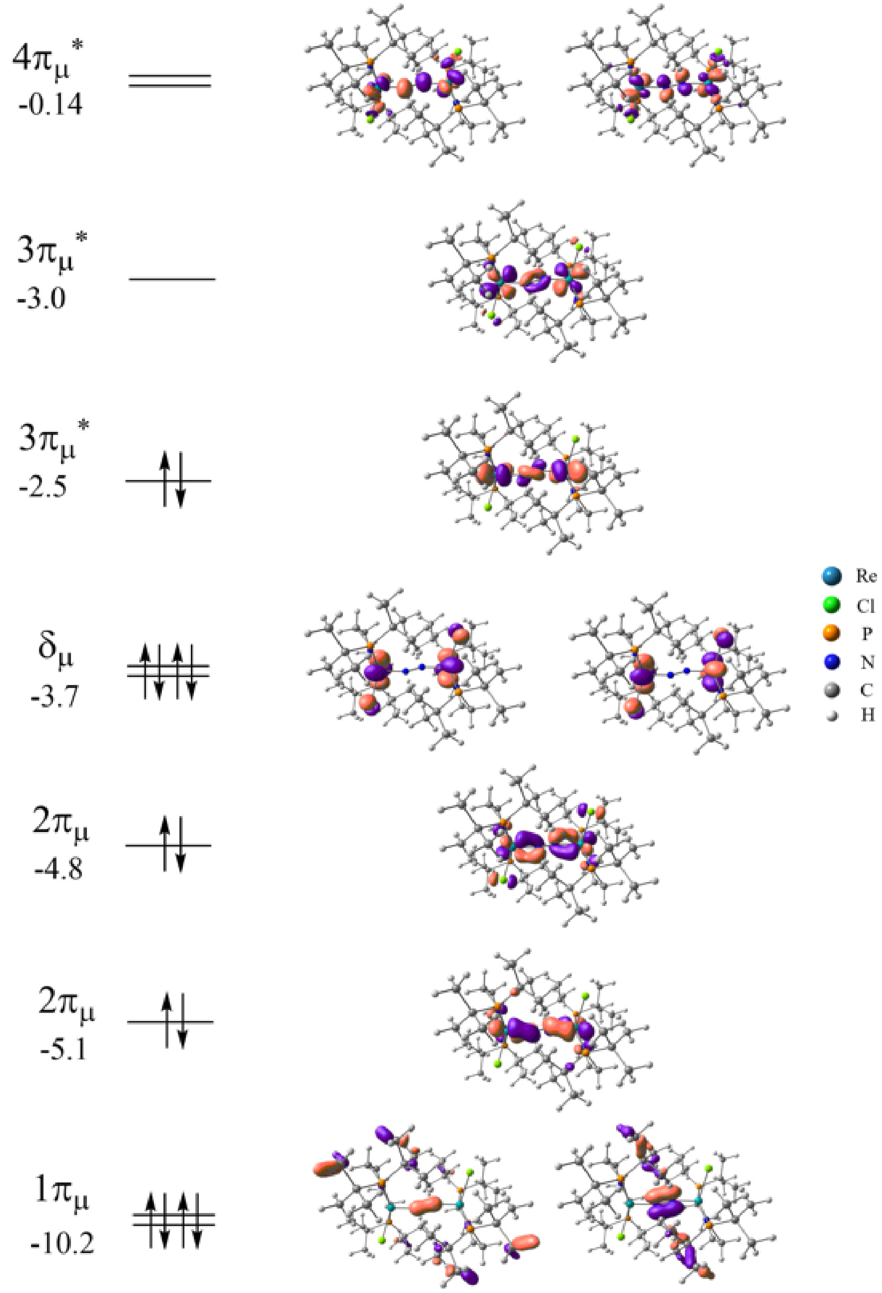

Figure 3.7: Kohn-Sham Molecular Orbitals for the Singlet Bridged N_2 Re complexes. Orbital energies are given in eV.

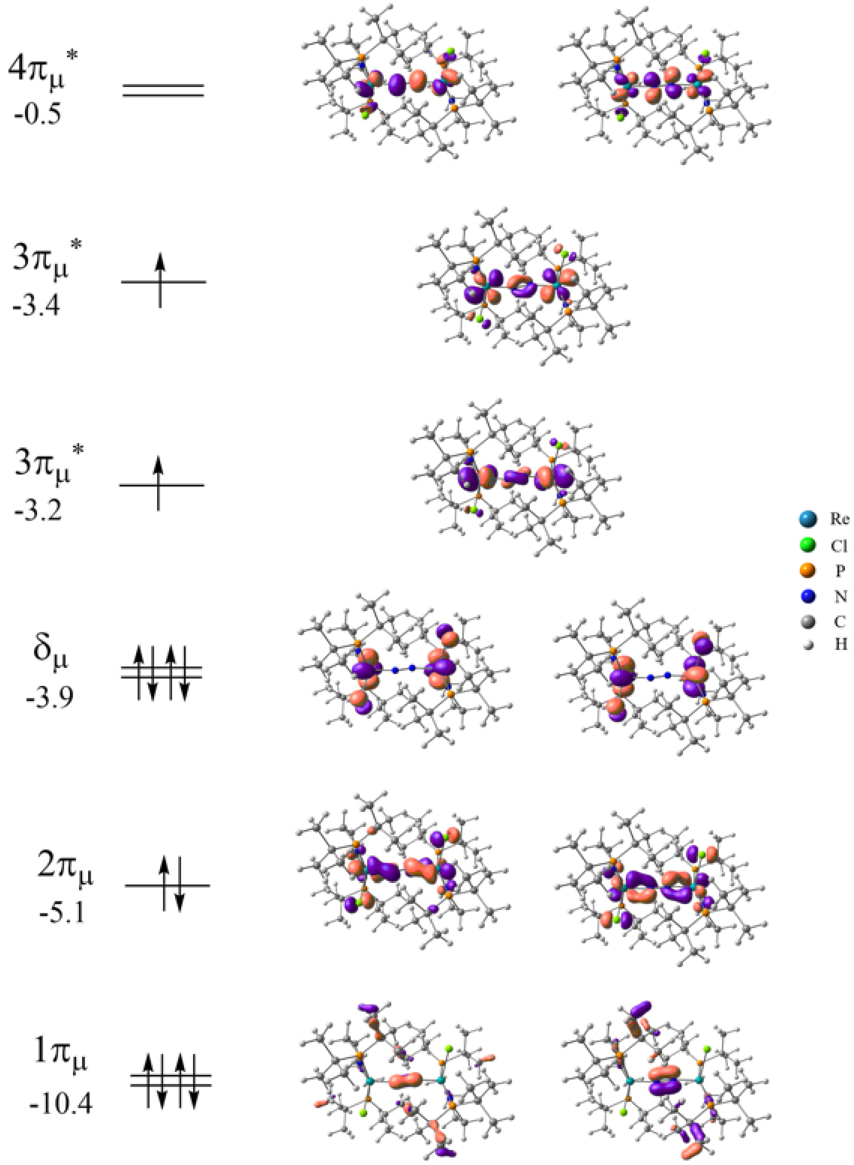

Figure 3.8: Kohn-Sham Molecular Orbitals for the Triplet Bridged N_2 Re complexes. Orbital energies are given in eV.

we present both singlet and triplet state MO energy level diagrams of the Re complex. For the sake of the comparison, we also consider the singlet state of the Mn μ-N_2 complex (Figure 3.5) lying 22 kcal/mol higher in energy than the triplet ground state. Interestingly, this singlet-triplet gap is much larger than those observed for the Re (3 kcal/mol) and the Tc (2 kcal/mol) complexes. We inspect the nature and energy of the Kohn-Sham molecular orbitals, specifically the frontier orbitals, for a possible explanation for the positive ΔE^{v}_{eq} of the Mn N_2 bridged complex. As regularly observed in previous literature, the molecular orbitals show some delocalization beyond the M-NN-M core due to the presence complex pincer ligands and the zig-zag geometry of the M-NN-M core [23, 24]. Consistent with the π-BO model described in Chapter 2, the lowest energy pair of π orbitals shown, $1\pi_\mu$ are bonding in N_2 and around -10 eV in energy. Following $1\pi_\mu$, the $2\pi_\mu$ orbitals, lying between -4.5 and 5.0 eV, show bonding character for the M-N bonds with a nodal plane the 2 central nitrogen atoms. The δ_μ orbitals are higher in energy than $2\pi_\mu$ and are nonbonding in character, consisting of the two metal d_{xy} orbitals facing each other. The $3\pi^*_\mu$ orbitals have two nodal planes, each between a metal center and a nitrogen atom, and show binding character in the N-N bond. While all lower energy orbitals are occupied with 2 electrons each, the occupancy of the higher $3\pi^*_\mu$ orbitals differs between the bridged complexes depending on the metal centers. The singlet state Mn N_2 bridged complex has a Highest Occupied Molecular Orbital (HOMO), $3\pi^*_{\mu-a}$ at -3.3 eV, with 2 paired electrons and a Lowest Unoccupied Molecular Orbital (LUMO), $3\pi^*_{\mu-b}$ at -3.2 eV. The HOMO-LUMO gap in this case is very small at 0.1eV. On the other hand, the triplet gorund state Mn N_2 bridged complex state has two Singly Occupied Molecular Orbitals (SOMO) with one electron each at -4.1 eV, lowering the energy of the whole complex. The d^5-d^5 Re singlet state μ-N_2 complex displays a larger HOMO-LUMO gap (0.5 eV) than its Mn analogue (0.1 eV). The triplet ground state has two SOMOs with a single electron in each. However, the two SOMOs are not degenerate but are 0.2 eV apart. This may be due to the different interaction of each orbital with the pincer ligands. The d^6-d^6 Fe bridged N_2 complex has fully occupied $3\pi^*_\mu$ orbitals, which explains the unfavorable formation of the d^6 bridging N_2 Fe complex. The highest molecular orbital, $4\pi^*_\mu$ at around 0 eV, is antibonding in character and empty for all Re, Mn and Fe complexes. Although the presented π-MO diagrams provide useful insight on the chemistry of N_2 complex formation, their inspection did not provide an adequate explanation for the exceptional ΔE^{v}_{eq} observed for the d^5-Mn system.

We now consider the structural data for the $(^{tBu}$PNP)MCl complexes presented in Figure 3.10 for an explanation of the electronically favored formation of the μ-N_2 Mn-complex. As observed in the PONOP system, the d^6 systems show the lengthening of both the M-N (Δr_{MN} between 0.04 and 0.05Å) and the N-N (Δr_{NN} between 0.015 and 0.018Å) bonds going from the terminal to the bridging complexes. This is consistent with the fully occupied $3\pi^*_\mu$ orbitals with nodal planes between the metal centers and the nitrogen atoms observed in Fig-

Table 3.4: M-N and N-N bond lengths (in Å) and N-N stretching vibration frequencies (in cm^{-1}) for selected octahedral complexes from Table 3.3[a]

		Terminal M-N_2			Bridging M-N_2			Eq 1	
Fragment	dπ/M	r_{MN}	r_{NN}	ν_{NN}	r_{MN}	r_{NN}	ν_{NN}	Δr_{MN}	Δr_{NN}
7-Mn d^5	**3**	1.781	1.139	2066	1.800	1.167	1867	0.019	0.028
7-Tc d^5	**3**	1.943	1.133	2067	1.888	1.174	1809	-0.055	0.041
7-Re d^5	**3**	1.941	1.140	2016	1.885	1.186	1771	-0.056	0.046
7-Fe d^6	**4**	1.766	1.131	2133	1.816	1.146	2058	0.050	0.015
7-Ru d^6	**4**	1.886	1.132	2119	1.932	1.147	2051	0.046	0.015
7-Os d^6	**4**	1.900	1.135	2101	1.940	1.153	2038	0.040	0.018

[a] Complexes described in Figure 3.3. dπ/M is the number of d electrons provided by each metal to the π-moiety.

ures 3.6 and 3.7. While the d^5 Tc and Re systems both show the contraction of the M-N bond when going from the terminal to the bridging complex, the Mn system shows the lengthening of this bond (0.019Å). The weakening of the M-N bond may contribute to the positive ΔE^v_{eq} value, favoring the formation of the η-N_2 complex rather than the μ-N_2 complex.

We return to the study of the effect of the metal in the Schneider PNP system on the equilibrium presented in eq 1 of Chapter 2. Going down the group for the d^5 systems yields more negative ΔE^v_{eq} values (2.2kcal/mol for Mn, -3.5 kcal/mol for Tc, and -10.2 kcal/mol for Re) and ΔG^o_{eq} (-2.4kcal/mol for Mn, -4.6 kcal/mol for Tc, and -5.3 kcal/mol for Re). The observed trend in ΔE^v_{eq} can be attributed to the less favorable ΔE_{v1} values going down the group and more favorable ΔE_{v2} values going down the group. This effect of the metal in diminished ΔG^o_{eq} since its calculation takes the outersphere interactions (ΔE_{int2}) and distortion energies (ΔE_{dist1} and ΔE_{dist2}) into consideration, both of which are less favorable going down the group. As seen in the PONOP systems, the observed effect of the metal on the electronic and free energy is reversed in the d^6 Group VIII metal systems. Less favorable ΔE^v_{eq} values are observed going down the group from Fe (2.5 kcal/mol) to Ru (5.2 kcal/mol) to Os (6.0 kcal/mol). The nature of the metal shows no significant effect on the individual ΔE_{v1} and ΔE_{v2} values, while the ΔE_{v1} values for all three metals remain lower than the ΔE_{v2} values. Similarly, the metal shows no great effect on the outersphere interactions and the distortion energies, where all the individual electronic energies lie within a 2 kcal/mol range.

After studying the thermodynamics of eq 1 for Group VII and Group VIII metal complexes belonging to the PONOP and PNP systems, we can infer that the nature of the metal centers affects the behavior of a system during N_2 complex formation. Some of the factors that come into play are the π-electron count and multiplicity, both of which were covered in this section. We observe that the effect of the metal, whether favorable or unfavorable, is amplified going down the groups. Next we study the effect of the metal on the cleavage of the μ-N_2 complexes upon formation. We will consider both thermodynamics and kinetics of the cleavage reaction.

3.3 Thermodynamics and Kinetics of Cleavage Reaction of Bridged N_2 Complexes

3.3.1 Thermodynamics of Cleavage Reaction of Bridged N_2 Complexes

The second step in Schrock's proposed mechanism for N_2 reduction to NH_3 involves the cleavage of the formed bimetallic bridged complex forming two metal nitrides. We now study the effect of changing the metal centers on this step in two systems: one where this cleavage is thermodynamically favored and the other where photochemical excitation was necessary for cleavage. Upon synthesis by Schneider's group, the μ-N_2-(^{tBu}PNP)ReCl cleaves at room temperature yielding two rhenium nitride complexes [31, 32]. Here we will substitute the Re center with earlier Group VII transition metals: Mn and Tc to study the effect of changing the nature of the metals on the cleavage. On the other hand, the *cis*-isomer of the μ-N_2-(^{iPr}PONOP)$ReCl_2$ complex synthesized by Bruch and Miller cleaved only after photochemical excitation using blue light (405nm) [22]. We will also consider the effect of changing Re to Mn and Tc in this system.

$$\text{MNNM} \xrightarrow{\Delta \text{G}_{cleavage}} 2\ \text{MN} \quad (2)$$

The reaction of interest is represented in Eq 2, where the bimetallic bridged N_2 complex undergoes reductive cleavage to give two identical metal nitrides. We first calculate the free energy of this cleavage reaction for both PNP and PONOP systems with Mn, Tc, and Re metal centers presented in Figure 3.11.

Table 3.5: Thermodynamics of the cleavage of the bimetallic μ-N_2 complexes

	$\Delta G_{\text{cleavage}}$ (kcal/mol)	
M	(^{iPr}PONOP)$\mathbf{M}Cl_2$	(^{tBu}PNP)$\mathbf{M}$Cl
Mn	62.1	27.6
Tc	21.6	-18.8
Re	10.9	-29.0

Consistent with the experimental data, the complexes in the Miller system showed very unfavorable cleavage free energies ($\Delta G_{cleavage} > 0$). Going down the group from Mn to Tc to Re, $\Delta G_{cleavage}$ decreases from 62.1 to 21.6 to 10.9 kcal/mol. The DFT calculations show a dramatic difference between first row transition metal complex and its third row analogue with a difference greater than 50 kcal/mol between the calculated free energies. The Group VII complexes of the Schneider system show a similar trend in $\Delta G_{cleavage}$. While the Re complex exhibits very favored N_2 cleavage (-29.0 kcal/mol), the cleavage reaction becomes less favored going up the group to Tc (-18.8 kcal/mol) and Mn (27.6 kcal/mol). A dramatic jump in energy is also observed in the Mn complex making the cleavage reaction thermodynamically not possible for the Mn μ-N_2 complex. The big difference in energy between the Mn and Re complexes in both PNP and PONOP systems led us to propose that there is a fundamental difference in the electronic structure of these complexes. A quick literature search on first row transition metal complexes showed that such complexes may prefer to occupy high-spin states when in trigonal bipyramidal (TBP), square pyramidal, or octahedral geometries [44, 45, 46]. The Manganese terminal and bridged N_2 complexes of Schneider's complex take on a distorted TBP coordination geometry and square pyramidal geometry around the metal centers, respectively, while those of Miller's complex are of a distorted octahedral geometry.

When surrounded by strong field ligands, which interact very well with the metal center, the metal center exhibits a low-spin state. However, when surrounded by weak field ligands, which have weaker interactions with the metal, the metal center exhibits a high-spin state. The d-orbital electronic structure of the high- and low-spin states are presented in Figure 3.9. The metal d-orbitals in TBP complexes split into a pair of degenerate orbitals with e" symmetry, a pair of degenerate orbitals with e' symmetry, and an $a_1^{"*}$ orbital. The e" orbitals are fully occupied in the low-spin state and a single electron occupies the e' orbital. In the high-spin state, a single electron occupies each orbital. In the octahedral systems, the metal d-orbitals split into three degenerate t_{2g} orbitals and two $e_g^{'}$ orbitals. While the five electrons occupy the t_{2g} orbitals in low-spin states, the electrons are distributed between the t_{2g} and $e_g^{'}$ orbitals in the octahedral high-spin states where each electron occupies an orbital. For square pyramidal systems. the metal d-orbitals split into 2 degenerate orbitals of e symmetry and three orbitals of b_2, a_1, and b_1 symmetry. The low-spin state has fully occupied e orbitals with one electron in the b_2 orbital. On the other hand, the high-spin state has a single electron in every orbital. Second and third row d^5 transition metal complexes do not exhibit the same behavior regarding spin states due to their larger 4d and 5d orbitals. Since the 4d and 5d orbitals are significantly larger than the 3d orbital, they have greater overlap with ligand orbitals than the later, allowing more interaction with them [47]. In addition, the larger space available for the electrons in these larger orbitals allows for lower electron pairing energy, a factor that affects the spin state along with the coulombic energy of repulsion and the split between orbitals (t_{2g}-$e_g^{'}$ split for octahedral complexes also

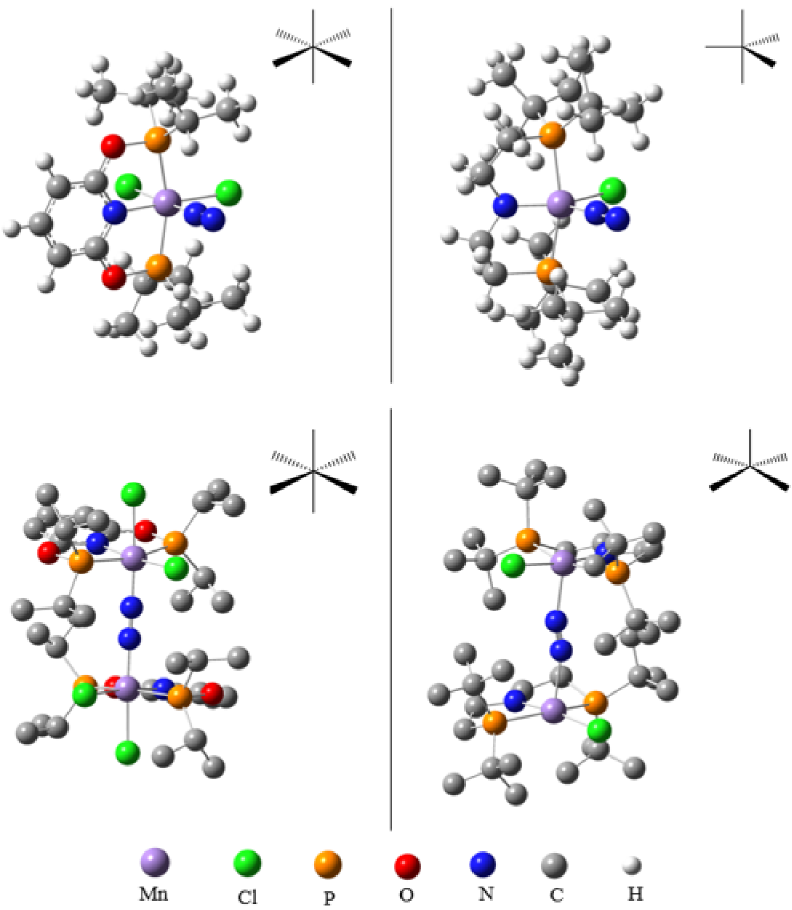

Figure 3.9: Terminal and Bridged N_2 complexes for Miller's (left) and Schneider's (right) complexes

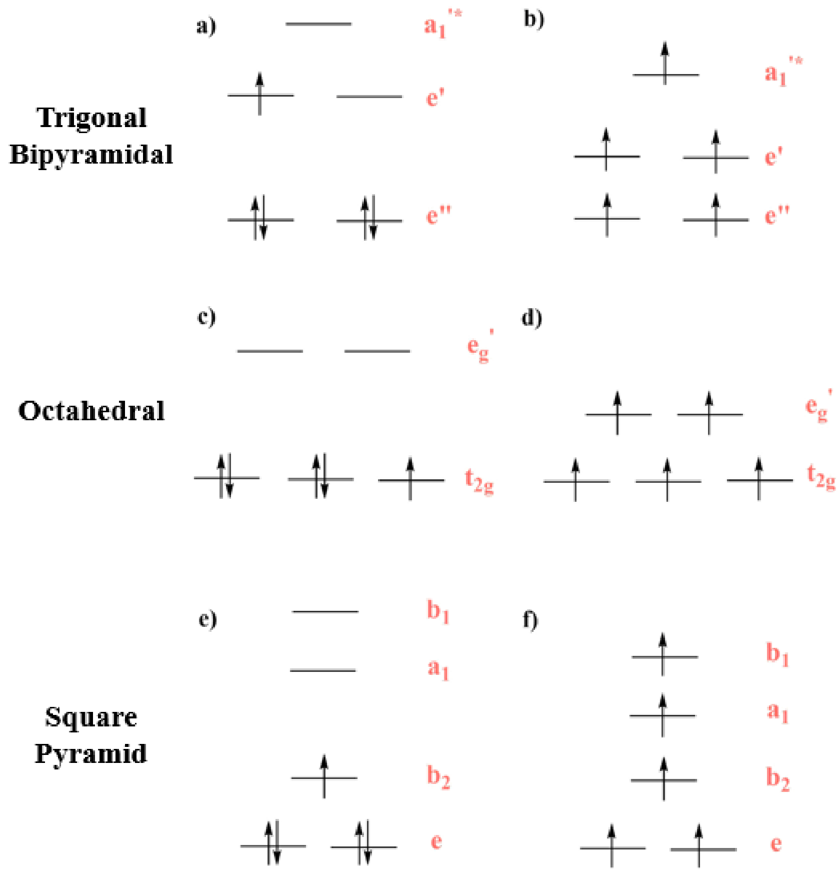

Figure 3.10: Energy level diagram for a) low-spin and b) high-spin states of trigonal bipyramidal complexes, c) low-spin and d) high-spin state of octahedral complexes, and e) low-spin and f) high-spin state of square pyramid complexes

known as Δ_o).

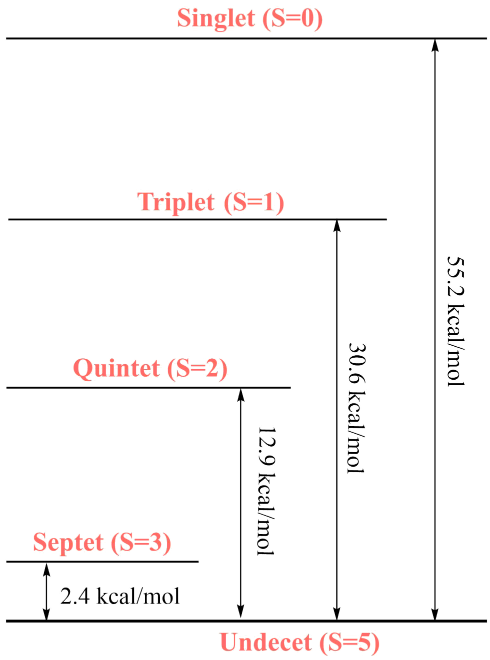

Figure 3.11: Higher spin states and relative energies of the μ-N_2-(^{tBu}PNP)MnCl complex. The nonet spin state did not stay intact upon optimization and was not included in the diagram.

Since the bridged Mn N_2 complex has a total of 10 metal d-electrons, there are a total of six possible spin states. If all the d-electrons are paired, the spin state is a singlet (S=0). If two electrons are unpaired, it becomes a triplet (S=1). The bridged complex will exhibit a quintet spin (S=2) if four electrons are unpaired, a septet (S=3) if 6 electrons are unpaired, a nonet (S=4) if 8 electrons are unpaired, and an undecet (S=5) if all ten electrons are unpaired. The geometries of the higher spin states of the Mn analogue of the Schneider complex were optimized and their energies relative to the determined ground state are given in Figure 3.10. The undecet has the lowest electronic energy among the higher spin states so it is considered the ground state of the μ-N_2-(^{tBu}PNP)MnCl complex. Upon optimization, the nonet state did not remain intact and was, therefore, not included in the diagram. The singlet state was highest in energy. As the multiplicity of the complex increases, its energy decreases. However the energy gap between higher spin states becomes smaller as we approach the ground state.

Now that we have determined the ground state of the Mn N_2 bridged complex, we can perform the calculation for the cleavage reaction. The energies corresponding to the (^{tBu}PNP)MCl systems are presented in the table of Table 3.5. After correcting the ground state energy of the Mn complex, $\Delta G_{cleavage}$ of its corresponding μ-N_2 complex increases to 78.8 kcal/mol. This shows that upon

Table 3.6: Thermodynamics of the cleavage of the bimetallic μ-N_2 complexes

	$\Delta G_{cleavage}$ (kcal/mol)
M	(^{tBu}PNP)**M**Cl
Mn	78.8
Tc	-18.8
Re	-29.0

formation, the bridged Mn N_2 complex will not favor cleavage.

3.3.2 Kinetics of Cleavage Reaction of Bridged N_2 Complexes

In this section, we will focus our study the kinetics of the cleavage reaction for the Schneider system. The μ-N_2-(^{tBu}PNP)ReCl complex was observed to undergo thermodynamically favored reductive cleavage experimentally. Although, the bridged N_2 Re complex has a triplet ground state, Schneider's group could locate a transition state on the singlet potential energy surface (PES). Here, we reproduce these experimental results computationally and extend our study to discuss the effect of changing the metal center on the kinetics of the reaction. We perform our optimization in gas phase, then run a single point calculation Toluene as a solvent using the M06L level of theory.

The activation energy, $\Delta G^{\ddagger}_{M06L}$, for the cleavage of the Re μ-N_2 complex is 19.7 kcal/mol. The activated transition state (TS) exhibits in-plane zig-zag vibrations with a N-N bond distance of 1.58 Å. This is consistent with the computational results obtained by Schneider and his group with $\Delta G^{\ddagger}_{exp}$ = 19.8 kcal/mol [32]. The N-N bond distance increases along the course of the reaction, starting with 1.19 Å in the reactant to 1.58 Å in the TS to 3.8 Å in the cleaved product. We then extend our study to the Mn and Tc analogues of the bridging N_2 complex. Starting with the Tc complex, $\Delta G^{\ddagger}_{M06L}$ of the N_2 splitting reaction was 23.1 kcal/mol. Similar to its Rhenium analogue, the TS showed in-plane zig-zag vibrations with an N-N bond distance of 1.58 Å. Throughout the course of the reaction the N-N bond distance increases from 1.18 Å in the reactant to 1.58 Å in the TS to 3.21 Å in the product. The overall reaction appears to be less thermodynamically favored than the that for the Re system, with a ΔG_{M06L} = -19.3 kcal/mol for Mn vs -26.4 kcal/mol for Re. In fact, the synthesis of a couple of N_2 Tc-PNP complexes has recently been reported by the Schneider group [48]. Following similar experimental procedures for the Tc as for the previous Re systems yielded different results. Upon the reduction of (^{tBu}PNP)$TcCl_2$ with [Co(Cp*)$_2$] under a flow of N_2, a terminal N_2 complex was formed. However, the reduction of a (^{tBu}PNP)$TcCl_3$ with [Co(Cp*)$_2$] under a flow of N_2 resulted in the formation of a bridged N_2 complex shown in Figure 3.13. This N_2 complex

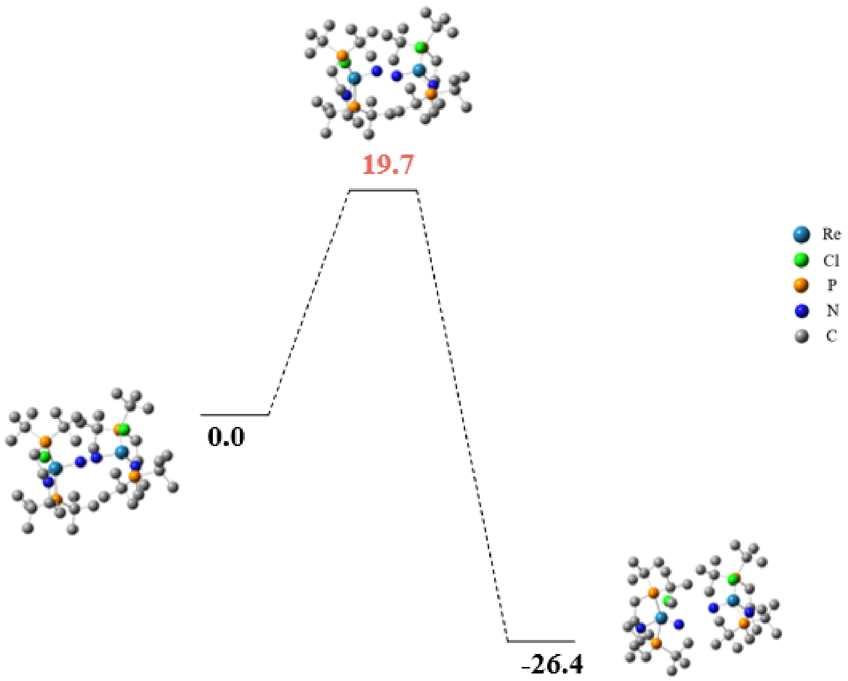

Figure 3.12: PES for the cleavage of the μ-N_2-(^{tBu}PNP)ReCl complex. Energies are given in kcal/mol.

did not cleave thermodynamically but remained intact. The computations performed here correspond to a different complex which the group was not able to synthesize. Although our results have no experimental data yet, they may aid in explaining the factors that favor N_2 dissociation.

The final reaction we consider is the cleavage of the Mn μ-N_2 complex. The PES shown in Figure 3.19 displays a positive ΔG_{M06L}, 10.0 kcal/mol, for the cleavage reaction. It also shows a much higher $\Delta G^{\ddagger}_{M06L}$ = 39.3 kcal/mol, which is almost double those of the Re and Tc systems. The TS shows similar in-plane zig-zag vibrations to those of the previously considered systems, but a considerably larger N-N bond distance (1.66 Å). Throughout the course of the reaction the N-N bond distance increases from 1.16 Å in the reactant to 1.66 Å in the TS to 2.90 Å in the product. The μ-N_2-(^{tBu}PNP)MnCl complex has not been synthesized experimentally. However, comparing its computational results to those of the Re and Tc systems shows that the cleavage reaction of the μ-N_2-(^{tBu}PNP)MnCl complex is unlikely both thermodynamically and kinetically. Since we are considering the singlet-state surfaces for these reactions and the ground state for the Mn μ-N_2 complex is an undecet, then the reactant in this case is an excited state. It is expected to be more reactive than the ground state but shows a very high activation energy. Based on these observations and those shown earlier in this chapter, it is not recommended to use Mn pincer ligated complexes for N_2 activation and cleavage via the formation of a bridging

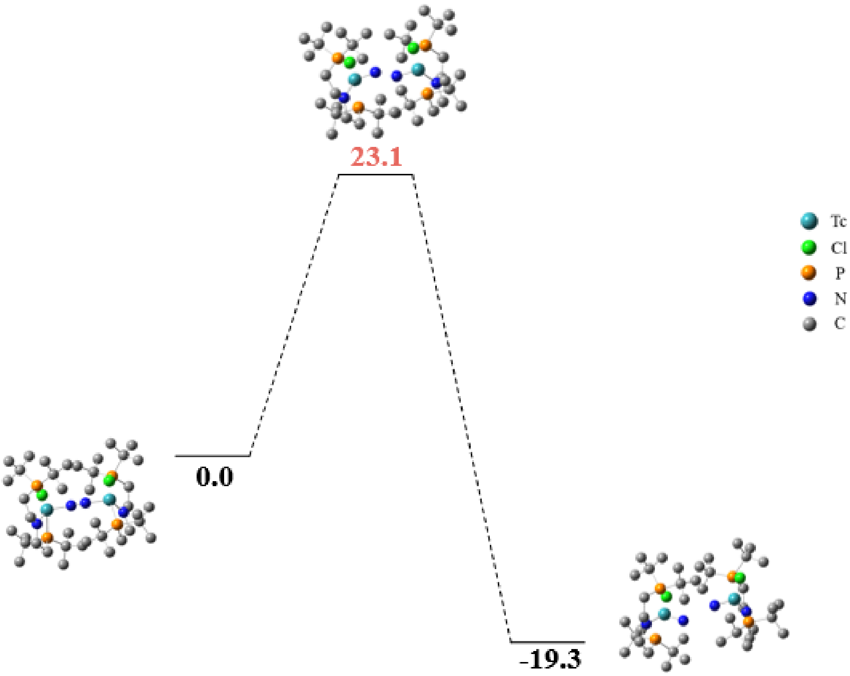

Figure 3.13: PES for the cleavage of the μ-N_2-(^{tBu}PNP)TcCl complex. Energies are given in kcal/mol.

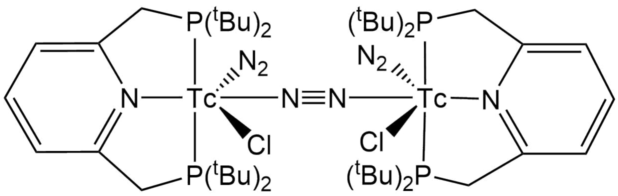

Figure 3.14: [Tc(^{tBu}PNP)Cl(N_2)]$_2$(μ-N_2) complex synthesized by Schneider and his group

complex.

3.3.3 Concluding Remarks

In this section, we explored the effect of the nature of the metal and coordination sphere on the cleavage of bimetallic bridged N_2 complexes. The computed free energies of this reaction showed significant effects of both the metal center and the coordination sphere. The effect of the coordination sphere was observed when systems having the same metal centers showed opposite results upon changing the coordination number and the nature of the ligands. The effect of the metal was also clear upon, within the same system, changing the metal center from the first row Mn to the second row Tc and third row Re, the free energy of the

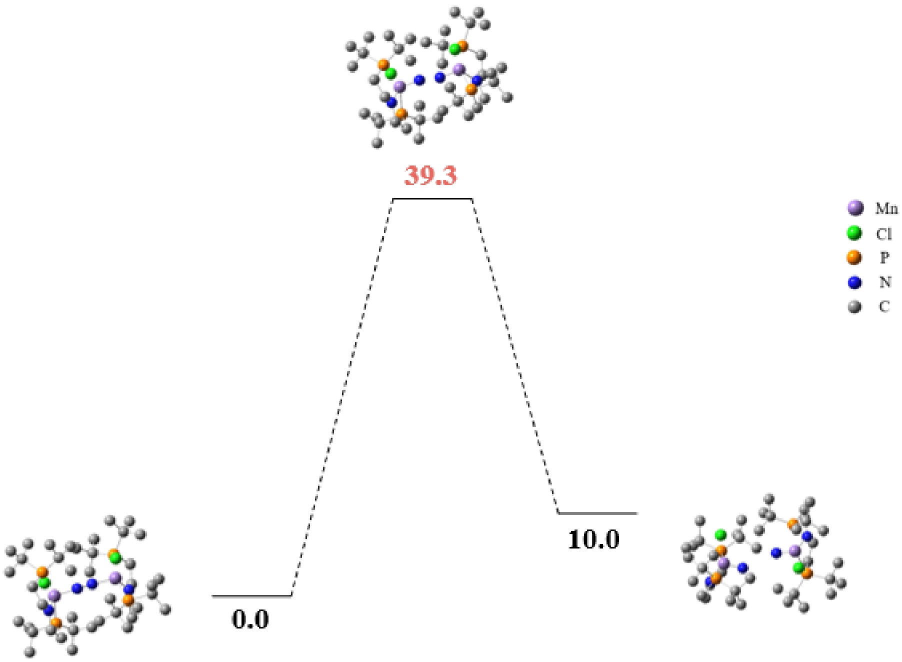

Figure 3.15: PES for the cleavage of the μ-N_2-(^{tBu}PNP)MnCl complex. Energies are given in kcal/mol.

reaction decreased dramatically. A deeper study of the different spin states of the Mn systems showed that this first row metal prefers to exhibit higher open shell spin states which effects the overall behavior of the metal complex. The kinetics of the cleavage reactions were also greatly affected by changing the nature of the metal center, where the activation energy of the Mn system was almost double that calculated for the Tc and Re systems. From both the thermodynamic and the kinetic studies presented here, we can infer that Re bimetallic bridged N_2 complexes have a much greater propensity to cleave than Tc complexes, while Mn complexes highly disfavor cleavage.

Chapter 4

Reactions of Metal Nitride Complexes

As seen in the Chatt cycle and the alternative mechanism suggested by Schrock, both terminal and bridged pathways lead to the formation of metal nitride complexes. To obtain the final product of interest, say ammonia, the metal-nitride intermediate must undergo further reaction such as proton-coupled electron transfers (PCET). However, the M≡N triple bond is in turn a strong bond, and despite its formal classification as nitride, the M≡N bond has highly covalent character, and therefore poses a challenge in mediating further reactions. Because of the limited experimental data associated with the poor reactivity, quantum chemical methods can be of great value in providing systematic understanding of the reactivity of metal-nitride bonds. Herein, we conduct a systematic study on how the identity of the metal and the coordination sphere affects the affinity of the nitrogen center of the metal nitride bond to different addenda. We start with the hydrogen atom transfer (HAT) reaction. This reaction can be divided into two consecutive steps: electron addition and proton addition, as shown in Figure 4.1. This scheme can be extended to handle the second and third hydrogen atom transfer, yielding ammonia. To translate the computed proton and electron affinities to electrochemical parameters, the thermodynamic cycle is coupled with isodesmic reactions using reference systems with available Redox and pKa data to determine the reduction potential (E^o), the acid dissociation constant (pKa) and the bond dissociation free energy (BDFE). This DFT-based isodesmic treatment will be explained more thoroughly in the following section. In addition to hydrogen atom addition, we are interested in determining the energy of nitrogen atom and oxygen atom transfer ($\Delta G_{transfer}$) to the M≡N bond presented in equation 1. The nitrogen atom transfer reaction is directly relevant to the splitting of bridged dinitrogen mentioned in previous chapters.

$$2\mathrm{MN} + \mathrm{X}_2 \xrightarrow{\Delta \mathrm{G}_{transfer}} 2\ \mathrm{MNX} \quad (1)$$

4.1 Proton-Coupled Electron Transfer

4.1.1 Background

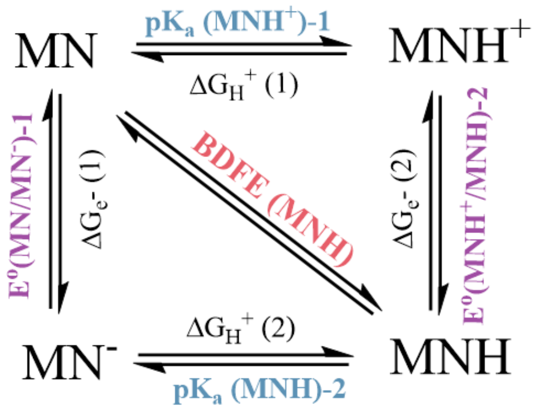

Figure 4.1: Proton Coupled Electron Transfer Reactions

Proton-coupled electron transfer reactions are observed in many biological and catalytic systems. While the definition of PCET reactions remains broad, we can simply define them as proton and electron transfers that may occur simultaneously or consecutively. The protons and electrons may originate from the same reactant and be transferred to a single compound, or may have different sources and recipients. In organometallic systems, such reactions may involve inner-sphere or outer-sphere interactions. Here we focus on a specific class of PCET reactions: Hydrogen Atom Transfers (HAT). HAT reactions (eq 2) involve the transfer of a single electron and a single proton along a common path [49].

$$\text{X}-\text{H} + \text{Y} \longrightarrow \text{X} + \text{Y-H} \quad (2)$$

One of the steps in the alternative mechanism suggested by Schrock for ammonia synthesis via the formation and cleavage of bridged bimetallic complexes involves a series of PCET reactions to the formed metal nitride complexes.

Here we will consider a DFT-based isodesmic approach to study the effect of the metal and coordination sphere on the first HAT to the metal nitride [50]. The isodesmic treatment will give relative free energies between our system and a reference one. Usually in such treatments, references are chosen to be similar to the system under study and have previous experimental data. The reference systems used here are: pyridine for the proton transfers, $ReCl_3$ for the electron transfer, and (2,2,6,6-Tetramethylpiperidin-1-yl)oxyl (TEMPO) for the bond dissociation free energy calculations. The calculated free energies of our system is related to the reference system and measurable properties through equations 3, 4 and 5.

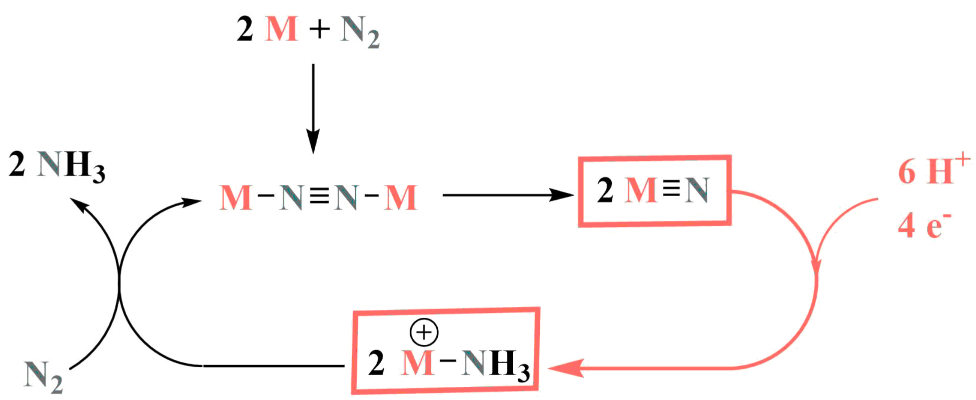

Figure 4.2: Schrock's Mechanism for Ammonia Synthesis

For the electron transfer reaction, the measurable property in the redox potential (E^o) shown in equation 3, where E^o_{ref} is the experimental redox potential of $ReCl_3$ and $\Delta\Delta G_{e^-}$ is the difference between the free energy of the electron transfer reaction to $ReCl_3$ and the free energy of the electron transfer to our complex determined computationally. For the proton transfer step, the acid dissociation

$$E^o = E^{\circ}_{ref} - \frac{\Delta\Delta G_{e^-}}{23.06} \qquad (3)$$

$$pK_a = pK_a^{ref} - \frac{\Delta\Delta G_{H^+}}{1.37} \qquad (4)$$

$$BDFE = 23.06\,E^o + 1.37\,pK_a + 66 \qquad (5)$$

constant (pKa) is the experimentally measurable property. It is shown in eq 4, where pKa^{ref} is the experimental acid dissociation constant of pyridine and $\Delta\Delta G_{H^+}$ is the difference between the free energy of the proton transfer reaction to pyridine and the free energy of the proton transfer to our complex determined computationally. The bond dissociation free energy (BDFE) for the hydrogen atom is determined from both E^o and pKa values and the experimental BDFE of hydrogen bond to TEMPO (in this case it is 66 kcal/mol).

4.1.2 Effect of Metal & Coordination Sphere on PCET Reactions

To study the effect of the coordination sphere on PCET reactions of metal nitrides, we will consider the two systems previously considered in Chapter 3: the five coordinate nitride complex of Schneider's complex, $(^{tBu}PNP)MCl$, and the six coordinate nitride complex of Miller's complex, (^{iPr}PONOP)MCl_2. To track the effect of the metal on the formation and cleavage of the bridged N_2 complexes, we examine the Group VII transition metal analogues of these systems. We will vary the metal center in each of those systems between three Group VII metals: Mn, Tc, and Re. The results of the first proton-coupled electron transfer to the Schneider system are presented in Table 4.1.

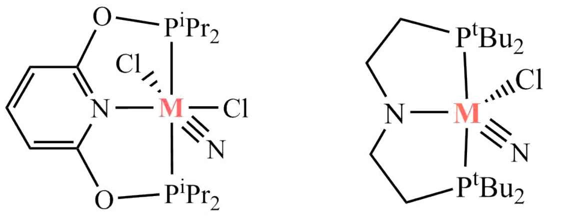

(^{iPr}PONOP)$MNCl_2$ (^{tBu}PNP)MNCl

Figure 4.3: Metal Nitrides of Miller's Complex (left) and Schneider's Complex (right)

Table 4.1: PCET Data for the first hydrogen atom transfer to Schnieder's complex $^{(a)}$

	Pathway -1-		Pathway -2-		
	ΔG_{H+} (1)	ΔG_{e^-} (2)	ΔG_{e^-} (1)	ΔG_{H+} (2)	**BDFE**
Mn	-141	-89	-47	-183	52
Tc	-142	-76	-28	-192	42
Re	-148	-71	-25	-195	41

(a) Free energies and bond dissociation free energies are given in kcal/mol.

There are two possible pathways for a hydrogen atom transfer to occur: the first involves a proton transfer followed by an electron transfer, while the second involves an electron transfer followed by a proton transfer. Considering the first pathway, Pathway -1-, substituting the metal from Mn to Tc to Re leads to a decrease in $\Delta G_{H+}(1)$ from -141 kcal/mol to -148 kcal/mol. This means that the first proton transfer becomes more favorable going down Group VII. Following this proton transfer, the electron transfer becomes less favored going down the group, where $\Delta G_{e^-}(2)$ increases from -89 kcal/mol to -71 kcal/mol. Pathway -2- starts with an electron transfer to the metal nitride, which is less favorable going down Group VII (-47 kcal/mol for Mn vs -25 kcal/mol for Re). Similar to Pathway -1-, the proton transfer is more favorable going from Mn (-183 kcal/mol) to Re (-195 kcal/mol). In both pathways, the electron transfer reactions become significantly more favorable going down the group where the average difference in energy between the Mn systems and the Re systems is 20 kcal/mol. The effect of changing the metal on the proton addition in both pathways is less dramatic where the average difference between the Mn complexes and the Re complexes is 10 kcal/mol. While the trends in the proton addition reactions can be attributed to the difference in size and electronegativity of the metals, the electron transfer reactions may be influenced by other structural or electronic factors. The structural data for the metal nitrides and the products of the electron and proton transfers are presented in Table 4.2.

Table 4.2: Structural data for the proton, electron, and hydrogen atom transfer to Schneider's complex $^{(a)}$

	MN	MN$^-$	MNH$^+$		MNH	
	M–N	M-N	M-N	N-H	M-N	N-H
Mn	1.52	1.53	1.59	1.02	1.66	1.03
Tc	1.62	1.72	1.70	1.02	1.76	1.03
Re	1.66	1.74	1.72	1.02	1.78	1.02

(a) Bond distances are given in Å.

Upon the addition of an electron to the manganese metal nitride, the M-N bond distance stays the same (around 1.52 Å). On the other hand, the addition of an electron to the technetium and rhenium metal nitrides leads to a significant increase in M-N bond distance from 1.62 Å to 1.72 Å for Tc and 1.66 Å to 1.74 Å for Re. The addition of a proton to the negatively charged anion radical leads to the further stretching of metal nitride bond in all three metal systems. The addition of a proton to the metal nitrides of Schneider's system leads to the slight stretching of the metal nitride bond. The calculation of the bond dissociation free energy for the hydrogen atom using from eq 5 yields the following dissociation energies: 52 kcal/mol for Mn, 42 kcal/mol for Tc, and 41 kcal/mol for Re. More energy is required to break the formed N-H bond in the Mn system than in the Re and Tc system. Simply put, this means that this bond is stronger in the Mn Schneider system than in the Tc and Re Schneider system.

To check whether the observed effect of the metal on the PCET reactions of metal nitrides is carried over to systems of different coordination spheres, we consider a second system. This second system is the six coordinate metal nitride complex of the Miller system. Similar to the previous system, ΔG_{H^+} (1) decreases going down group VII from Mn (-125 kcal/mol) to Re (-138 kcal/mol). The following electron transfer is less favored going down the group (ΔG_{e^-}(2) is -122 kcal/mol for Mn to -86 kcal/mol for Re). In Pathway -2-, the first electron

Table 4.3: PCET Data for the first hydrogen atom transfer to Miller's complex $^{(a)}$

	Pathway -1-		Pathway -2-		
	ΔG_{H+} (1)	ΔG_{e}- (2)	ΔG_{e}- (1)	ΔG_{H+} (2)	BDFE
Mn	-125	-122	-61	-186	45
Tc	-129	-97	-51	-175	48
Re	-138	-86	-50	-174	69

(a) Free energies and bond dissociation free energies are given in kcal/mol.

Table 4.4: Structural data for the proton, electron, and hydrogen atom transfer to Miller's complex $^{(a)}$

	MN	MN^-	MNH^+		MNH	
	M–N	M-N	M-N	N-H	M-N	N-H
Mn	1.51	1.54	1.58	1.02	1.70	1.03
Tc	1.62	1.65	1.69	1.02	1.78	1.03
Re	1.66	1.69	1.71	1.02	1.79	1.02

(a) Bond distances are given in Å.

transfer is also less favorable going down the group ($\Delta G_{e^-}(1)$ is -61 kcal/mol for Mn and -50 kcal/mol for Re). Upon the transfer of an electron, the transfer of a proton becomes much more favorable than the transfer of a proton to a neutral metal nitride ($\Delta G_{H^+}(1)$ is -125 kcal/mol for Mn vs $\Delta G_{H^+}(2)$ is -186 kcal/mol). However, going down the group, this proton transfer becomes less favorable from Mn (-186 kcal/mol) to Re (-174 kcal/mol). This trend is unlike that seen in the Miller system and requires further investigation. Furthermore, the calculation of the BDFE for the Miller systems shows a reverse trend in N-H bond strengths than the one observed in the Schneider systems. As we go down the group from Mn to Re, the strength of the N-H bond increases and more energy is required to break this bond. The dissociation free energy increases from 45 kcal/mol for Mn to 48 kcal/mol for Tc to 69 kcal/mol for Re.

The structural data for the electron, proton and hydrogen atom transfers is presented in Table 4.4. Upon the addition of an electron to the Mn, Tc, and Re metal nitride complexes, the M-N bond stretches slightly by an average of 0.03Å. An increase in M-N bond length is also observed upon the transfer of a proton and a hydrogen atom to the metal nitride complexes. Unlike the Schneider system, the transfer reactions to the Mn metal nitride of the Miller system do not exhibit unique structural effects in comparison with the Tc and Re systems. In attempts to rationalize the small change in M-N bond distance upon the transfer of an electron to the Mn metal nitride of the Schneider system, we look at the highest SOMO orbitals in which the added electron is located. We compare the SOMO orbitals of the Mn metal nitride anion radical with that of the Re metal nitride anion radical presented in Figure 4.4.

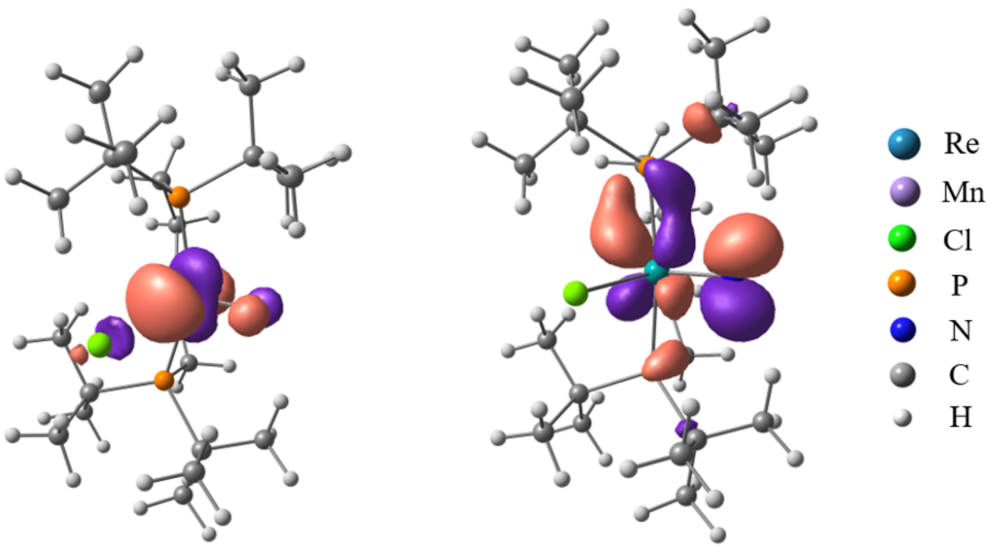

Figure 4.4: SOMO orbitals of the Mn (left) and Re (right) metal nitride anion radicals of the Schneider systems

Careful inspection of both presented orbitals shows that the Mn SOMO consists of a metal atomic orbital of d_{z^2} character and a nitrogen atomic p-orbital. This orbital shows more Mn character than nitrogen atom character. On the other hand, the Re SOMO consists of a delocalized d_{xy} Mn orbital and a p-orbital on the nitrogen. The two metal and nitrogen atomic orbitals are interacting out of phase with the formation of a nodal plane between them. The occupancy of this antibonding π-MO for the M-N, may explain the significant increase in M-N bond distance upon the addition of the electron to the Re metal nitride complex. The M-N bond distance increases from 1.66Å to 1.74Å in the Re system while it increases from 1.52Å to 1.53Å only in the Mn system. We also consider the SOMOs of the $(^{tBu}$PNP)MCl-NH complexes which are presented in Figure 4.9. The SOMOs of both Mn and Re are linear combinations of a metal d_{xy} orbital interacting out of phase with a nitrogen p-orbital. The later nitrogen p-orbital forms a sigma bond with the hydrogen s-orbital. Apart from the slight delocalization shown in the SOMO of the $(^{tBu}$PNP)ReCl-NH complex, the orbitals hosting the unpaired electron are similar in both Mn and Re complexes. Structurally, we

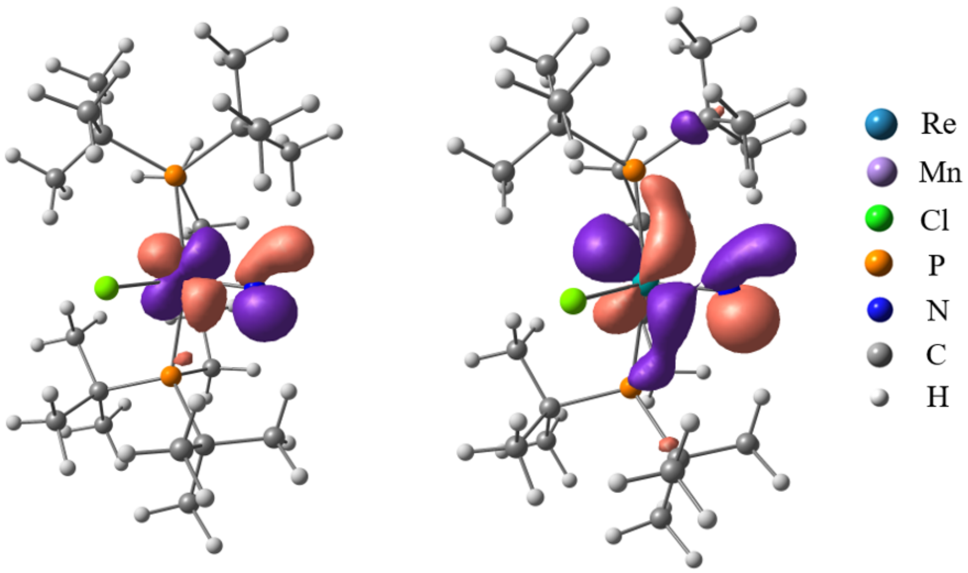

Figure 4.5: SOMO orbitals of the Mn (left) and Re (right) (^{tBu}PNP)MCl-NH complexes

observe the stretching of the M-N bond by around 0.13Å in both Mn and Re systems. The Re systems consistently show greater M-N bond distances than their Mn analogues, which may be rationalized by the greater size of the 5d orbital in Re with respect to the 3d orbital in Mn.

4.1.3 Hydrogen, Nitrogen & Oxygen Atom Transfer Reactions to Metal Nitride Complexes

We extend our study of the reactivity of metal nitride complexes to include transfer reactions of atoms of different electronegativity. We consider the transfer of hydrogen, nitrogen, and oxygen atoms from molecular hydrogen, nitrogen, and oxygen as shown in equation 1.

$$2\text{MN} + \text{X}_2 \xrightarrow{\Delta G_{transfer}} 2\ \text{MNX} \quad (1)$$

While hydrogen atom transfers have direct applications in ammonia synthesis, nitrogen atom transfers can be tied to the formation of the terminal μ-N_2 complexes and the reductive cleavage of the N_2 bond. Furthermore, considering the transfer of oxygen atoms as well will provide a more fundamental understanding of how the transfer of different atoms is affected by the nature of the metal center and the coordination sphere of the metal nitride complex. We first consider the transfer reactions to the five coordinate metal nitride of Schneider's system.

The free energies of the transfer reactions are given in Table 4.6. As seen in subsection 4.1.2 by the BDFE calculations, the transfer of a hydrogen atom

Table 4.5: Hydrogen, nitrogen, and oxygen transfer reactions to Schneider's nitride complex

	$\Delta G_{transfer}$ (kcal/mol)		
X_2	H_2	N_2	O_2
Mn	12.4	-41.6	-33.0
Tc	22.9	14.5	-20.4
Re	17.4	20.5	-18.2

to the Mn metal nitride is more favorable ($\Delta G_{transfer}$= 12.4 kcal/mol) than the transfer of a hydrogen atom to the Tc and Re metal nitrides ($\Delta G_{transfer}$= 22.9 kcal/mol and 17.4 kcal/mol, respectively). The transfer of the more electronegative nitrogen atom from molecular dinitrogen is more favorable than the hydrogen atom transfer (HAT) for the Mn and Tc systems. A dramatic drop in $\Delta G_{transfer}$ is observed for Mn where the free energy dropped from 12.4 kcal/mol to -41.6 kcal/mol. However, for the rhenium system, the free energy of nitrogen atom transfer is slightly greater than that of HAT. While HAT reactions were unfavorable for all three metal complexes, the nitrogen atom transfer was thermodynamically favorable for the Mn system. The transfer of the more electronegative oxygen atom was thermodynamically favorable ($\Delta G_{transfer} < 0$) for all Mn, Tc, and Re metal nitrides. Similar to the previous two transfers, the oxygen transfer reaction is significantly more favorable for the Mn nitride complex than the Tc and Re complexes with an energy difference greater than 10 kcal/mol. The structural data of the formed imido, dinitrogen, and nitrosyl containing complexes is presented in Table 4.6.

Table 4.6: Structural data of transfer reaction products: Schneider's complex $^{(a)}$

	MN	MNH		MNN		MNO	
	M–N	M-N	N-H	M-N	N-N	M-N	N-O
Mn	1.52	1.66	1.03	1.78	1.14	1.62	1.19
Tc	1.62	1.76	1.03	1.94	1.13	1.73	1.20
Re	1.66	1.78	1.02	1.94	1.14	1.75	1.20

(a) Bond distances are given in Å.

The transfer of a hydrogen atom to nitrogen of the metal nitride moiety leads to the formation of an imido ligand. In all three metal systems, this leads to the stretching of the M≡N bond by a distance of around 0.14Å. The M-N-H bond angle is bent at 127^o for the Mn imido complex, at 131^o for the Tc imido complex, and at 134^o for the Re imido complex. From this geometry and the Valence Shell Electron Pair Repulsion (VSEPR) theory, we can propose the following Lewis structure for the M-N-H moiety:

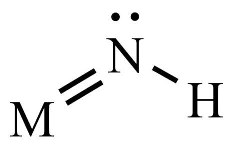

The transfer of a nitrogen atom to the nitrogen of the metal nitride group leads to the formation of a dinitrogen ligand, previously seen in the terminal μ-N_2 ligands discussed in Chapter 2. The transfer of the N-atom leads to more stretching of the M-N bond from 1.52Å to 1.78Å for Mn and from 1.66Å to 1.94Å for Re. This may be an indication of a loss of triple bond character between the metal center and the proximal nitrogen upon the formation of the strong N≡N bond. The M-N-N bond angle is close to linear in all three metal complexes: 175^o for Mn, 174^o for Tc, and 173^o for Re. This description of the bond angles and lengths, along with our prior knowledge of VSEPR theory allows us to predict the following Lewis structure for the M-N-N group:

The transfer of an oxygen atom to the nitrogen of the metal nitride group forms a nitrosyl group coordinated to the metal center. Upon the transfer of the oxygen atom, the M-N bond stretches from 1.52Å to 1.62Å for Mn, from 1.62Å to 1.73Å, and from 1.66Å to 1.75Å for Re. The increase in bond length is around 0.1Å for all three systems. The geometry of the M-N-O group may be linear or bent depending on many factors, one of which are the interaction of the metal MOs with the NO MOs [51]. Complexes in which backbonding is observed between the π^* orbital of the NO group and the d-orbital of the metal usually have linear M-N-O groups, while those exhibiting less backbonding tend to have linear M-N-O groups. The linear nitrosyl groups usually have an N≡O triple bond, while the bent nitrosyl groups usually have a N=O double bond. In the Schneider nitrosyl complexes considered here, the M-N-O angle is almost linear with a $\angle$MNO= 168^o for Mn and 169^o for Tc and Re. Inspection of the molecular orbitals of the Mn and Re Schneider nitrosyl complexes also shows considerable backbonding in a pair of perpendicular MOs for each complex (Figure 4.6). From the above structural and electronic data, we can propose the Lewis structure below.

In addition to reactions of metal nitrides of Schneider's systems, we also consider reactions of the six-coordinate nitride complexes of Miller's system. Similar to the previous system, the hydrogen atom transfer is more favorable for the Mn

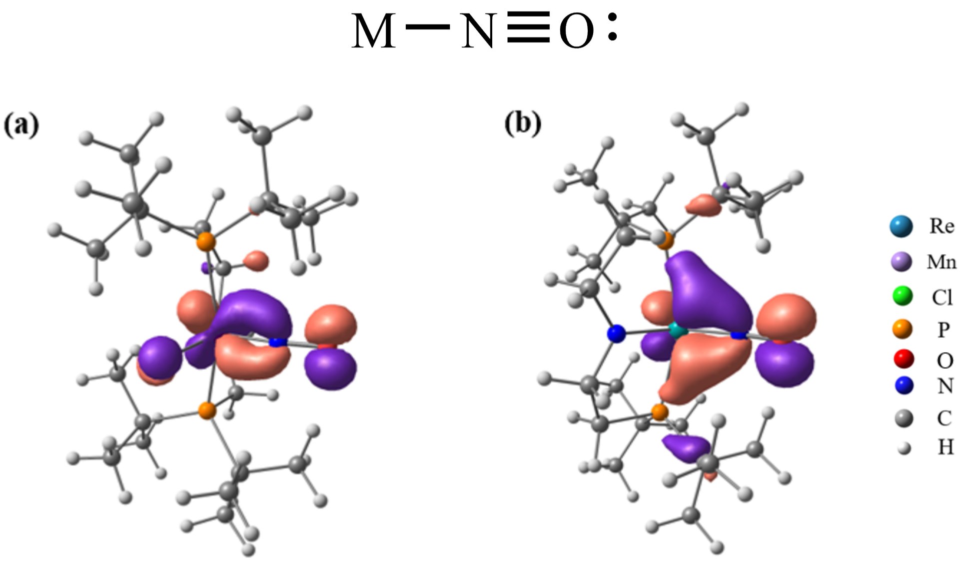

Figure 4.6: MOs for the (a) Mn and (b) Re Schneider nitrosyl complexes showing backbonding

system (-4.4 kcal/mol) than for the Tc (16.5 kcal/mol) and Re (18.9 kcal/mol) system. The transfer of the nitrogen atom is more favorable than the H-atom transfer for all three metal nitride complexes. While the nitrogen atom transfer is highly exergonic for Mn (-22.8 kcal/mol), it is exoneutral for the Tc complex (-0.8 kcal/mol) and slightly endergonic for the Re metal nitride (5.3 kcal/mol). An oxygen transfer is even more energetically favorable than both hydrogen and nitrogen transfers for all three metal complexes. The O_2 double bond is weaker than the strong N_2 triple bond. This contributes to the observed high nitrogen atom transfer energies and lower oxygen transfer energies.

Table 4.7: Hydrogen, nitrogen, and oxygen transfer reactions to Miller's nitride complex

	$\Delta G_{transfer}$ (kcal/mol)		
X_2	H_2	N_2	O_2
Mn	-4.4	-22.8	-42.8
Tc	16.5	-0.8	-33.9
Re	18.9	5.3	-32.7

The oxygen transfer reaction to Mn is the most favorable transfer reaction with $\Delta G_{transfer}$ = -42.8 kcal/mol. The calculated free energy of this transfer is 10 kcal/mol higher for the Tc and Re systems than for Mn. The structural data of the formed imido, dinitrogen, and nitrosyl compounds is presented in Table 4.8.

Table 4.8: Structural data of transfer reaction products: Miller's complex[(a)]

	MN	MNH		MNN		MNO	
	M–N	M-N	N-H	M-N	N-N	M-N	N-O
Mn	1.51	1.70	1.03	1.90	1.12	1.76	1.19
Tc	1.62	1.78	1.03	1.99	1.12	1.74	1.18
Re	1.66	1.79	1.02	1.97	1.13	1.76	1.19

(a) Bond distances are given in Å.

The transfer of a hydrogen atom to the Mn Miller metal nitride complex leads to the stretching of the Mn-N bond from 1.51Å to 1.70Å. Similarly the Tc-N and Re-N bonds also increase by 0.16Å and 0.13Å, respectively, upon the transfer of a hydrogen atom. The M-N-H bond angle is bent in all three metal complexes to different degrees. The Mn complex has the smallest ∠MNH of 111^o. While the Tc complex has a slightly larger ∠MNH value (116^o), the Re complex displays a significantly larger ∠MNH at 138^o. Similar to the Schneider metal imido complexes, the M-N-H group is proposed to have the following Lewis structure based on the above structural data and VSEPR theory:

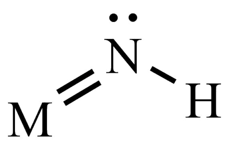

As observed in the 5-coordinate Schneider complexes, we observe a significant increase in M-N bond length upon the transfer of a nitrogen atom to the metal nitride group. The Mn-N distance increased by 0.39Å, while the Tc-N and Re-N bond distances increased by 0.37Å and 0.31Å, respectively. These larger increases indicate a loss of triple bond character. The M-N-N bond angle in all three dinitrogen complexes is almost linear (179^o). We propose a similar general Lewis structure for the Miller dinitrogen complexes as for the Schneider system:

Similar to the previously considered transfer reactions, the metal nitride bond lengths also increased in the Miller metal nitride systems upon the transfer of an oxygen atom to them. They also showed linear M-N-O bond angles of around 176^o. We therefore propose a linear geometry for the M-N-O group with a single bond between the metal center and the nitrogen and a triple bond between the nitrogen and the oxygen.

$$\mathrm{M-N\equiv O:}$$

4.1.4 Concluding Remarks

In this chapter, we focused on the effect of the nature of the metal center and the coordination sphere on reactions of molecular metal nitride complexes. The goal was to gain a deeper understanding of the highly covalent M≡N bond and its reactivity. We considered a total of five transfer reactions (proton, electron, hydrogen atom, nitrogen atom, and oxygen atom transfers) to two organometallic systems (Miller and Schneider's systems) of different coordination spheres. Depending on the type of the transfer, we observed different computational results. These observations are summed in the following points:

- Within a single organometallic system, the nature of the metal affected how favorable an electron transfer is to the system. In both Miller and Schneider's systems, electron transfers were more favorable to first row transition metal (TM) complexes and became less favorable going down the group. Simplistically, this may be attributed to the size of the metal d-orbital in which the added electron would reside. First row transition metals had smaller 3d orbitals than the 4d and 5d orbitals present in later transition metals. This would allow the electron to be in a more bound state with the positively charged nucleus, maximizing attraction, minimizing repulsion with other electrons, and lowering the overall energy of the complex. We notice no major effect of changing the coordination sphere on electron transfers.

- Proton transfers to the two metal systems were also affected by the nature of the metal. In both systems considered, as we substituted the metal from a first row TM to a larger second and third row TM, the proton transfer became more favorable. An exception to this case would be the second proton transfer observed in Pathway -2- for the Schneider system. The positively charged proton is added to the nitrogen of the metal nitride moiety. As we go down the group, we observe that the M≡N group becomes more electron rich due to the larger atomic number of the metal. So, as the number of electrons increases, the electron cloud around the M≡N group becomes significantly larger. The formation of delocalized MOs across the MN group allows for electrons to spread across it. Overall attraction increases going down the group, and therefore, energy is decreased. This explanation, although simple, helps us rationalize the general observed trend. Proton transfers, however, seem to be more affected by the coordination sphere than electron transfers as seen in the exception. This reversal of the general trend may be due to interactions between the ligands and the M≡N group, which alter the symmetry and the energetics of the MOs needed for the reaction.

- Both the nature of the metal and the coordination sphere affect the transfer of a hydrogen atom to the metal complexes as reflected in the BDFE calculations. These calculations are based on the individual electron and proton transfer reactions. The Miller complexes and the Schneider complexes displayed reverse trends in BDFE values. This indicates that the structure of the complex affected its susceptibility to added groups. While the sequential addition of an electron then a proton (or vice versa) is affected by the coordination sphere, the homolytic cleavage of an H_2 molecule followed by the transfer of a hydrogen atom to the metal complexes has shown similar trends in both systems. The isolation and cleavage of H_2 is experimentally costly and so PCET reactions may be experimentally more efficient.

- The transfer of a nitrogen and oxygen atom to the metal systems were more favorable than the transfer of the hydrogen atom for each metal system. Two main trends where observed in these transfer reactions: (1) The transfer reactions were always less favorable going from the first row transition metal complex to later transition metal complexes and (2) the larger and more electronegative the transferred group was the more favorable the transfer was within the same metal system. While we weren't able to provide a detailed study of the factors affecting these specific trends due to time restrictions, the data presented and the observations made may serve as a building block for further studies on reactions of metal nitrides.

We hope that this short study on the reactivity of the M≡N group would aid in future experimental or theoretical studies on the synthesis of ammonia as an alternative fuel or a necessary fertilizing agent.

Appendix A

Abbreviations

AO	Atomic Orbital
BDFE	Bond Dissociation Free Energy
BO	Bond Order
DFT	Density Functional Theory
ECP	Effective Core Potential
HAT	Hydrogen Atom Transfer
HF	Hartree-Fock
HOMO	Highest Occupies Molecular Orbital
HPC	High Performance Computer
IR	Infrared
IRC	Intrinsic Reaction Coordinates
LCAO	Linear Combination of Atomic Orbitals
LUMO	Lowest Unoccupied Molecular Orbital
MO	Molecular Orbital
NBO	Natural Bond Orbital
NMR	Nuclear Magnetic Resonance
PCET	Proton Coupled Electron Transfer
PES	Potential Energy Surface
SCF	Self-Consistent Field
SOMO	Singly Occupied Molecular Orbital
TS	Transition State
UV/Vis	Ultraviolet-Visible

Appendix B

Job Script Samples

B.1 Optimization and Frequency Calculations

```
%chk=NH3-gas
%mem=48GB
%nprocshared=28
# M06L/gen scf=direct
density=current integral=(grid=ultra,acc2e=11)
6d 10f sym=loose opt=(calcfc,tight) freq

NH3-gas

0 1
 N                  0.79246880    0.67177848    0.01037398
 H                  1.12579069   -0.27103461    0.01037398
 H                  1.12580790    1.14317866    0.82687072
 H                  1.12580790    1.14317866   -0.80612275

N H 0
6-311G(d,p)
****
```

Figure B.1: Sample input showing the commands needed for the optimization and frequency calculation of the optimized geometry of an NH_3 molecule

```
Optimization completed.
   -- Stationary point found.
                           ----------------------------
                           !   Optimized Parameters   !
                           ! (Angstroms and Degrees)  !
 --------------------------                            --------------------------
 ! Name  Definition              Value          Derivative Info.                !
 --------------------------------------------------------------------------------
 ! R1    R(1,2)                  1.0161         -DE/DX =    0.0                 !
 ! R2    R(1,3)                  1.0161         -DE/DX =    0.0                 !
 ! R3    R(1,4)                  1.0161         -DE/DX =    0.0                 !
 ! A1    A(2,1,3)              104.896          -DE/DX =    0.0                 !
 ! A2    A(2,1,4)              104.896          -DE/DX =    0.0                 !
 ! A3    A(3,1,4)              104.896          -DE/DX =    0.0                 !
 ! D1    D(2,1,4,3)           -110.2437         -DE/DX =    0.0                 !
 --------------------------------------------------------------------------------
GradGradGradGradGradGradGradGradGradGradGradGradGradGradGradGradGradGrad

                         Input orientation:
 ---------------------------------------------------------------------
 Center     Atomic      Atomic             Coordinates (Angstroms)
 Number     Number       Type             X           Y           Z
 ---------------------------------------------------------------------
      1          7           0        0.735900    0.671779    0.010374
      2          1           0        1.144813   -0.258427    0.010374
      3          1           0        1.144830    1.136875    0.815952
      4          1           0        1.144830    1.136875   -0.795204
 ---------------------------------------------------------------------
                   Distance matrix (angstroms):
                    1          2          3          4
     1  N    0.000000
     2  H    1.016117   0.000000
     3  H    1.016117   1.611156   0.000000
     4  H    1.016117   1.611156   1.611156   0.000000
 Stoichiometry    H3N
 Framework group  C3V[C3(N),3SGV(H)]
 Deg. of freedom     2
 Full point group                 C3V     NOp   6
 Largest Abelian subgroup         CS      NOp   2
 Largest concise Abelian subgroup CS      NOp   2
```

Figure B.2: Sample output showing the optimized geometric parameters of the NH_3 molecule shown

```
Harmonic frequencies (cm**-1), IR intensities (KM/Mole), Raman scattering
activities (A**4/AMU), depolarization ratios for plane and unpolarized
incident light, reduced masses (AMU), force constants (mDyne/A),
and normal coordinates:
                      1                      2                      3
                     A1                      E                      E
Frequencies --   1126.5217              1694.3339              1694.3592
Red. masses --      1.1778                 1.0628                 1.0628
Frc consts  --      0.8806                 1.7976                 1.7976
IR Inten    --    143.2540                16.0853                16.0911
 Atom  AN      X      Y      Z        X      Y      Z        X      Y      Z
    1   7     0.00   0.00   0.11     0.00   0.07   0.00    -0.07   0.00   0.00
    2   1     0.00  -0.22  -0.53     0.00   0.15   0.26     0.76   0.00   0.00
    3   1     0.19   0.11  -0.53     0.39  -0.53  -0.13     0.07  -0.39   0.23
    4   1    -0.19   0.11  -0.53    -0.39  -0.53  -0.13     0.07   0.39  -0.23
                      4                      5                      6
                     A1                      E                      E
Frequencies --   3469.6340              3606.5918              3606.6601
Red. masses --      1.0289                 1.0876                 1.0876
Frc consts  --      7.2978                 8.3352                 8.3355
IR Inten    --      1.0565                 0.1895                 0.1764
 Atom  AN      X      Y      Z        X      Y      Z        X      Y      Z
    1   7     0.00   0.00  -0.04     0.08   0.00   0.00     0.00   0.08   0.00
    2   1     0.00  -0.55   0.19     0.02   0.00   0.00     0.00  -0.75   0.32
    3   1     0.47   0.27   0.19    -0.56  -0.33  -0.28    -0.33  -0.17  -0.16
    4   1    -0.47   0.27   0.19    -0.56   0.33   0.28     0.33  -0.17  -0.16
```

Figure B.3: Sample output showing the frequency calculations of the NH_3 molecule shown

```
-------------------
- Thermochemistry -
-------------------
Temperature   298.150 Kelvin.  Pressure   1.00000 Atm.
Atom     1 has atomic number  7 and mass  14.00307
Atom     2 has atomic number  1 and mass   1.00783
Atom     3 has atomic number  1 and mass   1.00783
Atom     4 has atomic number  1 and mass   1.00783
Molecular mass:    17.02655 amu.
Principal axes and moments of inertia in atomic units:
                          1         2         3
    Eigenvalues --     6.15606   6.15606   9.34239
          X            0.95441   0.29850   0.00000
          Y           -0.29850   0.95441   0.00000
          Z            0.00000   0.00000   1.00000
This molecule is an oblate symmetric top.
Rotational symmetry number  3.
Rotational temperatures (Kelvin)     14.06969    14.06969     9.27106
Rotational constants (GHZ):         293.16506   293.16506   193.17767
Zero-point vibrational energy      90904.8 (Joules/Mol)
                                  21.72678 (Kcal/Mol)
Vibrational temperatures:   1620.81  2437.77  2437.80  4992.02  5189.07
         (Kelvin)           5189.17

Zero-point correction=                           0.034624 (Hartree/Particle)
Thermal correction to Energy=                    0.037483
Thermal correction to Enthalpy=                  0.038427
Thermal correction to Gibbs Free Energy=         0.016591
Sum of electronic and zero-point Energies=          -56.528715
Sum of electronic and thermal Energies=             -56.525855
Sum of electronic and thermal Enthalpies=           -56.524911
Sum of electronic and thermal Free Energies=        -56.546748

                    E (Thermal)          CV                S
                     KCal/Mol       Cal/Mol-Kelvin    Cal/Mol-Kelvin
Total                  23.521             6.294             45.959
Electronic              0.000             0.000              0.000
Translational           0.889             2.981             34.441
Rotational              0.889             2.981             11.452
Vibrational            21.744             0.333              0.066
                          Q            Log10(Q)             Ln(Q)
Total Bot       0.233735D-07        -7.631276         -17.571662
Total V=0       0.197034D+09         8.294542          19.098889
Vib (Bot)       0.119213D-15       -15.923678         -36.665623
Vib (V=0)       0.100494D+01         0.002140           0.004928
Electronic      0.100000D+01         0.000000           0.000000
Translational   0.276150D+07         6.441145          14.831285
Rotational      0.709998D+02         1.851257           4.262677
***** Axes restored to original set *****
-------------------------------------------------------------------
```

Figure B.4: Sample output showing the thermochemistry section of the frequency calculations of the NH_3 molecule shown

B.2 Single Point Calculations

```
%chk=NH3-gas
%mem=48GB
%nprocshared=28
#M06L/gen scf=(direct)
density=current integral=(grid=ultrafine,acc2e=11)
6d 10f  sym=loose guess=read geom=check scrf=(smd,solvent=thf)

NH3-sol

0 1

N H 0
Def2tzvp
****

--link1--
%mem=48GB
%chk=NH3-gas
%nprocshared=28
#M06L/gen scf=(direct)
density=current integral=(grid=ultrafine,acc2e=11)
6d 10f  sym=loose guess=read geom=check scrf=(smd,solvent=acetonitrile)

NH3-sol

0 1

N H 0
Def2tzvp
****
```

Figure B.5: Sample input showing the commands needed for a simple point calculation of the optimized geometry of an NH_3 molecule in solvent continuum using a larger basis set

```
Polarizable Continuum Model (PCM)
=================================
Model                  : PCM (using non-symmetric T matrix).
Atomic radii           : SMD-Coulomb.
Polarization charges   : Total charges.
Charge compensation    : None.
Solution method        : On-the-fly selection.
Cavity type            : VdW (van der Waals Surface) (Alpha=1.000).
Cavity algorithm       : GePol (No added spheres)
                         Default sphere list used, NSphG=    4.
                         Lebedev-Laikov grids with approx.  5.0 points / Ang**2.
                         Smoothing algorithm: Karplus/York (Gamma=1.0000).
                         Polarization charges: spherical gaussians, with
                                               point-specific exponents (IZeta= 3).
                         Self-potential: point-specific (ISelfS= 7).
                         Self-field     : sphere-specific E.n sum rule (ISelfD= 2).
Solvent                : TetraHydroFuran, Eps=   7.425700 Eps(inf)=   1.974025
------------------------------------------------------------------------------
Spheres list:
ISph  on   Nord     Re0    Alpha      Xe           Ye           Ze
   1   N      1   1.8900  1.000     0.000000     0.000000     0.122677
   2   H      2   1.2000  1.000     0.000000     0.930201    -0.286247
   3   H      3   1.2000  1.000    -0.805578    -0.465101    -0.286247
   4   H      4   1.2000  1.000     0.805578    -0.465101    -0.286247
------------------------------------------------------------------------------
------------------------------------------------------------------------------
Atomic radii for non-electrostatic terms: SMD-CDS.
------------------------------------------------------------------------------
Nuclear repulsion after PCM non-electrostatic terms =      11.9244688178 Hartrees.
One-electron integrals computed using PRISM.
NBasis=    54 RedAO= T EigKep=  3.94D-04  NBF=    36    18
NBsUse=    54 1.00D-06 EigRej= -1.00D+00 NBFU=    36    18
Initial guess from the checkpoint file:  "NH3-gas.chk"
B after Tr=     0.000000     0.000000     0.000000
        Rot=    1.000000     0.000000     0.000000     0.000000 Ang=   0.00 deg.
Initial guess orbital symmetries:
```

Figure B.6: Sample output showing the polarizable continuum model used in the single point calculation

```
      Occupied  (A1) (A1) (E) (E) (A1)
      Virtual   (A1) (E) (E) (E) (E) (A1) (A1) (E) (E) (A1) (E)
                (E) (A1) (A2) (E) (E) (E) (E) (A1) (E) (E) (A1)
                (E) (E) (A1) (E) (E) (A1) (E) (E) (A1) (A1) (?A)
                (?A) (?A) (?A) (?A) (?A) (?A) (?A) (?A) (?A) (?A)
                (?A) (?A) (?A) (?A) (?A) (?A)
 Keep J ints in memory in symmetry-blocked form, NReq=5265182.
 Requested convergence on RMS density matrix=1.00D-08 within 128 cycles.
 Requested convergence on MAX density matrix=1.00D-06.
 Requested convergence on             energy=1.00D-06.
 No special actions if energy rises.
 Inv3:  Mode=1 IEnd=     437772.
 Iteration    1 A*A^-1 deviation from unit magnitude is 2.44D-15 for     80.
 Iteration    1 A*A^-1 deviation from orthogonality  is 2.82D-15 for    192    113.
 Iteration    1 A^-1*A deviation from unit magnitude is 2.33D-15 for    306.
 Iteration    1 A^-1*A deviation from orthogonality  is 5.38D-15 for    351    276.
 Error on total polarization charges =  0.01320
 SCF Done:  E(RM06L) =  -56.5758745201     A.U. after   10 cycles
            NFock= 10  Conv=0.48D-09     -V/T= 2.0052
 SMD-CDS (non-electrostatic) energy       (kcal/mol) =       1.68
 (included in total energy above)
```

Figure B.7: Sample output showing the polarizable continuum model used in the single point calculation along with the calculated electronic energy

B.3 Transition State Calculations

```
%chk=Re-PNP-sing-TS
%mem=78GB
%nprocshared=28
#M06L/gen pseudo=read scf=(direct) density=current integral=(grid=superfine,acc2e=11)
opt=(modredundant,noeigentest,calcfc) 6d 10f sym=loose freq

Re-PNP-sing-TS

0 1
 Re,0,-2.4186286665,-0.0343244995,0.0110298944
 C,0,-4.4160438178,-2.4186876727,-1.767096873
 P,0,-2.6229749012,-2.1653352436,-1.138838602
 N,0,-3.1686976053,-1.1802947594,1.471364085
                        .
                        .
                        .
                        .
                        .
 H,0,0.6724416965,-3.692480443,1.5594320034
 H,0,0.1652663541,-1.9881954207,1.4413412626
 C,0,2.3957115334,-3.486425744,3.6251215759
 H,0,1.6177901129,-3.8193490941,4.3214103502
 H,0,3.2671205015,-3.2153174712,4.2242693975
 H,0,2.6612564741,-4.3468791254,3.0025467839
 C,0,1.525860558,-1.1165785232,3.6866058405
 H,0,0.7071479077,-1.3900905829,4.3624494358
 H,0,1.2048313264,-0.2613912092,3.0885769
 H,0,2.3648088545,-0.789149125,4.3002151294

10 80 f

C N H Cl P 0
6-311G(d,p)
****
Re 0
sdd
f 1 1.0
0.86 1.0
****

Re 0
sdd
```

Figure B.8: Sample input showing the commands needed for the optimization of the fixed geometry of the transition state.

```
******    1 imaginary frequencies (negative Signs) ******
Diagonal vibrational polarizability:
     123.0711718      60.8246590      52.9037565
Harmonic frequencies (cm**-1), IR intensities (KM/Mole), Raman scattering
activities (A**4/AMU), depolarization ratios for plane and unpolarized
incident light, reduced masses (AMU), force constants (mDyne/A),
and normal coordinates:
                      1                      2                      3
                      A                      A                      A
Frequencies --   -733.2661               18.1392                21.7553
Red. masses --     13.9679                4.0389                 4.0412
Frc consts  --      4.4249                0.0008                 0.0011
IR Inten    --     24.5970                0.1427                 0.4303
 Atom  AN      X      Y      Z        X      Y      Z        X      Y      Z
   1   75     0.00  -0.01  -0.00     0.00   0.00   0.01    -0.00   0.00  -0.01
   2    6     0.00  -0.00  -0.00     0.04   0.01  -0.03    -0.01  -0.00   0.01
   3   15     0.01   0.03   0.01     0.03   0.01  -0.02    -0.00   0.02  -0.03
   4    7     0.04   0.03  -0.02    -0.01  -0.02  -0.02     0.05  -0.02  -0.00
   5   15     0.03  -0.00  -0.01    -0.04  -0.02   0.02     0.01  -0.02   0.02
   6    6     0.00  -0.00   0.00    -0.03  -0.02   0.01    -0.04  -0.05   0.08
   7   17     0.00  -0.00   0.01     0.02   0.03   0.02    -0.06   0.03   0.02
   8    6    -0.00  -0.01  -0.00     0.04   0.02  -0.02    -0.02   0.04  -0.06
   9    6    -0.01   0.01   0.01    -0.06  -0.03   0.05     0.02   0.02  -0.03
  10    7     0.67  -0.23  -0.18    -0.00   0.01   0.04    -0.00   0.02  -0.04
  11    6     0.00   0.00  -0.00    -0.05  -0.04  -0.01     0.08  -0.05   0.05
  12    1     0.00   0.00   0.00    -0.05  -0.05  -0.03     0.07  -0.07   0.10
  13    1     0.00   0.00  -0.00    -0.08  -0.05  -0.01     0.11  -0.05   0.06
  14    6    -0.00   0.01   0.00    -0.04  -0.04  -0.02     0.11  -0.04   0.02
  15    1     0.01  -0.01  -0.03    -0.05  -0.05  -0.05     0.14  -0.05   0.06
  16    1     0.00  -0.00  -0.02    -0.06  -0.04   0.00     0.14  -0.02  -0.02
  17    6    -0.00   0.01  -0.01     0.00  -0.02  -0.03     0.06  -0.02  -0.02
  18    1    -0.02   0.05   0.00    -0.01  -0.03  -0.03     0.09  -0.03  -0.03
  19    1    -0.01   0.05  -0.01     0.01  -0.03  -0.05     0.07  -0.03   0.00
  20    6    -0.00   0.00  -0.00     0.03  -0.00  -0.03     0.04   0.00  -0.04
  21    1    -0.01  -0.02   0.00     0.02   0.01  -0.02     0.05   0.01  -0.07
  22    1    -0.02   0.00   0.00     0.04  -0.00  -0.04     0.05  -0.00  -0.04
  23    6    -0.00  -0.00   0.00    -0.02  -0.01   0.04    -0.11  -0.03   0.07
  24    1    -0.00   0.00   0.00    -0.02  -0.00   0.03    -0.14  -0.05   0.10
  25    1     0.00   0.00   0.00    -0.01   0.01   0.04    -0.12   0.00   0.04
  26    1    -0.00  -0.00   0.00    -0.03  -0.01   0.06    -0.11  -0.01   0.05
  27    6     0.00  -0.00  -0.00    -0.05  -0.04   0.01    -0.03  -0.09   0.11
  28    1     0.00  -0.00  -0.00    -0.05  -0.04   0.00    -0.05  -0.10   0.14
  29    1     0.00  -0.00  -0.00    -0.07  -0.04   0.02    -0.03  -0.09   0.10
  30    1     0.00  -0.00   0.00    -0.06  -0.05  -0.01     0.00  -0.11   0.11
  31    6    -0.00   0.00   0.00    -0.01  -0.01  -0.02    -0.05  -0.08   0.10
  32    1    -0.00   0.00   0.00    -0.01  -0.01  -0.02    -0.08  -0.10   0.14
```

Figure B.9: Sample output showing the calculated imaginary frequency during the optimization of the fixed geometry of the transition state.

```
%chk=Re-PNP-sing-TS
%mem=78GB
%nprocshared=28
#M06L/gen pseudo=read scf=(direct) density=current integral=(grid=superfine,acc2e=11)
 opt=(readfc,modredundant,noeigentest,TS) 6d 10f sym=loose freq guess=read geom=check

Re-PNP-sing-TS

0 1

10 80 a

C N H Cl P 0
6-311G(d,p)
****
Re 0
sdd
f 1 1.0
0.86 1.0
****

Re 0
sdd
```

Figure B.10: Sample input showing the commands needed for the optimization of the activated geometry of the transition state.

```
Optimization completed.
   -- Stationary point found.
                           ----------------------------
                           !   OPTIMIZED Parameters   !
                           ! (Angstroms and Degrees)  !
 --------------------------                            --------------------------
 ! Name  Definition              Value          Derivative Info.                !
 --------------------------------------------------------------------------------
 ! R1    R(1,3)                  2.4301         -DE/DX =    0.0                 !
 ! R2    R(1,4)                  2.0021         -DE/DX =    0.0                 !
 ! R3    R(1,5)                  2.4571         -DE/DX =    0.0                 !
 ! R4    R(1,7)                  2.486          -DE/DX =    0.0                 !
 ! R5    R(1,10)                 1.7626         -DE/DX =    0.0                 !
 ! R6    R(2,3)                  1.9168         -DE/DX =    0.0                 !
 ! R7    R(2,35)                 1.5346         -DE/DX =    0.0                 !
 ! R8    R(2,39)                 1.5303         -DE/DX =    0.0                 !
 ! R9    R(2,43)                 1.5305         -DE/DX =    0.0                 !
 ! R10   R(3,8)                  1.8979         -DE/DX =    0.0                 !
 ! R11   R(3,20)                 1.8404         -DE/DX =    0.0                 !
 ! R12   R(4,14)                 1.4665         -DE/DX =    0.0                 !
 ! R13   R(4,17)                 1.4672         -DE/DX =    0.0                 !
 ! R14   R(5,6)                  1.9014         -DE/DX =    0.0                 !
 ! R15   R(5,9)                  1.9019         -DE/DX =    0.0                 !
 ! R16   R(5,11)                 1.8517         -DE/DX =    0.0                 !
 ! R17   R(6,23)                 1.5294         -DE/DX =    0.0                 !
 ! R18   R(6,27)                 1.5321         -DE/DX =    0.0                 !
 ! R19   R(6,31)                 1.5343         -DE/DX =    0.0                 !
 ! R20   R(8,59)                 1.5341         -DE/DX =    0.0                 !
 ! R21   R(8,63)                 1.5282         -DE/DX =    0.0                 !
 ! R22   R(8,67)                 1.5343         -DE/DX =    0.0                 !
 ! R23   R(9,47)                 1.5282         -DE/DX =    0.0                 !
 ! R24   R(9,51)                 1.5295         -DE/DX =    0.0                 !
 ! R25   R(9,55)                 1.5335         -DE/DX =    0.0                 !
 ! R26   R(10,80)                1.583          -DE/DX =    0.0                 !
 ! R27   R(11,12)                1.0946         -DE/DX =    0.0                 !
 ! R28   R(11,13)                1.0951         -DE/DX =    0.0                 !
 ! R29   R(11,14)                1.5186         -DE/DX =    0.0                 !
 ! R30   R(14,15)                1.1025         -DE/DX =    0.0                 !
 ! R31   R(14,16)                1.1045         -DE/DX =    0.0                 !
 ! R32   R(17,18)                1.1031         -DE/DX =    0.0                 !
 ! R33   R(17,19)                1.1067         -DE/DX =    0.0                 !
 ! R34   R(17,20)                1.5194         -DE/DX =    0.0                 !
 ! R35   R(20,21)                1.0915         -DE/DX =    0.0                 !
 ! R36   R(20,22)                1.0942         -DE/DX =    0.0                 !
 ! R37   R(23,24)                1.096          -DE/DX =    0.0                 !
 ! R38   R(23,25)                1.0947         -DE/DX =    0.0                 !
 ! R39   R(23,26)                1.0932         -DE/DX =    0.0                 !
```

Figure B.11: Sample output showing the optimized geometric parameters of the activated geometry of the transition state.

```
%chk=Re-PNP-sing-TS-IRC.chk
%mem=78GB
%nprocshared=28
# irc=(maxpoints=20,recorrect=never,calcfc) gen 10f 6d density=current
integral=(grid=superfine,acc2e=11) m06l pseudo=read scf=direct sym=loose

Re-PNP-sing-TS-IRC

0 1
 Re                  -2.41739200   -0.03510000    0.01047900
 C                   -4.41441300   -2.42610200   -1.75915600
 P                   -2.62157600   -2.17056900   -1.13111700
 N                   -3.16827500   -1.17522000    1.47496800
 P                   -3.13871600    1.75128800    1.53553000
                                        .
                                        .
                                        .
                                        .
                                        .
 C                    2.39483500   -3.47376100    3.64016400
 H                    1.61655900   -3.80383100    4.33741400
 H                    3.26602700   -3.20044200    4.23862300
 H                    2.66051400   -4.33668900    3.02108200
 C                    1.52533200   -1.10355500    3.69198100
 H                    0.70628300   -1.37428800    4.36853600
 H                    1.20469700   -0.25066800    3.09046600
 H                    2.36406600   -0.77385400    4.30466700

C N H Cl P 0
6-311G(d,p)
****
Re 0
sdd
f 1 1.0
0.86 1.0
****
|
Re 0
sdd
```

Figure B.12: Sample input showing the commands needed for the calculation of the intrinsic reaction coordinates of the cleavage of a N_2 bimetallic bridged

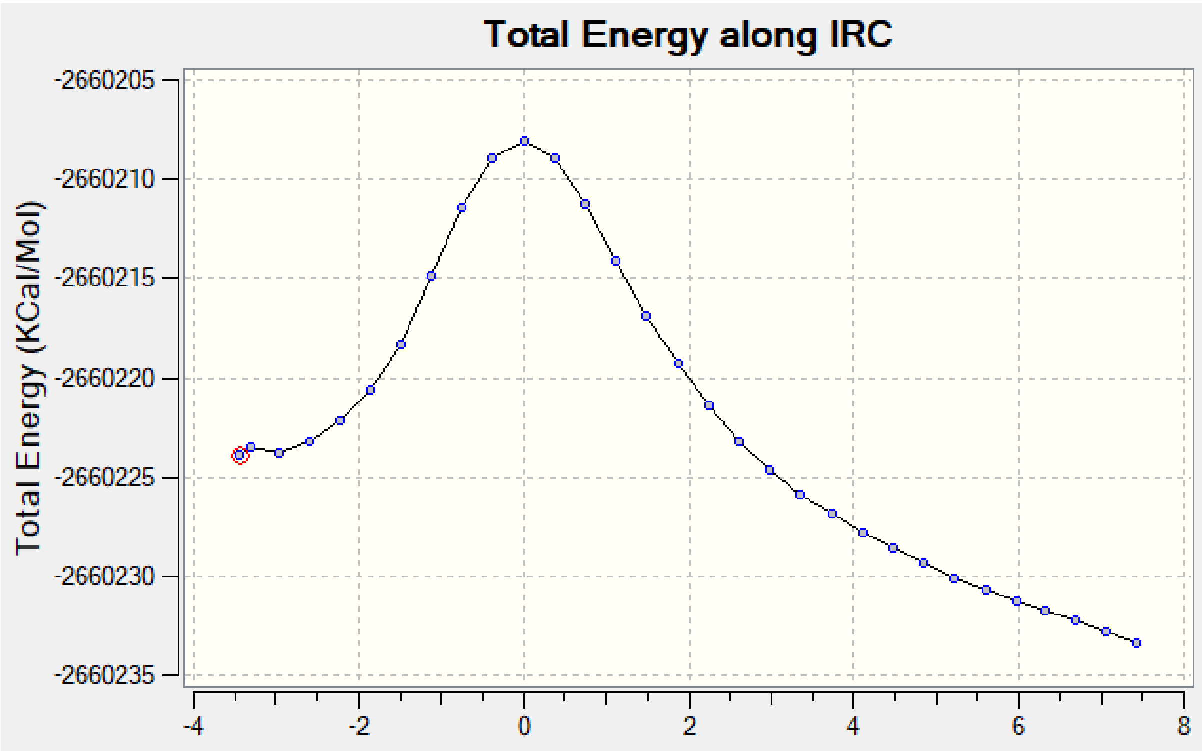

Figure B.13: Sample output showing the intrinsic reaction coordinates displayed by Gaussview of the cleavage of a N_2 bimetallic bridged

Bibliography

[1] J. W. Erisman, M. A. Sutton, J. Galloway, Z. Klimont, and W. Winiwarter, "How a century of ammonia synthesis changed the world," *Nature Geoscience*, vol. 1, no. 10, pp. 636–639, 2008.

[2] G. Ertl, "Reactions at surfaces: From atoms to complexity (nobel lecture)," *Angewandte Chemie International Edition*, vol. 47, no. 19, pp. 3524–3535, 2008.

[3] C. Smith, A. K. Hill, and L. Torrente-Murciano, "Current and future role of haber–bosch ammonia in a carbon-free energy landscape," *Energy & Environmental Science*, vol. 13, no. 2, pp. 331–344, 2020.

[4] J. Chatt, A. Pearman, and R. Richards, "The reduction of mono-coordinated molecular nitrogen to ammonia in a protic environment," *Nature*, vol. 253, no. 5486, pp. 39–40, 1975.

[5] C. E. Laplaza and C. C. Cummins, "Dinitrogen cleavage by a three-coordinate molybdenum (iii) complex," *Science*, vol. 268, no. 5212, pp. 861–863, 1995.

[6] T. J. Hebden, R. R. Schrock, M. K. Takase, and P. Müller, "Cleavage of dinitrogen to yield a (t-bupocop) molybdenum (iv) nitride," *Chemical Communications*, vol. 48, no. 13, pp. 1851–1853, 2012.

[7] R. Mulliken, "The nobel prize in chemistry 1966," *Nobelprize. org*, 2014.

[8] J. Pople, "The nobel prize in chemistry 1998 explore press release," *Nobelprize. org*, 2021.

[9] C. Riplinger, P. Pinski, U. Becker, E. F. Valeev, and F. Neese, "Sparse maps—a systematic infrastructure for reduced-scaling electronic structure methods. ii. linear scaling domain based pair natural orbital coupled cluster theory," *The Journal of chemical physics*, vol. 144, no. 2, p. 024109, 2016.

[10] S. Maeda and K. Morokuma, "Toward predicting full catalytic cycle using automatic reaction path search method: a case study on hco (co) 3-catalyzed

hydroformylation," *Journal of chemical theory and computation*, vol. 8, no. 2, pp. 380–385, 2012.

[11] I. Funes-Ardoiz and F. Schoenebeck, "Established and emerging computational tools to study homogeneous catalysis—from quantum mechanics to machine learning," *Chem*, vol. 6, no. 8, pp. 1904–1913, 2020.

[12] M. J. Frisch, G. W. Trucks, H. B. Schlegel, G. E. Scuseria, M. A. Robb, J. R. Cheeseman, G. Scalmani, V. Barone, G. A. Petersson, H. Nakatsuji, X. Li, M. Caricato, A. V. Marenich, J. Bloino, B. G. Janesko, R. Gomperts, B. Mennucci, H. P. Hratchian, J. V. Ortiz, A. F. Izmaylov, J. L. Sonnenberg, D. Williams-Young, F. Ding, F. Lipparini, F. Egidi, J. Goings, B. Peng, A. Petrone, T. Henderson, D. Ranasinghe, V. G. Zakrzewski, J. Gao, N. Rega, G. Zheng, W. Liang, M. Hada, M. Ehara, K. Toyota, R. Fukuda, J. Hasegawa, M. Ishida, T. Nakajima, Y. Honda, O. Kitao, H. Nakai, T. Vreven, K. Throssell, J. A. Montgomery, Jr., J. E. Peralta, F. Ogliaro, M. J. Bearpark, J. J. Heyd, E. N. Brothers, K. N. Kudin, V. N. Staroverov, T. A. Keith, R. Kobayashi, J. Normand, K. Raghavachari, A. P. Rendell, J. C. Burant, S. S. Iyengar, J. Tomasi, M. Cossi, J. M. Millam, M. Klene, C. Adamo, R. Cammi, J. W. Ochterski, R. L. Martin, K. Morokuma, O. Farkas, J. B. Foresman, and D. J. Fox, "Gaussian˜16 Revision A.03," 2016. Gaussian Inc. Wallingford CT.

[13] B. P. Pritchard, D. Altarawy, B. Didier, T. D. Gibson, and T. L. Windus, "New basis set exchange: An open, up-to-date resource for the molecular sciences community," *Journal of chemical information and modeling*, vol. 59, no. 11, pp. 4814–4820, 2019.

[14] E. Glendening, A. Reed, J. Carpenter, and F. Weinhold, "Nbo 3.0 program manual," *Theoretical Chemistry Institute, University of Wisconsin, Madison, WI*, 1990.

[15] R. Dennington, T. A. Keith, and J. M. Millam, "Gaussview Version 5," 2019. Semichem Inc. Shawnee Mission KS.

[16] G. Zhurko and D. Zhurko, "Chemcraft, version 1.6," *URL: http://www. chemcraftprog. com*, 2009.

[17] K. Arashiba, Y. Miyake, and Y. Nishibayashi, "A molybdenum complex bearing pnp-type pincer ligands leads to the catalytic reduction of dinitrogen into ammonia," *Nature chemistry*, vol. 3, no. 2, pp. 120–125, 2011.

[18] Y. Zhao and D. G. Truhlar, "A new local density functional for main-group thermochemistry, transition metal bonding, thermochemical kinetics, and noncovalent interactions," *The Journal of chemical physics*, vol. 125, no. 19, p. 194101, 2006.

[19] Y. Zhao and D. G. Truhlar, "Attractive noncovalent interactions in the mechanism of grubbs second-generation ru catalysts for olefin metathesis," *Organic letters*, vol. 9, no. 10, pp. 1967–1970, 2007.

[20] S. Grimme, S. Ehrlich, and L. Goerigk, "Effect of the damping function in dispersion corrected density functional theory," *Journal of computational chemistry*, vol. 32, no. 7, pp. 1456–1465, 2011.

[21] A. D. Becke and E. R. Johnson, "A density-functional model of the dispersion interaction," *The Journal of chemical physics*, vol. 123, no. 15, p. 154101, 2005.

[22] Q. J. Bruch, G. P. Connor, C.-H. Chen, P. L. Holland, J. M. Mayer, F. Hasanayn, and A. J. Miller, "Dinitrogen reduction to ammonium at rhenium utilizing light and proton-coupled electron transfer," *Journal of the American Chemical Society*, vol. 141, no. 51, pp. 20198–20208, 2019.

[23] F. Schendzielorz, M. Finger, J. Abbenseth, C. Würtele, V. Krewald, and S. Schneider, "Metal-ligand cooperative synthesis of benzonitrile by electrochemical reduction and photolytic splitting of dinitrogen," *Angewandte Chemie International Edition*, vol. 58, no. 3, pp. 830–834, 2019.

[24] M. J. Bezdek, S. Guo, and P. J. Chirik, "Terpyridine molybdenum dinitrogen chemistry: synthesis of dinitrogen complexes that vary by five oxidation states," *Inorganic chemistry*, vol. 55, no. 6, pp. 3117–3127, 2016.

[25] S. Rupp, F. Plasser, and V. Krewald, "Multi-tier electronic structure analysis of sita's mo and w complexes capable of thermal or photochemical n2 splitting," *European Journal of Inorganic Chemistry*, vol. 2020, pp. 1506–1518, 2020.

[26] D. Dubois and R. Hoffmann, "Diazenido, dinitrogen and related complexes.," *Nouv. J. Chim.; FR.; DA. 1977; vol. 1; no 6; PP. 479-492; bibl. 2 P.*, 1977.

[27] G. A. Silantyev, M. Förster, B. Schluschaß, J. Abbenseth, C. Würtele, C. Volkmann, M. C. Holthausen, and S. Schneider, "Dinitrogen splitting coupled to protonation," *Angewandte Chemie International Edition*, vol. 56, no. 21, pp. 5872–5876, 2017.

[28] A. Caselli, E. Solari, R. Scopelliti, C. Floriani, N. Re, C. Rizzoli, and A. Chiesi-Villa, "Dinitrogen rearranging over a metal- oxo surface and cleaving to nitride: From the end-on to the side-on bonding mode, to the stepwise cleavage of the nn bonds assisted by nbiii-calix [4] arene," *Journal of the American Chemical Society*, vol. 122, no. 15, pp. 3652–3670, 2000.

[29] H. W. Turner, J. D. Fellmann, S. M. Rocklage, R. R. Schrock, M. R. Churchill, and H. J. Wasserman, "Tantalum complexes containing diimido bridging dinitrogen ligands," *Journal of the American Chemical Society*, vol. 102, no. 26, pp. 7809–7811, 1980.

[30] U. J. Kilgore, X. Yang, J. Tomaszewski, J. C. Huffman, and D. J. Mindiola, "Activation of atmospheric nitrogen and azobenzene nn bond cleavage by a transient nb (iii) complex," *Inorganic chemistry*, vol. 45, no. 26, pp. 10712–10721, 2006.

[31] I. Klopsch, M. Finger, C. Wuurtele, B. Milde, D. B. Werz, and S. Schneider, "Dinitrogen splitting and functionalization in the coordination sphere of rhenium," *Journal of the American Chemical Society*, vol. 136, no. 19, pp. 6881–6883, 2014.

[32] B. M. Lindley, R. S. Van Alten, M. Finger, F. Schendzielorz, C. Wurtele, A. J. Miller, I. Siewert, and S. Schneider, "Mechanism of chemical and electrochemical n2 splitting by a rhenium pincer complex," *Journal of the American Chemical Society*, vol. 140, no. 25, pp. 7922–7935, 2018.

[33] N. Tsvetkov, H. Fan, and K. G. Caulton, "An evaluation of monovalent osmium supported by the pnp ligand environment," *Dalton Transactions*, vol. 40, no. 5, pp. 1105–1110, 2011.

[34] C. E. Laplaza, M. J. Johnson, J. C. Peters, A. L. Odom, E. Kim, C. C. Cummins, G. N. George, and I. J. Pickering, "Dinitrogen cleavage by three-coordinate molybdenum (iii) complexes: Mechanistic and structural data1," *Journal of the American Chemical Society*, vol. 118, no. 36, pp. 8623–8638, 1996.

[35] R. Ghosh, M. Kanzelberger, T. J. Emge, G. S. Hall, and A. S. Goldman, "Dinitrogen complexes of pincer-ligated iridium," *Organometallics*, vol. 25, no. 23, pp. 5668–5671, 2006.

[36] J. M. Smith, R. J. Lachicotte, K. A. Pittard, T. R. Cundari, G. Lukat-Rodgers, K. R. Rodgers, and P. L. Holland, "Stepwise reduction of dinitrogen bond order by a low-coordinate iron complex," *Journal of the American Chemical Society*, vol. 123, no. 37, pp. 9222–9223, 2001.

[37] S. F. McWilliams, K. R. Rodgers, G. Lukat-Rodgers, B. Q. Mercado, K. Grubel, and P. L. Holland, "Alkali metal variation and twisting of the fennfe core in bridging diiron dinitrogen complexes," *Inorganic chemistry*, vol. 55, no. 6, pp. 2960–2968, 2016.

[38] S. F. McWilliams, P. C. Bunting, V. Kathiresan, B. Q. Mercado, B. M. Hoffman, J. R. Long, and P. L. Holland, "Isolation and characterization of

a high-spin mixed-valent iron dinitrogen complex," *Chemical Communications*, vol. 54, no. 95, pp. 13339–13342, 2018.

[39] J. Chatt, R. Fay, and R. Richards, "Preparation and characterisation of the dinuclear dinitrogen complex, trichloro-μ-dinitrogen-bis (tetrahydrofuran){chlorotetrakis [dimethyl-(phenyl) phosphine] rhenium (I)} chromium (iii)[(pme 2 ph) 4 clren 2 crcl 3 (thf) 2]," *Journal of the Chemical Society A: Inorganic, Physical, Theoretical*, pp. 702–704, 1971.

[40] N. Re, M. Rosi, A. Sgamellotti, and C. Floriani, "Theoretical study of dinitrogen activation in dinuclear v (ii) and v (iii) hexacoordinated complexes: Ab initio calculations on various model compounds," *Inorganic Chemistry*, vol. 34, no. 13, pp. 3410–3417, 1995.

[41] R. Ferguson, E. Solari, C. Floriani, D. Osella, M. Ravera, N. Re, A. Chiesi-Villa, and C. Rizzoli, "Stepwise reduction of dinitrogen occurring on a divanadium model compound: A synthetic, structural, magnetic, electrochemical, and theoretical investigation on the [vnnv] n+[n= 4- 6] based complexes," *Journal of the American Chemical Society*, vol. 119, no. 42, pp. 10104–10115, 1997.

[42] J. J. Curley, T. R. Cook, S. Y. Reece, P. Muller, and C. C. Cummins, "Shining light on dinitrogen cleavage: structural features, redox chemistry, and photochemistry of the key intermediate bridging dinitrogen complex," *Journal of the American Chemical Society*, vol. 130, no. 29, pp. 9394–9405, 2008.

[43] L. S. Yamout, M. Ataya, F. Hasanayn, P. L. Holland, A. J. M. Miller, and A. S. Goldman, "Understanding terminal versus bridging end-on n2 coordination in transition metal complexes," *Journal of the American Chemical Society*, vol. 143, no. 26, pp. 9744–9757, 2021.

[44] M. Y. Combariza, A. M. Fahey, A. Milshteyn, and R. W. Vachet, "Gas-phase ion–molecule reactions of divalent metal complex ions: Toward coordination structure analysis by mass spectrometry and some intrinsic coordination chemistry along the way," *International Journal of Mass Spectrometry*, vol. 244, no. 2-3, pp. 109–124, 2005.

[45] R. Morassi, I. Bertini, and L. Sacconi, "Five-coordination in iron (ii); cobalt (ii) and nickel (ii) complexes," *Coordination Chemistry Reviews*, vol. 11, no. 4, pp. 343–402, 1973.

[46] L. Sacconi, "The influence of geometry and donor-atom set on the spin state of five-coordinate cobalt (ii) and nickel (ii) complexes," *Coordination Chemistry Reviews*, vol. 8, no. 4, pp. 351–367, 1972.

[47] G. B. Kauffman, "Inorganic chemistry, (miessler, gary l.; tarr, donald a.)," 2000.

[48] M. L. Besmer, H. Braband, S. Schneider, B. Spingler, and R. Alberto, "Exploring the coordination chemistry of n2 with technetium pnp pincer-type complexes," *Inorganic Chemistry*, vol. 60, no. 9, pp. 6696–6701, 2021.

[49] J. M. Mayer, "Proton-coupled electron transfer: a reaction chemist's view," *Annu. Rev. Phys. Chem.*, vol. 55, pp. 363–390, 2004.

[50] S. Chen, R. Rousseau, S. Raugei, M. Dupuis, D. L. DuBois, and R. M. Bullock, "Comprehensive thermodynamics of nickel hydride bis (diphosphine) complexes: a predictive model through computations," *Organometallics*, vol. 30, no. 22, pp. 6108–6118, 2011.

[51] J. Enemark and R. Feltham, "Principles of structure, bonding, and reactivity for metal nitrosyl complexes," *Coordination Chemistry Reviews*, vol. 13, no. 4, pp. 339–406, 1974.